ADVANCES IN SURFACE PENETRATING TECHNOLOGIES FOR IMAGING, DETECTION, AND CLASSIFICATION

by

Jay A. Marble

A dissertation submitted in partial fulfillment
of the requirements for the degree of
Doctor of Philosophy
(Electrical Engineering: Systems)
in The University of Michigan
2007

Doctoral Committee:

Professor Alfred O. Hero III, Co-Chair
Professor Andrew E. Yagle, Co-Chair
Professor Eric Michielssen
Associate Professor Mahta Moghaddam

To: the Environmental Research Institute of Michigan (ERIM)

ACKNOWLEDGMENTS

The author gratefully acknowledges the support of and collaboration with the U.S. Army's Night Vision and Electronic Sensor Directorate (NVESD). He also wishes to thank the Army Research Office (ARO) for their support of the Multi-modal, Adaptive Target Detection and Classification MURI (project number DAAD-19-02-1-0262). The views and conclusions contained in this document are those of the author and should not be interpreted as representing official policies, either expressed or implied, of NVESD, ARO, or the United States government.

For assistance with data processing, problem insights, and assistance with results thanks goes to Mehrdad Soumekh, Raviv Raich, Hakan Bagci, and Doron Blatt. For mentorship and career direction thanks goes to John Ackenhusen of General Dynamics - Advanced Information Systems (Ann Arbor) and Steve Bishop of NVESD. For use of their data and facilities thanks goes to Waymond Scott, Gregg Larson, and Jim McClellen of the Georgia Institute of Technology. For guidance in the first two years of research, thanks goes to Professor Andy Yagle. Thanks also to Professor Al Hero for challenging the author to approach academic problems in a more rigorous, theoretical way. Thanks to the E&M members of the committee Professor Eric Michielssen and Professor Mahta Moghaddam for their valuable insight.

For listening to the author complain about how much work it is to get a Ph.D., grateful thanks is due to his many friends, the Christian Faith Group, and especially Patrick Spicer. For emotional support throughout this five year life chapter the author thanks his family: James, Joyce, Jon, and Colleen Marble. For perseverance in study and the ability to

understand anything at all, the author humbly wishes to thank the Creator.

TABLE OF CONTENTS

LIST OF FIGURES

LIST OF TABLES

LIST OF APPENDICES

ABSTRACT

ADVANCES IN SURFACE PENETRATING TECHNOLOGIES FOR IMAGING, DETECTION, AND CLASSIFICATION

by

Jay A. Marble

Co-Chairs: Alfred O. Hero III and Andrew E. Yagle

Surface penetration for the purpose of detecting objects of interest is a field of importance in both military and civilian applications. This work touches on the entire scope of the problem, including the detection and classification of objects and the process of forming an image. Military applications such as See-Through-Wall radar and landmine detection dominate the specific applications explored. Initially, the problem of decreasing signal-to-noise ratio is addressed by applying non-statistical methods to signal enhancement. Metal detectors and ground penetrating radar, the standard sensors for landmine detection, are given the focus. Next, statistical methods are explored for both object detection and classification. A Gaussian mixture is used to model the response of multiple objects of interest to the standard sensors. Two sensor scheduling techniques are then studied within the context of confirmation. The first applies an information gain metric called the Rényi Divergence to schedule a single sensor out of a toolset of sensors. (Three appendices discuss the physics of potential sensors that could make up the toolset.) The second uses a learning approach to determine a policy for applying more than one confirmation sensor. The policy dictates when to declare an object class and when to deploy another sensor. The resulting policy produces the maximum probability of correct classification with the minimum number of sensor dwells. Imaging begins with backpropagation synthetic aperture radar imaging and progresses to an efficient implementation of wavenumber

migration. The use of a sparse prior for image reconstruction is introduced in an iterative method that transforms the data back and forth between image and observation domains using Landweber iteration. Soft-thresholding is used as the mechanism for applying the sparse prior. Examples are shown in 2D and 3D. The final contribution is an adaptive imaging technique called the Iterative Redeployment of Illumination and Sensing. This algorithm utilizes the scene itself to determine the best locations to acquire further observations. An E&M simulator dubbed a $virtual\ transmitter$ is used in conjunction with information gain to direct the imaging device to the next location. The final result is an image that approximates a large synthetic aperture from multiple observations with a much smaller aperture device.

CHAPTER I

INTRODUCTION

Surface penetrating technologies cover a vast range of research areas and applications. Areas of research include medicine, subterrestrial object detection, and package inspection. In medicine, the detection of cancerous tumors has been been of high interest throughout modern times. In recent years, package inspection, whether luggage or shipping crates or a building, has become of high interest. Subterrestrial detection can include objects near the surface like landmines or deep objects like underground tunnels. In this work the focus is primarily on military applications of subsurface methods. The fundamental process is to form an image from an appropriate sensor, detect the presence of objects, and then discriminate between objects of interest and objects not of interest.

Depending on the problem at hand, a suite of sensors may be required. One sensor may be useful in scanning large regions, while another is useful in removing ambiguity at a single point. Two types of objects may respond very differently to different sensor technologies. Some sensors may be easy (fast) to deploy and perform a measurement, while others may require a lot of power and averaging time (slow). This richness of technologies and signatures of interest makes an ideal problem for $sensor\ scheduling$, $detection/classification$, and $imaging$. The two applications that receive attention in exploring subsurface technologies here are $landmine\ detection$ and $see\text{-}through\text{-}wall\ imaging$.

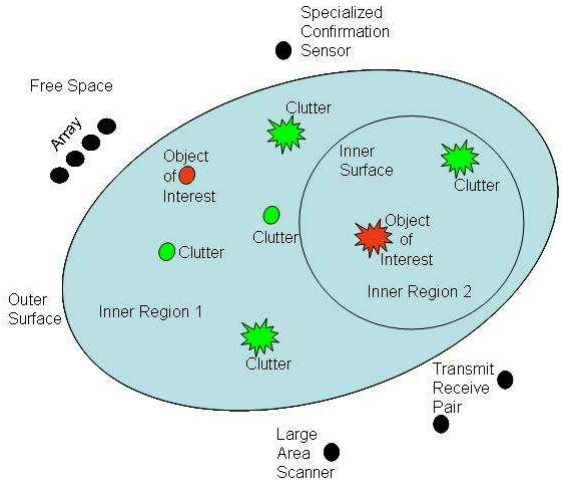

Figure 1.1: The Surface Penetrating Problem Generalized

1.1 Contributions Made

Low signal strength is an ever-present aspect of surface penetrating technologies. Objects close to the surface or with large cross section will give high signal returns. Achievable depth and detection of smaller targets will always be the technological frontier of surface penetration. In the first contribution chapter, methods of enhancing signal strength are explored. First, radar is used to image landmines to determine the depth, length, and height of objects. Knowledge of depth and size is a powerful discriminant between landmines and non-threatening clutter objects. We also look at a novel transform that sums all the energy in a hyperbolic radar signature. This transform eliminates clutter because real objects in radar data have a hyperbolic shape while clutter from ground strata do not. We then look at determining object size and shape using a metal detector. By identifying a set of basis functions and using subspace projection methods, the depth and basic object size and shape can be estimated.

In the second contribution chapter we look at probabilistic approaches of the landmine detection and classification problem. Multiple sensor technologies have been developed over the past ten years. Each target and clutter type has a different response to each sensor technology. In addition, object depth significantly changes signature statistics. Characterizing the signatures leads to a Gaussian mixture model. Multimodal sensing implies the use of multiple sensors to detect objects. By exploiting the joint probability

density function (PDF) of objects over all the sensors, the object class can be estimated. Two approaches are used. The first looks at Maximum a Posteriori estimation. The second simplifies the joint PDF using a Bayesian Network. The Bayes Net simplifies training and generalizes performance across multiple soil types.

The third contribution focuses on sensor scheduling. The landmine problem provides a rich tapestry of sensor technologies and object responses. Metal detection is employed to find mine casings. X-rays and other nuclear methods are used to detect explosives. Radar is used to detect changes in dielectric permittivity. Two stages of sensor scheduling is explored. The first considers the deployment of a single sensor. It uses an information based technique. For a given situation a measure of increased certainty called the $R\acute{e}nyi\ Divergence$ is computed. The sensor that displays the highest information gain (the highest probable increase in object certainty) is deployed. The problem is expanded to include time considerations. Next the problem of how many sensors to deploy before moving on is considered. Reinforcement learning is used to compute an optimal policy for deploying additional sensors based on the current set of measurements available. The solution is optimal in that it maximizes the probability of correct classification while making the fewest number of sensor deployments.

As mentioned above, the first stage of many surface penetration problems is imaging. An image must be made of the region under test that can be exploited by detection algorithms. In the next contribution chapter, we look at synthetic aperture radar imaging with a focus on the subsurface application. We first consider the basic backpropagation imaging algorithm. Acceleration of this algorithm is achieved using wavenumber migration, which is a technique borrowed from seismology. We go beyond this by introducing an iterative technique that makes use of the same approximations as wavenumber migration. In our approach the radar data is imaged using wavenumber migration and then $un\text{-}imaged$ using wavenumber migration in $reverse$. A control loop is formed by making use of $sparsity$. $Sparsity$ is the concept that the majority of pixels (or

voxels) in an image should be zero. A sparse prior constraint is placed on the reconstructed image. This constraint is applied in the image domain. The result is then $un\text{-}imaged$ and an error is formed with the data in the observation domain. Examples of this are shown for see-through-wall imaging in 2D and landmine imaging in 3D.

The final contribution chapter looks in depth at see-through-wall radar imaging. First we look at determining the unknown phase correction needed to properly focus radar waves that pass through an inhomogeneous medium. We also look at how to detect and map inner walls. A novel form of sensor scheduling called $Iterative\ Redeployment\ of\ Illumination\ and\ Sensing(IRIS)$ is explored. Here we look at the use of a small aperture (handheld) radar for building an image comparable to a long baseline apeture. The algorithm utilizes the scene itself to determine the best locations to acquire further observations for the given scene. Advanced E&M simulation tools dubbed $virtual\ transmitters$ are an integral part of this adaptive process. They predict the fields outside the structure being imaged and an information gain criteria is used to determine the best place to redeploy the small aperture radar.

1.2 Outline of Dissertation

In Chapter II an overview of the field is presented. We begin with a historical look at the military applications of surface penetrating technologies. This field began in earnest with foliage penetration during the Viet Nam era. The motivation was to detect vehicles under jungle foliage. In the early 1990s, military base closures drove environmental cleanup efforts to eliminate unexploded ordnance (UXO). By the late 1990s, the focus has shifted from UXO to landmines. In recent years, tunnel detection has come to the forefront. Also in recent years many new applications have surfaced. These include luggage and package inspection and other applications. The two primary areas explored in this dissertation are landmine detection and see-through-the- wall radar. The challenges and goals of each research area are discussed in some detail.

Chapters III, IV, and V address issues in landmine detection and classification. Chapter III focuses on non-statistical methods for enhancing signal-to-noise ratio. Radar and metal detectors are considered. Chapter IV turns to statistical methods. Much information can be gleaned from pixel amplitudes. By comparing measured amplitudes to a joint probability function, depth and object type can be classified. Classifying objects is addressed in Chapter V using sensor scheduling. This chapter represents a truly innovative contribution to landmine detection and classification.

Chapters VI and VII turn to the application of see-through-the-wall imaging. In Chapter VI we discuss many aspects of radar imaging and algorithm acceleration. Sparsity is explored as a method of improving image quality. In Chapter VII we model the propagation of electromagnetic waves as they pass through the inhomogeneous walls using geometrical optics. These models are used in the novel $Iterative\ Redeployment\ of\ Illumination\ and\ Sensing$ algorithm to predict locations of information gain outside the building being imaged. This information is used to schedule a small aperture imaging radar to produce a final image that approximates a much larger aperture system.

In the appendices we look at three sensor phenomenologies of importance to landmine detection. These technologies are electromagnetic induction (EMI) sensors, magnetometers, and x-ray backscatter. Chapter V discusses the application of multiple sensors in sensor scheduling. In that chapter the sensors are viewed as black boxes. These appendices illuminate the details of how these technologies work to provide information on buried objects.

In Chapter VIII we conclude this work. Discussion is made of future directions and ideas for technology transfer to real world systems.

1.3 List of Publications

The contributions made during this effort are as follows:

1. Marble,J.A., Hero,A.O., “Iterative Redeployment of Illuminatiion and Sensing (IRIS): Application to STW-SAR Imaging,” in Proc. of the 25th Army Science Conference, Orlando, FL, Nov. 2006.
2. Marble,J.A., Hero,A.O., “Phase Distortion Correction for See-Through--The-Wall Imaging Radar,” ICIP: International Conference on Image Processing 2006, Atlanta, GA, Oct. 2006.
3. Marble,J., Blatt,D., Hero,A., “Confirmation Sensor Scheduling using a Reinforcement Learning Approach,” SPIE: Detection and Remediation Technologies for Mines and Minelike Targets XI, March 2006, Orlando, FL.
4. Marble,J., Hero,A, “See Through The Wall Detection and Classification of Scattering Primitives,” SPIE: Detection and Remediation Technologies for Mines and Minelike Targets XI, March 2006, Orlando, FL.
5. Marble,J., Yagle,A., Hero,A, “Sensor Management for Landmine Detection,” SPIE: Detection and Remediation Technologies for Mines and Minelike Targets X, March 2005, Orlando, FL.
6. Marble,J., Yagle,A., Hero,A, “Multimodal, Adaptive Landmine Detection Using EMI and GPR,” SPIE: Detection and Remediation Technologies for Mines and Minelike Targets X, March 2005, Orlando, FL.
7. Marble,J., Yagle,A., Wakefield,G, “Physics Derived Basis Pursuit in Buried Object Identification using EMI Sensors,” SPIE: Detection and Remediation Technologies for Mines and Minelike Targets X, March 2005, Orlando, FL.
8. Marble,J., Yagle,A., “Measuring Landmine Size and Burial Depth with Ground Penetrating Radar,” SPIE: Detection and Remediation Technologies for Mines and Minelike Targets IX, April 2004, Orlando, FL.
9. Marble,J., Yagle,A., “The Hyperbola Flattening Transform,” SPIE: Detection and Remediation Technologies for Mines and Minelike Targets IX, April 2004, Orlando, FL.

CHAPTER II

OVERVIEW OF THE FIELD

2.1 Historical Background

2.1.1 Foliage Penetrating Radar

During the Viet Nam War, foliage penetrating radar became of high interest. Enemy assets hid beneath two canopies of jungle. The beginning of surface penetrating radar is found in this problem. The challenges that are faced are an attenuation of electromagnetic energy as it passes forward and back through the conducting jungle leaves and a random backscatter created by tiny branches. The result is a weak target signal that is obscured by random additive noise and a peppering of tree trunks [1].

In the mid-1990s, foliage penetrating radar returned as an area of research interest. Some approaches used VHF and UHF frequencies. A challenging problem is that objects such as trucks and cars can look like tree trunks at the resolution produced in VHF/UHF imagery. Some novel discriminating features were identified using directional features and by taking ratios of the UHF to VHF band energy in the backscattered signals [2] [3].

2.1.2 Unexploded Ordnance Detection

Base closures in the 1990s created an interest in detecting ordnance that had not detonated during military tests on bases scheduled to close. This unexploded ordnance (UXO) posed a health hazard to land being turned over to the public. An entire industry was spawned for environmental clean up of military bases [4] [5].

In addition to domestic cases of UXO contamination, bombs that had not exploded

during conflict were present in countries like Laos and Cambodia. Farmers plowing fields would have no problems one year, then the next would hit bombs being pushed to the surface like field stones. To this day, regions of Europe encounter UXO left over from the Second World War.

Initially, this problem generated interest in metal detection and magnetometer technology. These sensors could achieve penetration depths of several meters. However, the trade off between resolution and depth (i.e., deeper depth penetration coming only with lower resolution) led to more and more innovation. Eventually, radar began to be explored for its ground penetration capabilities. This led to Ground Penetrating Radar (GPR). Early radars in the mid-1990s were crude geophysical instruments. Today such sensors are greatly improved as they are in their third generation and have found a home as a tool for landmine detection [6].

2.1.3 Landmines

In the late 1990s much attention turned to the development of sensor technologies for landmine detection. Landmines pose a threat to soldiers during conflicts and to civilians and livestock in its wake. Over the past ten years a wealth of sensors and technologies have been proposed, developed, prototyped, and fielded. Despite all of this effort, the nature of landmines as having a wide disparity of signatures, which are affected by the state of the soil environment, has made a universal solution challenging. The signatures observed from landmines have encompassed such a rich variety that it has spawned much innovation. Among the innovations are two technology tiers. The first tier being the Standoff application and the second is the Close-in application. The reader is referred to [7] for a comprehensive overview of the landmine detection field.

Standoff Sensors

Stand-off sensor technologies for landmine detection include synthetic aperture radar [8] [9] [10] [11], microwave radiometers, and the entire family of IR (multispectral

and hyperspectral) and visible light cameras [12]. These technologies are useful as standoff sensors because they rely on the propagation of electromagnetic energy over distance. Useful IR signals have been obtained from buried landmines. These signals are caused by the warming of the mine and the surrounding ground by the sun. At night, the ground is cooler than the mine, while in the day the mine is warmer than the ground. This temperature difference creates an observable signature. Because the sun is the primary illumination source, careful study of the cycle of warming and cooling has been made. If nothing else, the goal is to predict the times of the thermal crossover when both mine and ground will have the same temperature. Other environmental effects like cloud cover and rain complicate the issue. After a rain, no signal will be present because everything has the same temperature [13].

Airborne radar systems have also been developed. These include ground penetrating radars with frequencies in the VHF, UHF, and L-bands. As well as, X-band (8-12GHz) systems that look for surface effects to detect the presence of disturbed earth. Plans for spaceborne assets for landmine detection have also been considered [14].

Close-in Sensors

There is indeed a vast set of sensor technologies for close-in detection of landmines. These include: metal detectors, magnetometers, nuclear quadrapole resonance [15], x-ray backscatter, downward looking radar [16], and chemical (olfactory) detectors. Some of these technologies are explored in the modeling presented in the appendices.

Metal detectors are the original technology for close-in landmine detection. Landmines were introduced by Germany in World War I. Since these were made with a metal casing, the metal detector became the first landmine countermeasure. (This eventually led to the development of plastic cased mines.) The technology of metal detection remains virtually unchanged. A coil of wire is energized by electric current. When the current is cut off, eddy currents continue to flow in metal objects in close proximity to the coil. This

induction effect is understood in multiple ways. Metal detectors are often referred to as electromagnetic induction (EMI) sensors [17] [18].

2.1.4 Emerging Applications

"Necessity is the mother of invention." Recent events have made for many new necessities. The public threat to air travel has brought luggage inspection to new scrutiny. A related area of interest is that of inspecting shipping containers at ports. It is desirable to inspect every container brought into port. This comes from the recent threat of global terrorism and the more traditional problem of illegal drug smuggling. The need for this type of technology does not end here. Railroad cars and transport trucks are also of interest.

Somewhat of a hybrid between container inspection and landmine detection is the search for underground facilities. This area has two tiers. One for deep structures to be detected from the air or from space. The second is that of shallow structures to be detected from the surface just above. Both are challenging problems of great interest.

Non-military applications also abound. In the biomedical field, cancerous tumor detection has been the source of much research. Bridge and infrastructure inspection for catastrophic failure is of great interest in light of recent tragedies. And, rounding out our list is the detection of buried pipes and cables. To be sure there is no shortage of problems to be solved with surface penetrating technologies.

2.2 Landmine Detection and Classification Research

In this work, two applications are given significant attention: Landmines and See-Through-Wall Imaging. New techniques and technology are often applied to the landmine problem as a first attempt at marketing. Headlines often read, "Landmine Problem Solved." The truth is, however, that landmines have been a very daunting humanitarian problem since they were first introduced as weapons.

The Uses and the Problems of Landmines

The primary goal of a landmine is to deny the enemy entry to a given region (area control). They are cheap to mass produce and effective. They are not, however, always villains. The existence of a huge minefield planted by the United States between North and South Korea has assisted in keeping over fifty years of truce. The humanitarian problems arise when the conflict ends (completely) and mines remain in the ground. Their location may not have been recorded during the war. Or, perhaps flooding has caused their location to move.

A Tale of Two Applications

Landmine research falls clearly into two categories: military and humanitarian. The challenges and goals of each are quite different. On the military side, the interest is in breaching the minefield. An army wants to go where the enemy is trying to deny. Here the application calls for a fast detection of the mines along a corridor to be traversed. The mines can be destroyed in place, or neutralized, or simply avoided. A gruesome fact is that 100% detection is not necessary for a system to be considered a success. Casualty rates must, however, be "reasonable." This can only be understood in the context of other immediate threats facing the soldiers during their minefield traversal.

The humanitarian aspect of the problem is very different. 100% detection is essential. In addition, the entire minefield must be cleared with high confidence. Also in direct contrast to the military application, humanitarian de-mining has no time constraint. The field will be declared clear when the desired confidence is achieved.

General Landmine Types

A wide range of landmines have been developed by multiple countries in the last 50 years. The most general classifications are $antipersonnel$ and $antitank$. Antipersonnel mines are small and found at shallow depth. They contain just enough explosive to kill or maim a single human. There are also antipersonnel mines that are so small as to just eliminate part of a foot. Antitank mines, on the other hand, are large and deeply buried (six inches

from surface to top of mine). They contain enough explosives to render a tank immobile. They can generally be detonated by only something as heavy as a tank. Antitank and antipersonnel mines are often found intermingled. The idea being that the antipersonnel mines will detonate, if someone tries to defuse the antitank mines.

Material composition makes up the next characterizing feature of landmines. The original versions had metallic cases. Many mines today are still made with metal casings. The original landmine countermeasure was the metal detector. The counter to this countermeasure was to build the mines with plastic casings. Some mines today contain only a slight amount of metal in the firing pin. Some plastic cased mines can still have significant metal content in the pressure plate. Therefore, mine content is described as "high metal" or "low metal".

For years the "Holy Grail" of landmine detection has been a device that could detect the explosive material itself. Quadrupole resonance, x-ray backscatter, neutron x-ray excitation, and olfactory (sniffer) sensors have all been designed with this in mind. To date, however, these systems have not made it past the experimental stage. Fielded systems still target some aspect of the surroundings of the landmine rather than the explosive material itself.

2.2.1 Low Signal-to-Noise Ratio

The cutting edge of landmine detection is defined by the depth at which a landmine can be detected. In recent conflicts objects buried at significant depths have become of high priority. Achieving depth with high resolution is necessary to extract image information about the object. The classic GPR trade off is that lower frequencies achieve greater depth of penetration but at the cost of resolution.

2.2.2 False Alarm Rejection

Since the primary detection characteristic is the landmine casing, false alarms are often generated by non-threatening objects that exhibit the same characteristic. An important

area of research is the ability to properly identify threatening objects while rejecting harmless ones. Thus, false alarm rejection is an object classification problem.

Sensor Fusion

Because landmines have such a wide variety of signals, a real world landmine detection system must employ multiple sensor technologies. This can take many forms. A standoff system may queue a close-in detector to investigate a particular location. A system of two or three sensors may measure simultaneously in a scanning sense. Or a system with a lever arm may deploy a sensor that has been selected based on previous observations. The phrase $multimodal\ system$ has come to refer to one that can modify its mode of sensing to remove detection ambiguity [19].

Because landmine signatures are affected by changing environmental conditions, a successful landmine detection system will have to be able to adapt. An adaptive system is one that allows algorithms to vary based on the surrounding environment. Wetness of the ground is a randomly varying quantity. It has been shown that this parameter needs to be observed constantly for proper GPR operation.

Confirmation Sensors

Some of the technology developed for landmine detection has matured and can be implemented in sensor arrays that scan for landmines. Other technologies show great promise for distinguishing landmines from clutter, but are more practical to implement on a point-by-point basis as confirmation sensors. Confirmation sensor scheduling has arisen as a research topic to determine the optimal allocation of the many sensor resources at hand.

Sensor Scheduling

Artificial Intelligence has spawned the concept of algorithms that learn over the course of their lifetimes. Sensor Scheduling is a sub-field of algorithms that attempts to learn a

policy for applying the right sensor at the right time. Chapter V discusses this in more detail in regard to the landmine detection application.

2.3 See-Through-Wall Radar Imaging

The latest twist in the story of surface penetrating radar is the See-Through-Wall (STW) application . STW radar imaging refers to the imaging of objects behind walls or inside buildings. The application has become of increased interest in recent years for both military and law enforcement applications. Ultimately it is desired to provide the most useful information possible to authorities. The nature of this information includes the internal layout of a building (location of doors, obstructions, or inner rooms), the existence and location of objects of interest (weapons, explosives, methamphetamine labs), and the tracking of suspicious individuals inside [20].

Imaging Challenges and Issues

The most useful tool for this application is radar. Radar observations of a building can be used to form 3D volumetric images of the building interior. This application is challenging, however, because it requires the processing and interpretation of electromagnetic waves in an inhomogeneous media with unknown material parameters and structures. Standard imaging techniques suffer from multibounce effects. That is, energy bounces back and forth between walls or inside walls making the image difficult to interpret [21] [22] [23] [24].

Suspicious Individual Tracking

Tracking individuals inside a room faces a signal-to-noise ratio challenge. Nevertheless, recent work has shown that this can be accomplished using STW radar. Law enforcement desires to know the location of individuals in a room at the moment they force entry. In a hostage sitaution, if they can determine the location of the captive and the captor, the chances of a safe hostage extraction increases greatly.

Inner Wall Mapping

Along the same line of thought, it is desired to know the layout of the structure being entered. Mapping doorways to other rooms identifies the direction of possible gun fire. Wall mapping has been shown to be difficult. Again low signal-to-noise ratio plays a large part. Walls that are not directly illuminated by the radar beam cause the RF energy to bounce away from the radar (in the monostatic case). The result is a scene revealing walls perpendicular to the beam, but without ones that are parallel or angled to it. A practical system may have to collect data from two directions and merge the information to properly map all inner walls [25] [26].

CHAPTER III

NON-STATISTICAL APPROACHES

Surface penetrating technology often suffers from low signal-to-noise ratio and/or low resolution. In this first contribution chapter we look at non-statistical methods for extracting information about landmines from ground penetrating radar (GPR) and metal detectors. The first section deals with low resolution. It uses computer vision tools to segment a radar scene into object and background regions. A bounding box is then drawn around the object to identify it as being of the right size and depth. Section 3.2 addresses the issue of low SNR in GPR data by introducing a novel transform. This transform dubbed the $Hyperbola\ Flattening\ Transform$ collapses all the energy of a GPR point spread function into a point allowing for the best achievable SNR. Section 3.3 turns to electromagnetic induction (EMI) metal detectors. This technology, despite its simple nature, has stood the test of time. In this section we look at the extraction of depth and rudimentary shape information from the metal detector signal. This technique is a basis pursuit, which can be used to eliminate noise. Since plastic cased landmines can have very metal only in their firing pins, this technique is of high interest.

3.1 Imaging Using Ground Penetrating Radar

The Wavenumber Migration imaging algorithm decribed in Chapter VI will be applied to real world data collected with a GPR. All signatures shown in this section are from a Russian made TM-62M landmine buried at 6". The TM-62M is an anti-tank mine that is typically buried at a depth between 4" and 8". This particular variant has a metal casing,

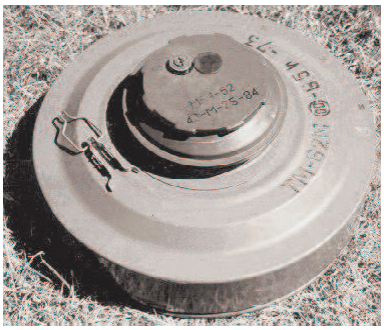

Figure 3.1: A TM-62M, Metal Cased Landmine (Dimensions: hgt. - 6”, dia. - 13”)

which gives a very strong signature.

Ground penetrating radar images are inherently low resolution. High resolution imagery requires high frequency E&M waves. These higher frequencies are strongly attenuated by the conductivity of the ground. Lower frequencies can penetrate the soil further, but the landmines have lower reflectivity at these lower frequencies. Thus, the problem of designing a radar to detect landmines is sandwiched by lack of returned energy at lower frequencies and lack of penetrating energy at the higher frequencies. The frequency range we are left with tends to be in the upper UHF and L-bands. That is, around $500MHz$ to $2GHz$. With these wavelengths it is possible to obtain resolutions of around 2” in depth. The TM-62M is 6” high. This means that when looking downward in depth we are likely to get around three pixels between the top of the mine and the bottom.

Figure 3.1 shows a typical TM-62M landmine. A hyperbolic signature observed from a similar TM-62M at 6” depth is shown in Figure 3.2. The soil here is Virginia clay, which is known for being quite lossy. The exact relative permittivity and conductivity values are unknown. The signatue here appears at a false depth due to uncalibrated delays in the GPR. (The wavenumber migration algorithm will correct this during imaging .)

In Figure 3.3 we see the results of imaging this signature with the wavenumber migration algorithm. Note that the low resolution image is dominated by two horizontal lines. These lines are 6” or 7” apart and roughly 12” or 13” in length. The upper line is caused by the energy reflecting from the top of the mine while the bottom line is the energy

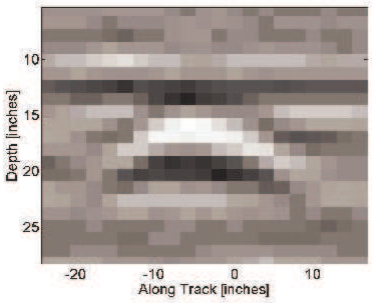

Figure 3.2: Observed Signature of a TM-62M (Depth: 6” to top)

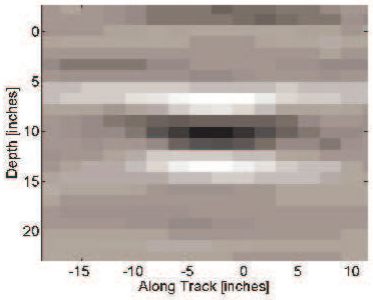

Figure 3.3: Image After Wavenumber Migration - Size of reflections reveals the depth, height, and diameter of the landmine.

reflecting from the bottom. Note the low return area (shadow) in between. Since this is a metal-cased mine, little energy gets into the mine itself, producing a shadow region.

The final image in Figure 3.4 shows a thresholded version of this signature. The top and bottom edge returns clearly dominate the signature. The exact threshold values were chosen arbitrarily but consistently for all the signatures analyzed in this study. From this binarized image the height of the mine can be seen to be around 7”. The length of the upper reflection is about 17” while the length of the lower reflection is about 12”. The depth to the top is 6”. This is very close to the actual 13” diameter, 6” height, and 6” burial depth of the mine.

3.1.1 Size and Depth Estimation Algorithm

In Section 3.1 we estimated the size of the landmine by visual inspection of the focused signature. For the purpose of automatically determining the landmine’s size and making a

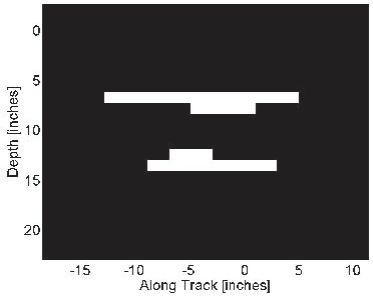

Figure 3.4: Binarized Image of Fig. 3.3 - Reflections from the top and bottom of the landmine are visible.

decision based on that information, an automatic estimation algorithm has been created.

Identifying the Top and Bottom Scatterers

Using a standard vision system approach it is possible to automatically identify the top and bottom scatterers. The algorithm requires setting a threshold on the real part of the complex focused image. Next, all pixels breaking the threshold are lumped into objects. In vision system literature these are called Binary Large Objects (BLOBs). Any BLOB found at a depth that is above the ground is eliminated. These objects are associated with multiple reflections from the landmine that are aliased into false locations by the radar sampling process. Next, the two objects that have the greatest size-brightness product are identified. (The size-brightness product feature that is computed is the number of pixels in the BLOB times the value of the brightest pixel on the blob.) In all ten signatures of the repeatability study of Section 3.1.2, the two BLOBs with the largets size-brightness product corresponded to the top and bottom edge reflections.

Figures 3.5 and 3.6 illustrate the process. Figure 3.5 shows the original focused image. The thresholding reveals several bright scatterers. In this case several BLOBs were reported at impossible depths. That is, they were reported to be above the ground. These objects are eliminated from the object list. In other cases not shown here, BLOBs that were not associated with the top and bottom of the mine were dimmer and smaller than the correct ones. So there was little difficulty in automatically choosing the correct BLOBs.

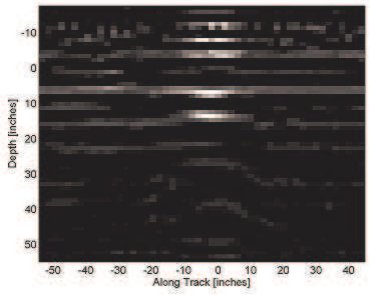

Figure 3.5: Focused Image of TM-62M Landmine

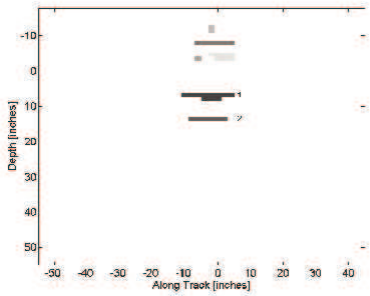

Figure 3.6: Fig.3.5 After Thresholding

It should be noted that this landmine is a large metal landmine. Despite the fact that it is buried relatively deeply, it still gives a very high signal-to-noise ratio. This is common to all metal objects.

The depth of the landmine is determined from the location of the top reflection. Similarly, the height is estimated from the distance between the top and bottom reflections. The length is computed by averaging the lengths of the top, bottom, and shadow region BLOBs. The shadow region is described in the next section. This particular example is entry Number 5 in Table 3.1 of Section 3.1.2. The sizes automatically determined were: height - 6.8”, depth - 6.7”, length - 13.3”. The actual values of these dimensions are listed in Figures 3.1 and 3.2. Actual values: height 6”;depth 6”; length 13”.

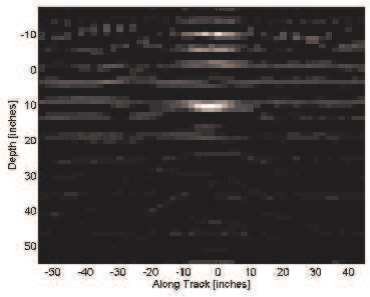

Figure 3.7: The negative of the focused image converts the shadow region into a bright one.

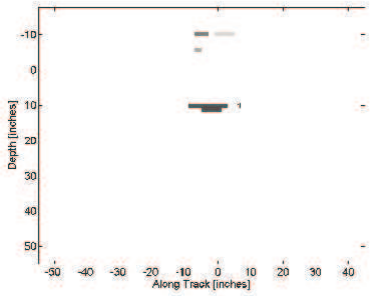

Figure 3.8: Shadow region is automatically identified and labeled 1 by the algorithm.

Utilizing the Shadow Region

For metal landmines the real part of the focused image can be inverted to detect the shadow region. In the preprocessing step the data is high pass filtered. This has the effect of removing the average value. The average value of the background is created by energy that is reflected from the soil filling the medium. When this average is removed by the high pass filter, the shadow region ends up being negative. By multiplying the real part of the image by -1 and then going through the algorithm described in Section 3.1.1, a BLOB associated with the shadow region can be identified.

The existence of the shadow region also provides a confidence check. If the algorithm returns a shadow region that is not located spatially between the upper and lower reflections, then an error has occurred. The signature is not being produced by a large, metal landmine.

3.1.2 Algorithm Validation - Repeatability Study

Validation of the imaging and size & depth estimation algorithms involves focusing an image for multiple targets of known size and depth, performing the estimates, and then comparing to the ground truth of these objects. As an initial test, ten targets were selected from multiple measurements of the same buried landmine. The TM-62M landmine chosen was buried at 6". All 10 signatures studied are from independent measurements of the same TM-62M. All 10 were measured within 3 days of each other. There were no significant changes in weather during these 3 days, so it is expected that the ground permittivity will be relatively constant for all 3 days.

By trial and error the relative permittivity of the ground was determined to be 3. (This is the real part of the relative permittivity.) This value was used to image each hyperbolic signature. After performing the size and depth estimation on the real part of the focused images, Table 3.1 was produced. The results are encouraging. On average the method determined the height and depth of the landmine to within a standard deviation 0.55". On average the estimates were too high by 0.5" and 0.4" inches for height and depth. Because the soil was determined to have a dielectric constant of 3, the depth resolution of the system making these estimates was 1.13". The estimates are, therefore, accurate to within one resolution cell.

The performance of the length estimator was not quite as accurate. On average the algorithm determined the length of the 13" diameter landmine to be 11.6". This is too small by 1.4". The standard deviation of these estimates was 2.54". If we assume that the radar beamwidth was roughly $\pm 45°$, the azimuth resolution will be roughly 1.3". So the length estimate bias is on the order of one resolution cell.

These results are encouragingly consistent. It is clear from the data that the length estimate is the more difficult quantity to measure accurately. However, our estimates are still within 1.5" on average and within 2.5" in standard deviation for a 13" object. The burial depth and height measurements, on the other hand, are quite accurate. On average

Table 3.1: Summary of Estimates - All units in inches.

	Estimates			Error		
Number	Length	Height	Depth	Length	Height	Depth
1	9.3	6.8	6.7	-3.7	0.8	0.7
2	11.3	6.8	5.6	-1.7	0.8	-0.4
3	12.0	6.8	5.6	-1.0	0.8	-0.4
4	18.0	6.8	5.6	5.0	0.8	-0.4
5	13.3	6.8	6.7	0.3	0.8	0.7
6	10.7	5.7	6.7	-2.3	-0.3	0.7
7	10.7	5.7	6.7	-2.3	-0.3	0.7
8	9.3	6.8	6.7	-3.7	0.8	0.7
9	10.7	5.7	6.7	-2.3	-0.3	0.7
10	10.7	6.8	6.7	-2.3	0.8	0.7
Average	11.6	6.5	6.4	-1.4	0.5	0.4
St. Dev.				2.54	0.55	0.55

our estimates of depth and height are within a half inch for a system that measures depth and height with a resolution of around 1”.

This section has shown how ground penetrating radar can collect and process information into low resolution images of objects buried in the ground. By the term ”low resolution” it is implied that only a few pixels are available on the targets of interest. In this application, a 6” tall landmine is resolved with 1.5” resolution, so only about 4 pixels will exist from the top of the landmine to the bottom. However, despite the low resolution characteristic of the data, information regarding the size and depth of the landmine can still be extracted with reasonable accuracy.

The wavenumber migration imaging technique was applied to a TM-62M landmine buried at 6”. In the resulting focused image, reflections from the top and bottom edges of the landmine could be clearly seen. These reflections appeared as parallel, horizontal lines in the final imagery. Computer vision techniques were applied to extract these two reflections and the low return (shadow) region in between. These three objects were then used to compute the depth, length, and height estimates.

An initial study of accuracy was then performed on 10 signatures collected over the same landmine. In all cases the automatic estimation algorithm correctly identified the edges of the landmine and computed estimates. The results showed that depth and height were easier to estimate than length. The depth and height estimates were accurate to

within 0.5” in bias and standard deviation. This standard deviation implies depth and height measurements to within $\pm 10\%$ of the actual values. The length measurement was accurate to a bias of 1.4” and a standard deviation of 2.5”. This is an accuracy of about $\pm 20\%$. Greater sophistication in the estimation algorithms will likely reduce these errors.

A spent rifle cartridge shaped like a cylinder that is 1” long and 0.25” in diameter lying on the surface will generate a large response in a metal detector. The GPR working in combination with the metal detector will be able to determine that this object’s size is not in the proper regime. Using size and depth information, objects that are too big/small and too shallow/deep to be consistent with landmines can be removed from detection lists as non-threatening objects [27] [28] [29].

3.2 Pseudo Imaging

Vehicle mounted ground penetrating radars transmit RF energy into the ground from a short distance above. In the area of landmine detection the goal is to detect landmines located just inches below the surface. The frequencies used tend to be relatively low to allow for necessary penetration. This combination of geometry and low wavelength leads to the generation of a unique signature that can be exploited in GPR data. The signature has a characteristic hyperbolic shape as shown in Figure 3.9.

Soil has a tendency to be horizontally layered. In GPR data this horizontal layering manifests itself as straight, horizontal lines in the data. False detections are often caused in GPR systems by a change in the horizontal layering of the ground. These changes, however, do not appear as a hyperbolic signature in the data. This means that the hyperbola generated by discrete objects like landmines can be utilized as a powerful discriminant against ground layer induced false-alarms. For this reason many GPR users perform detection processing on un-imaged data. Imaging of landmines eliminates the hyperbolic shape by resolving the energy of the signature into a low resolution image.

Here we present an algorithm that takes advantage of the hyperbola by utilizing all the

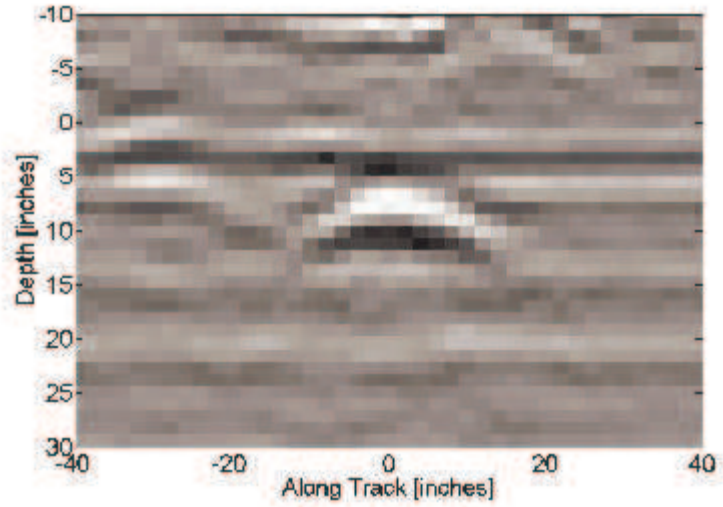

Figure 3.9: Characteristic Hyperbolic Signature of a Landmine Measured by GPR

energy contained in the hyperbolic shape. The algorithm is called the Hyperbola Flattening Transform because it ”flattens” the hyperbola into a line prior to summing the line into an energy value. This energy value can then be compared to other objects as a measure of the ”hyperbola likeness” of the signature.

3.2.1 Algorithm Discription

Many approaches have been used to exploit the hyperbolic signature produced by discrete scatterers in GPR data. Typically these approaches have tried to extract the energy from the left and right ”tails”, and then combine them in some way to estimate the total energy [27]. An elegant approach has been developed for capturing the total energy of the hyperbola in one step. This approach is called the ”Hyperbola Flattening Transform”. It is a virtual warping of space that converts the curved hyperbola into a straight line. Total energy can then be estimated by summing this line.

Equation 3.1 is a general second order polynomial equation that appears in the study of conic sections [30]. Based on the values of A,B,C,D,E, and F the equation can describe a hyperbola, a parabola, a circle, or an ellipse. The resulting geometric shape results from

the choice of these coefficients. For example, choosing A=1, B=0, C=1, D=0, E=0, F=-1 causes the resulting equation to describe the unit circle.

$$AX^2 + BXY + CY^2 + DX + EY + F = 0 \tag{3.1}$$

The hyperbola shown in Figure 3.9 can be modeled mathematically by:

$$-\frac{X^2}{a^2} + \frac{Y^2}{d^2} = 1 \tag{3.2}$$

Y in this equation is the depth direction. (Y is positive down for increasing depth as shown in the figure), X is the horizontal direction, and the parameters a and d control location and convexity. Note that this expression models both halves of the hypberbola - the upward and downward convex curves. In the case of the landmine signatures, we only have the curve that is below the ground. This is the (mathematically) upward convex curve, because Y (depth) is increasing in the downward direction. So, the other half of the hyperbola does not exist in our application.

The idea of the Hyperbola Flattening Transform is to modify the geometry of the hyperbola of Equation 3.2 so it is described as the following:

$$XY = 1 \tag{3.3}$$

Equation 3.2 is an expression of a hyperbola. It is a conic section with: $A = \frac{-1}{a^2}$, $B = 0$, $C = \frac{1}{d^2}$, $D = 0$, $E = 0$, $F = -1$. However, Equation 3.3 is also a hyperbola. It is a conic section with: $A = 0$, $B = 1$, $C = 0$, $D = 0$, $E = 0$, and $F = -1$. Once the signature is transformed into $XY = 1$, we can do a change in variables of $Y \rightarrow \frac{1}{Z}$ to produce $X = Z$. This is a straight line at $45°$. With the signature "flattened" into a line, it is easier to construct algorithms to sum up the energy it contains.

The transformation of the data from the form of Equation 3.2 to the form of Equation 3.3 is accomplished by the following steps:

1) Scale the dimensions:

$$X' = \frac{\sqrt{2}X}{a} \qquad Y' = \frac{\sqrt{2}Y}{d} \tag{3.4}$$

Equation 3.2 now becomes:

$$-\frac{X'^2}{2} + \frac{Y'^2}{2} = 1 \tag{3.5}$$

2) Equation 3.5 can be factored into the following expression:

$$\left[\frac{X'}{\sqrt{2}} + \frac{Y'}{\sqrt{2}}\right]\left[-\frac{X'}{\sqrt{2}} + \frac{Y'}{\sqrt{2}}\right] = 1 \tag{3.6}$$

3) Rotate by $-45°$:

$$X'' = X'cos(-45°) - Y'sin(-45°) = \frac{X'}{\sqrt{2}} + \frac{Y'}{\sqrt{2}} \tag{3.7}$$

$$Y'' = X'sin(-45°) + Y'sin(-45°) = -\frac{X'}{\sqrt{2}} + \frac{Y'}{\sqrt{2}} \tag{3.8}$$

4) Substitute X'' and Y'' into Equation 3.6:

$$X''Y'' = 1 \tag{3.9}$$

We now have the hyperbola in the same form as Equation 3.3. At this point the Y'' axis is inverted to produce a line.

5) Invert the Y'' axis:

$$Z = \frac{1}{Y''} \tag{3.10}$$

$$X''Y'' = 1 \rightarrow \frac{X''}{Z} = 1 \rightarrow X'' = Z \tag{3.11}$$

Note that the expression shown in Equation 3.12 is a line with slope 1 and Z-intercept 0. That is, it is a straight line at $45°$.

$$X'' = Z \tag{3.12}$$

By transforming the geometry into this form, the hyperbola has been ”flattened” into a line. Now the radon transform can be used to sum along all angles to obtain the energy contained in the entire signature.

3.2.2 Results on Simulated Data

The concept put forward in Section 3.2.1 is relatively simple. But the implementation can be tricky. Below is a simulation that illustrates the process giving a proof-of-concept. The starting point for creating a simulation is to define an X,Y coordinate system and ”turn on” pixels according to the expression of the hyperbola of Equation 3.2. That is, for every X location the pixel given by Equation 3.13 are set to ”1”.

$$Y = \sqrt{d^2 \left(\frac{X^2}{a^2} + 1 \right)} \tag{3.13}$$

The result is a hyperbolic shape in the same ”observation space” as that obtained by the GPR. The first step in implementing the HFT is to normalize our axes to remove the

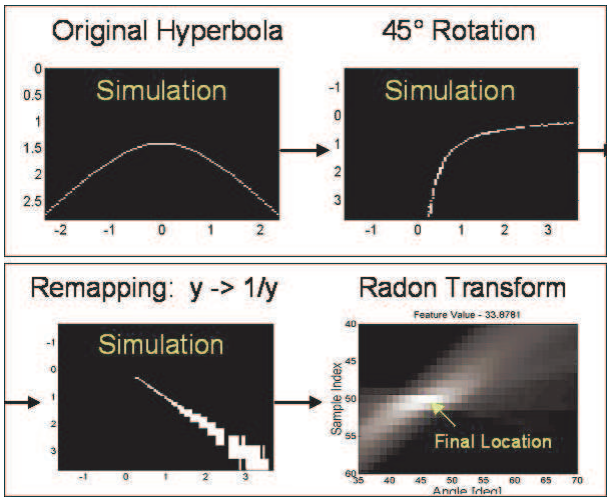

Figure 3.10: Steps of the HFT Applied to a Simulated Hyperbolic Signature

parameters a and d. This means that a and d must be known (or estimated) before the algorithm will successful produce the flattened signature. Figure 3.10a shows the scaled version of the hypberbola.

After scaling the axes, the -45 rotation is achieved by rotating the image. The axes are then redefined as X' and Y'. The result is Figure 3.10b. The Y' axis is now inverted to $frac1Y'$ to generate the Z dimension. This is a non-linear mapping, which means that the samples that were uniformly spaced in the Y dimension are now non-uniformly spaced in the Z dimension. To get back to uniform sampling, the data is interpolated in the Z dimension onto a rectangular grid. The result is shown in Figure 3.10c. Note that the signature is now a line at a 45 angle. If the a and d parameters are properly removed, the hyperbola will always be converted to this orientation. Notice that the line begins at the location (0,0) in (X,Z) space and proceeds to the most positive values of X and Z (i.e. the lower right corner of Figure 3.10c). The line does not continue on the other side of (0,0) to the most negative values (upper left corner). This is because only the half of the hyperbola that corresponds to the below ground landmine signature was simulated. The half that we ignored would fill in a straight line in the upper left corner of the image.

Now that the hyperbola has been flattened to a line, it can be more easily exploited to obtain the total energy in the signature. Figure 3.10d shows the result of performing

a Radon Transform on the image of Figure 3.10c. Recall that a Radon Transform will sum the values of an image along lines oriented at specified angles between $0°$ and $180°$. Looking at Figure 3.10d the $45°$ line sums to a point at the $45°$ angle index of the Radon Transform. Since the HFT requires the hyperbola to be normalized properly to always generate the $45°$ line, this location in the Radon Transform will always contain the energy of the hyperbola.

3.2.3 Results on Real Data

Section 3.2.2 provided a proof of concept for this algorithm. It showed that, when applied to perfect data, the HFT will produce a flattened hyperbola that can be summed into a point using the Radon Transform. In this section the HFT is applied to the real world hyperbolic signature of Figure 3.9. The result shows that the energy is summed up in the same way as predicted in Section 3.2.2.

First, the values of a and d were determined for the hyperbola of Figure 3.9. The parameter d is related to the depth of the landmine. The parameter a is more complicated as it is related to both the depth of the landmine and the relative permittivity of the soil. Figure 3.11a shows the signature with the a and d parameters removed by the normalization step (Step 1 in Section 3.2.1). Figure 3.10b shows the $-45°$ rotation of Step 3. Figure 3.10c shows the remapping to the inverted vertical coordinate. A line at $45°$ is visible.

Because the beamwidth of the GPR used in this application is small, the extent of the hyperbola is small. The result after flattening is a rather small line at $45°$. Regardless, Figure 3.11d shows the radon transform with the summed energy from the hyperbola landing at $45°$ in the Radon Transform image.

3.2.4 Applications

Two potential applications exist for the Hyperbola Flattening Transform. The first is as a false alarm discrimination feature. Detections that have been located by some other means

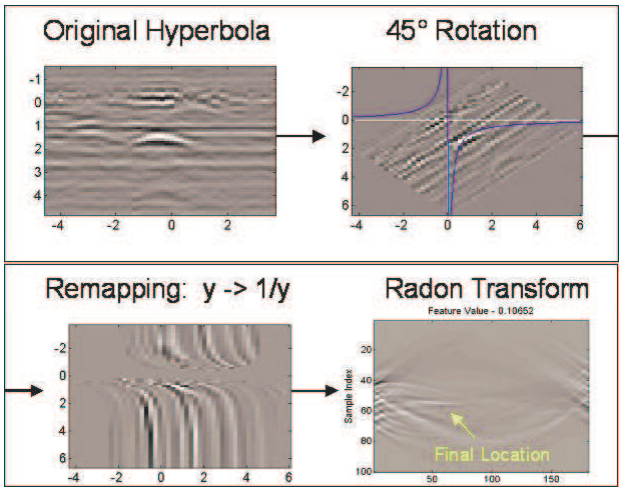

Figure 3.11: Steps of the HFT Applied to an Actual Hyperbolic Signature

or other sensor can be analyzed one by one to determine their characteristics. The HFT is a measure of hyperbolic-likeness. This measure is useful in determining if a detected object is a discrete object or a change in the background. The other application is in enhancing the contrast of low signal-to-noise ratio landmines during the detection process.

Plastic landmines that are buried deeply are particularly difficult to detect due to low signal-to-noise ratio. Figure 3.12 is an example of an Italian VS1.6 landmine buried at 6" (to the top of the mine).

The hyperbolic signature is visible, but is weak. The magnitude of its reflection is less than the reflection from a stratification layer of the earth also visible in Figure 3.12. The goal of the HFT is to change the contrast of the image so the stratification signal is less than the VS1.6. Figure 3.13 shows the results of applying the HFT to every point in the image with an a parameter of 17. (This value of a corresponds to the relative permittivity of this soil and an object at 6" depth.) The results show some promise. The earth stratification signal is almost removed from the data, while the VS1.6 is enhanced. Figure 3.14 shows the 20% brightest pixels in the transformed data. The location of the VS1.6 is among the strongest pixels. A detection scheme used in some GPR applications is to find the standard deviation in the returned echoes. This is equivalent to computing a standard deviation over all the pixels in a vertical column. Figure 3.15 shows that this technique applied to the

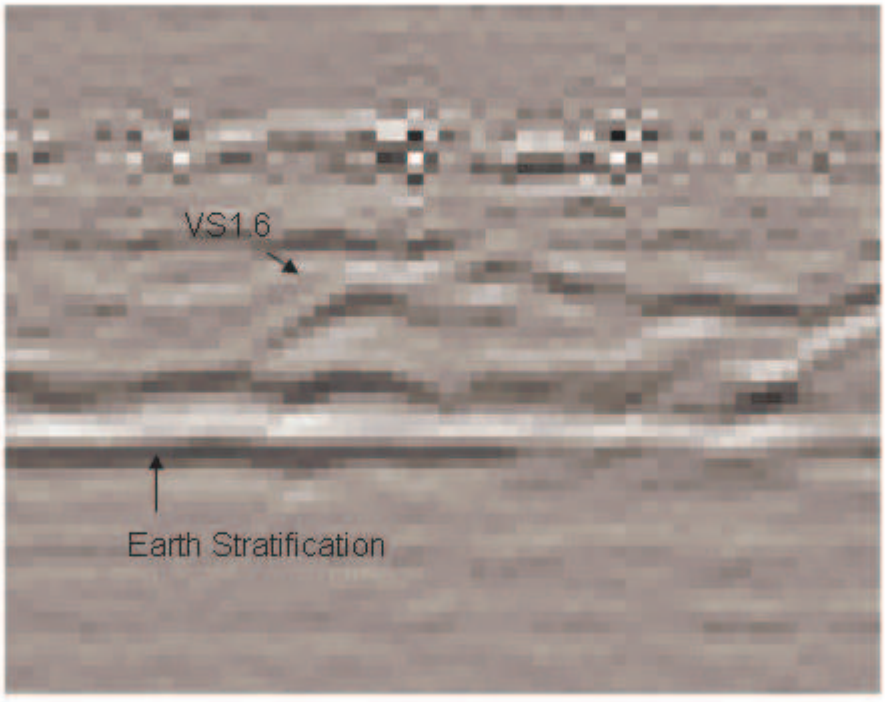

Figure 3.12: Italian VS1.6 Landmine at 6” Depth

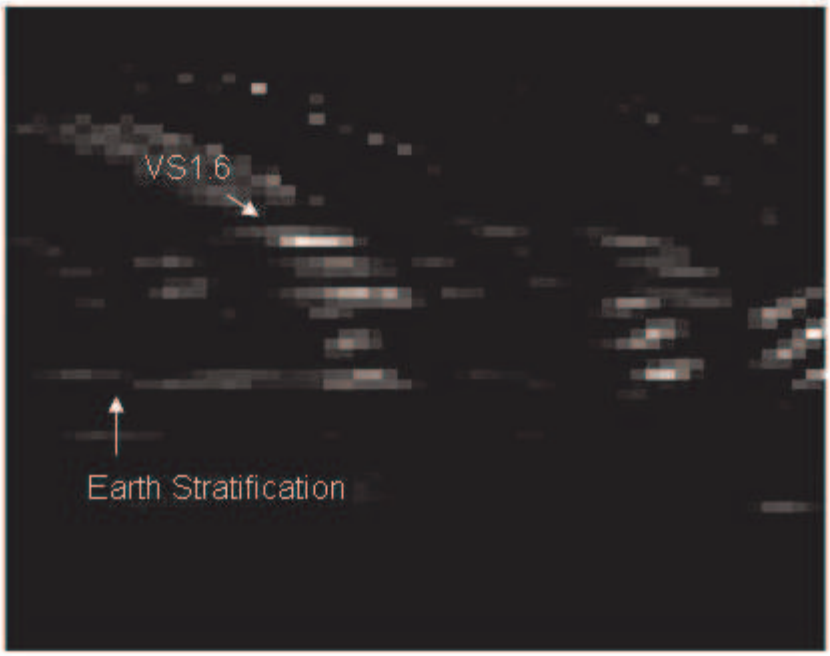

Figure 3.13: The HFT Applied to Every Point of the Image

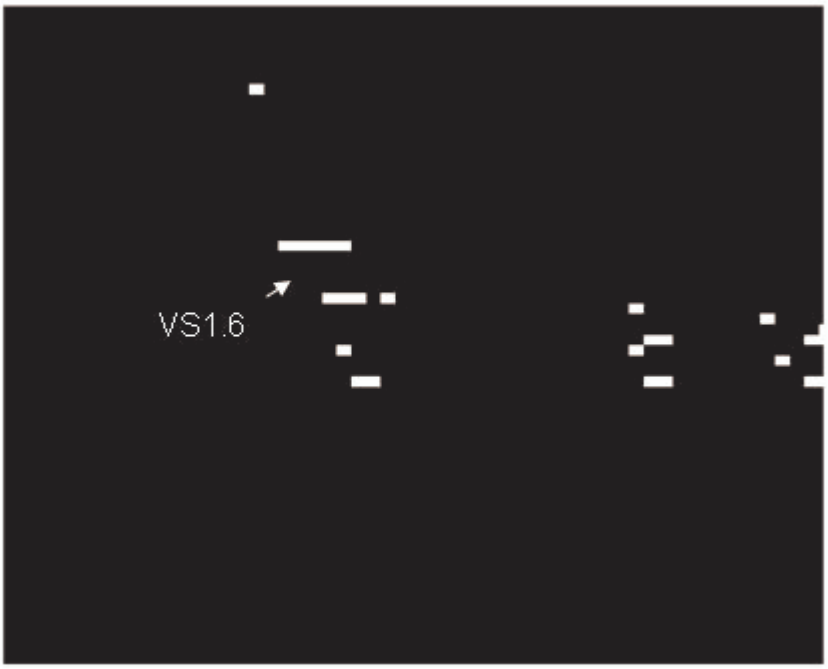

Figure 3.14: The 20% Brightest Pixels of the Transformed Data

HFT image shows a strong indication of an object at the location of the VS1.6.

3.2.5 Pseudo Imaging Conclusions

A novel way of processing GPR signatures has been introduced called the Hyperbola Flattening Transform. The algorithm utilizes the mathematics of conic sections to transform the hyperbola into a line. The line can then be exploited using the Radon Transform to produce a feature value for use in discrimination of false-alarms and detection of low signal-to-noise ratio objects. This feature value can be thought of as a summation of all the energy contained in the hyperbolic signature. After applying the HFT to a VS1.6 buried at 6", encouraging results were obtained. This is a plastic mine and is buried deeply. The transformed data showed an enhancement of the landmine's signal while diminishing other signals caused by the stratified earth [31].

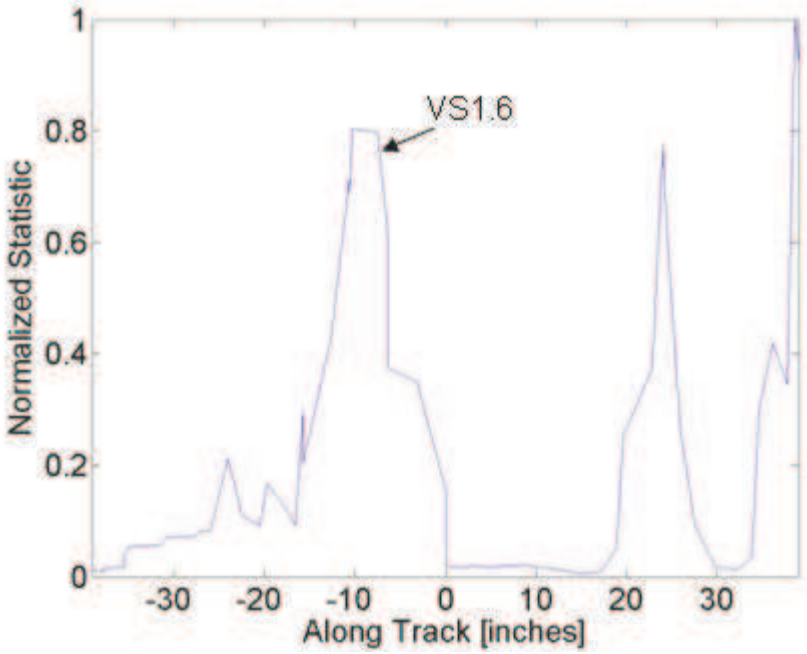

Figure 3.15: Vertical Standard Deviation Showing Location of the Most Hyperbolic Signatures

3.3 Subspace Methods

In the previous two sections the focus was on ground penetrating radar. Now we switch to the other mature sensor technology for landmine detection - metal detectors. The metal detector has been called a "monkey wrench" sensor. This is because of its inherent low resolution. Its resolution is so low that is is almost a binary sensor providing a 1 when metal is present and a 0 otherwise. Close inspection of the physics, however, does show that some information about the depth and shape of the object can be extracted.

3.3.1 Depth and Shape Information

For years, treasure hunters have used Electromagnetic Induction (EMI) metal detectors to search for buried objects. An investigation of the physics of these devices reveals an understanding of the principal components contributing to the received signal. The spatial signal from any buried metal object can be decomposed into two basis functions. These bases are produced by orthogonally oriented magnetic dipole sources induced in the buried

object. Because of their characteristic appearance, the two bases have been called the Λ and W basis functions. Since the induced sources behave like point sources, the Λ and W basis functions are the same for all objects at the same depth. The object's shape and metal content determines the weighting of Λ and W, which sum to produce the spatial signal received by the metal detector.

The fact that all objects at the same depth can be represented as the summation of two basis functions implies that the signal exists in a two dimensional vector subspace. Identification of the subspace reveals the depth of the object. Once depth is known, the basic shape of the object can be determined by the signal components. The metal content (i.e., conductivity) and object size can be estimated by the components' magnitude.

Two applications of this signal representation are explored. First, a projection method is used to estimate object depth. This method utilizes a projection matrix that projects a normalized signal into the subspace of a "shallow", "mid-depth", and "deep" object. After the projection is made, the l_2 norm of the sampled signal is computed. This norm is a measure of the energy of the signal that "survived" the projection. In a world without noise, the subspace corresponding to true depth will not reduce the signal energy at all. 100% of the input signal energy will be found in the projected signal. When noise is present, the true depth will still be revealed by the projector that rejects the least amount of energy. (That is, only the energy contained in the additive noise will be rejected.)

The second application involves determining the object's shape through estimation of the object's directional polarizability. Accurate estimation of polarizability requires knowledge of the object's depth. In other words, it is necessary to know the correct signal subspace within which to make the estimates. (The depth could be provided by the proposed projection algorithm just mentioned or through the use of an alternative sensor like a ground penetrating radar.) Once depth is known, the object shape is identified by estimating the polarizability of the object in the horizontal and vertical directions.

Computer simulations are used to test the two applications. Signals corresponding to

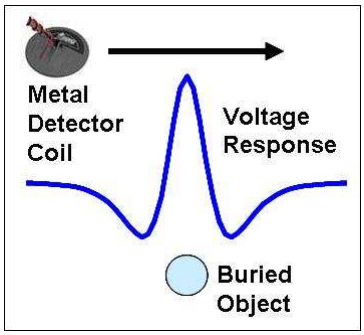

Figure 3.16: Typical EMI Spatial Signal - 1D

spheres, cylinders, and flat plates buried at 0.0, 0.25, and 1.0m are produced. In Section 3.3.3 results are shown for predicting the depth of each object in a world with and without noise. In Section 3.3.4 polarizability estimates are made with and without noise. It is shown that accurate estimates of the polarizability are achieved as long as the object depth has been properly determined.

3.3.2 The Λ and W Basis Functions

When a metal detector passes over a buried metal object a signal like the one shown in Figure 3.16 is produced. The signal shown is a simulation of a metal detector held 0.3 m (i.e. 1ft) above the ground. The object is a sphere of radius 0.15m buried at 0.25m to its center. This signal and all other received signals (from objects at 0.25m depth) can be represented as a weighted sum of the two bases shown in Figure 3.17. The shape of these functions has led them to be named the Λ and W basis functions.

These functions arise due to the phenomenology of the magnetic fields generated by the metal detector. A metal detector is fundamentally a coil of wire that is driven by an electrical current. The current is generally sinusoidal with a frequency on the order of 100 Hz [32]. This field interacts with the buried object. To satisfy the electromagnetic boundary conditions, electrical currents are set up within or on the surface of the object. The details of these currents are quite complicated and depend greatly on the shape of the object. However, an approximation to the object's response is an induced magnetic

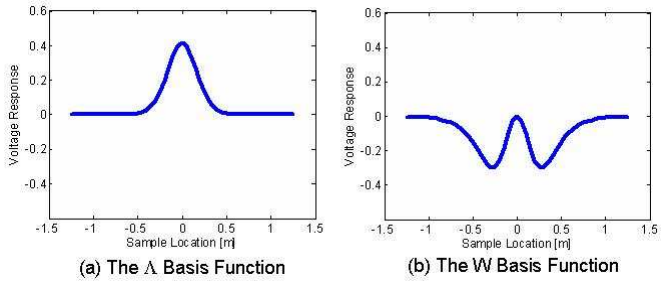

Figure 3.17: The Λ and W Basis Functions

dipole [33]. Because higher order effects in magnetics have a very fast spatial decay rate, the contribution of the more complicated physics is not observed by the metal detector. As far as the metal detector is concerned, the buried object is just a magnetic dipole source. This source will have components in both the vertical and horizontal directions. The magnitudes of these dipoles change as the sensor passes overhead. The Λ and W basis functions take into account these changes. The weightings of the two bases come from the polarizability of the object.

That is, the tendency of the object to allow a magnetic dipole to exist in the vertical and horizontal directions. The polarizability values are always constant no matter where the sensor is located with respect to the buried object. This implies that the polarizability can be estimated and used as a rough measure of object shape.

$$s(x) = a\Lambda_d(x) + bW_d(x) \tag{3.14}$$

The shape of the buried object affects its polarizability. For instance, a sphere has no inherent directionality. So, the polarizability is equal in all directions. A flat plate, on the other hand, will allow the swirling currents induced by the sensor to exist on its flat surface. If that surface is parallel to the earth's surface, then there will be a large vertical dipole response. The area of the flat plate perpendicular to the horizontal is very small. It does not allow much current to flow so the horizontal polarizability of the plate is quite small. (See Section 3.3.4 for more discussion.)

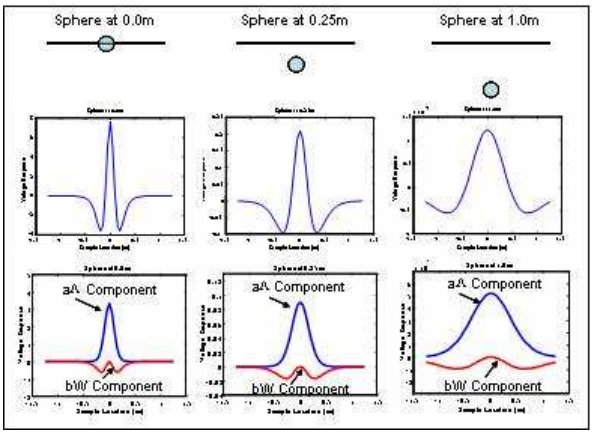

Figure 3.18: Signals from Spheres at Canonical Depths

The depth of the buried object affects the width of the basis functions. The magnetic fields emitted by the metal detector are highly non-linear with distance. That is, they fall-off quickly as the distance from the detector increases. (For this reason, metal detectors are inherently "close-in" detectors. They cannot perform from a large standoff distance.) The result is a broadened spatial signal. (See Section 3.3.3 for more discussion.)

3.3.3 Subspace Identification

In this section the Λ and W functions for buried objects at 3 depths are considered. These functions are referred to as: Λ_1,W_1,Λ_2,W_2, and Λ_3,W_3, where the subscripts 1,2,3 refer to shallow, mid-depth, and deep objects respectively. No matter what the shape or metal type of the object, all objects at the same depth will have the same Λ_i and W_i basis functions. The Λ_i and W_i span a 2D signal subspace (i.e. a plane) that contains all signals coming from objects at the same depth. (The shape and metal content impact the coefficients that weight the two basis functions. This will be discussed in the $Shape\ Identification$ section below.) Figure 3.18 illustrates the signal from a buried sphere at three canonical depths. The depths are: shallow (0.0m), mid-depth (0.25m), and deep (1.0m).

Given a measurement of an unknown signal, it is desired to determine the proper subspace that contains the signal. This is synonymous with determining the object's depth. It is further desired that this process be robust to object shape. It is shown in the following

paragraphs that the subspace from a sphere, a cylinder, and a flat plate buried at 0.0, 0.25, and 1.0m depths can be identified by projecting each signal into the shallow, mid, and deep subspaces and choosing the subspace that rejects the least amount of signal energy. This approach works even in the presence of noise.

The subspace projection method is used here to identify object depth. Equations 3.16, 3.17, and 3.18 defines a set of matrices called projection matrices [34]. When a projection matrix operates on an observed signal, it has the effect of revealing the signal components found in that subspace. This fact is often used to reduce noise is signals. In this application a mismatched subspace will have the effect of reducing the energy of the signal. The projection matrices for the subspaces are formed according to Equations 3.16, 3.17, and 3.18. Here Λ_d and W_d in Equation 3.15 represent column vectors formed by digitally sampling the basis functions.

$$H_d = [\ \Lambda_d \ \ W_d\ ] \tag{3.15}$$

$$P_{shallow} = H_1(H_1^T H_1)^{-1} H_1^T \tag{3.16}$$

$$P_{mid} = H_2(H_2^T H_2)^{-1} H_2^T \tag{3.17}$$

$$P_{deep} = H_3(H_3^T H_3)^{-1} H_3^T \tag{3.18}$$

Unfortunately, the subspaces occupied by objects at different depths are not orthogonal. They can be geometrically be interpreted as slanted planes. Some energy from signals at, say, 0.0m will be present in the subspace occupied by a signal at 1.0m. Table 3.2 shows

Table 3.2: Norm After Projection into Subspaces (No Noise)

	Spheres			Flat Plates			Cylinders		
	Shallow	Mid	Deep	Shallow	Mid	Deep	Shallow	Mid	Deep
Shallow	1.00	0.79	0.72	1.00	0.99	0.93	1.00	0.94	0.92
Mid	0.70	1.00	0.72	0.92	1.00	0.99	0.81	1.00	0.94
Deep	0.19	0.51	1.00	0.63	0.85	1.00	0.37	0.68	1.00

Table 3.3: Norm After Projection into Subspaces (Noise Standard Deviation: 0.01)

	Spheres			Flat Plates			Cylinders		
	Shallow	Mid	Deep	Shallow	Mid	Deep	Shallow	Mid	Deep
Shallow	1.00	0.79	0.72	1.00	0.99	0.93	1.00	0.94	0.92
Mid	0.70	1.00	0.72	0.92	1.00	0.99	0.81	1.00	0.94
Deep	0.19	0.51	1.00	0.63	0.85	1.00	0.37	0.68	1.00

the norm of signals after being projected into the three subspaces. The results in this table are for the case of no external noise.

Since the signal before projection is normalized, the value shown corresponds to a ratio of ”energy out divided by energy in”. The first 3 columns show the results of projecting sphere signals at each canonical depth into each subspace. Note that 100% of the energy of the shallow sphere survives the shallow projection. This implies that the signal actually occupies the shallow subspace. The highlighted entries of Table 3.2 show the result of projecting the signals into the proper subspace. In all correct cases, 100% of the energy survives.

Two additional observations can be made from Table 3.2. First, when considering the flat plate at 0.0m being projected into the 0.25m subspace (i.e. the next deeper subspace), very little energy is rejected. This is a performance limiting fact. When no noise is present, the small difference between the two subspaces is detectable. In the presence of noise, however, the flat plates become very difficult signals for determining the proper depth subspace. This means that the angle between the two subspaces is very small.

Table 3.3 shows the results after applying a small amount of additive noise. This represents a situation with good signal-to-noise ratio. With this level of noise, the result for all cases (even the flat plates) remain robust.

Table 3.4 shows the result after increasing the noise by a factor of five. The signal-to-noise ratio can still be considered reasonable for this case. However, the first mistake is

Table 3.4: Norm After Projection into Subspaces (Noise Standard Deviation: 0.05)

	Spheres			Flat Plates			Cylinders		
	Shallow	Mid	Deep	Shallow	Mid	Deep	Shallow	Mid	Deep
Shallow	0.96	0.75	0.65	0.95	0.94	0.91	0.92	0.89	0.85
Mid	0.68	0.97	0.64	0.90	0.94	0.95	0.77	0.94	0.86
Deep	0.16	0.51	0.93	0.63	0.84	0.95	0.30	0.61	0.94

Table 3.5: Norm After Projection into Subspaces (Noise Standard Deviation: 0.3)

	Spheres			Flat Plates			Cylinders		
	Shallow	Mid	Deep	Shallow	Mid	Deep	Shallow	Mid	Deep
Shallow	0.52	0.32	0.42	0.31	0.38	0.19	0.42	0.44	0.48
Mid	0.37	0.62	0.48	0.31	0.37	0.26	0.31	0.43	0.52
Deep	0.18	0.37	0.62	0.36	0.33	0.30	0.20	0.33	0.52

made here by the algorithm for the flat plate case. This limiting condition can be explained by considering the W basis function for the flat plate. Due to the thin nature of the flat plate, there is very little polarizability in the horizontal direction. The W basis function is, therefore, almost non-existent. Loss of the W basis function makes determining depth for this class of object virtually impossible when significant noise is present.

Objects other than flat plates show much better robustness to noise. Table 3.5 shows a 30dB increase in noise. The resulting projections show that the depth of flat plates and the cylinders can no longer be determined with any confidence. The spheres, however, still give correct depth estimates.

3.3.4 Shape Identification

Once object depth is determined the object polarizability can be estimated. Figure 3.19 shows the signal components for 3 canonical shapes: a sphere, a cylinder, and a flat plate. The polarizability of each shape type is known.

For the sphere the polarizability is: $P_z = 1.0$, $P_x = 1.0$. For cylinders: $P_z = 1.0$, $P_x = 0.5$. And for flat plates: $P_z = 1.0$, $P_x = 0.2$. This is summarized in Table 3.6.

These values were chosen for the simulation intuitively. The sphere should not have a bias in any direction because it is spherical. (This is a minor assumption that may not be true in reality due to the ”infinite conducting half-space”, i.e. the ground, within which the

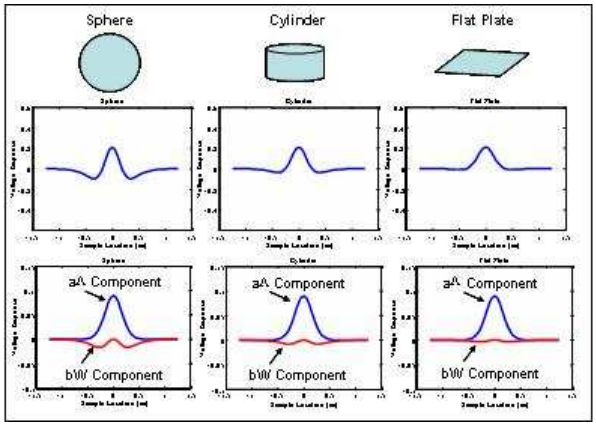

Figure 3.19: Canonical Objects at Same Depth

Table 3.6: Shape Polarizabilities

	P_z	P_x
Sphere	1.0	1.0
Cylinder	1.0	0.5
Flat Plate	1.0	0.2

object is buried.) The flat plate, on the other hand, has a large area perpendicular to the vertical magnetic field. The swirling eddy currents induced by the sensor result in a large vertical polarizability. Because the flat plate is thin, it has only a little area perpendicular to the horizontal magnetic field. The resulting polarizability is small. Similarly, in the case of the cylinder, if it is ”short”, then it will have less ”height” than it has ”diameter”. By the same line of thinking it is expected that the horizontal direction will be less polarizable than the vertical.

The minimum squared error inversion algorithm for estimating polarizability is shown in Equation 4 [35].

$$\begin{bmatrix} \hat{p}_z \\ \hat{p}_x \end{bmatrix} = \left(H_{\hat{d}}^T \; H_{\hat{d}} \right)^{-1} \; H_{\hat{d}}^T \; \underline{s} \tag{3.19}$$

In this equation d is an estimate of the object depth, and H_d is defined by Equation 3.15. The vector $\underline{s}$ represents a column vector containing the sampled spatial signal. Table

Table 3.7: Polarizability Estimates (No Noise)

		Shallow	Mid	Deep	Shallow	Mid	Deep	Shallow	Mid	Deep
Shallow	$\hat{P}_z$	1.00	0.93	0.45	1.00	0.76	0.38	1.00	0.82	0.41
	$\hat{P}_x$	1.00	0.41	-0.42	0.20	-0.27	-0.62	0.50	-0.01	-0.54
Mid	$\hat{P}_z$	0.53	1.00	0.78	0.96	1.00	0.63	0.80	1.00	0.69
	$\hat{P}_x$	0.82	1.00	0.09	0.41	0.20	-0.44	0.56	0.50	-0.24
Deep	$\hat{P}_z$	-0.10	0.30	1.00	0.67	0.89	1.00	0.38	0.67	1.00
	$\hat{P}_x$	0.13	0.59	1.00	0.33	0.43	0.20	0.26	0.49	0.50

Table 3.8: Polarizability Estimates (Noise Var: 0.01)

		Shallow	Mid	Deep	Shallow	Mid	Deep	Shallow	Mid	Deep
Shallow	$\hat{P}_z$	1.00	0.92	0.46	0.98	0.75	0.38	1.01	0.84	0.38
	$\hat{P}_x$	1.00	0.40	-0.40	0.18	-0.26	-0.61	0.52	0.00	-0.55
Mid	$\hat{P}_z$	0.53	0.99	0.79	0.96	0.98	0.62	0.80	1.02	0.67
	$\hat{P}_x$	0.82	1.00	0.10	0.40	0.18	-0.44	0.58	0.52	-0.25
Deep	$\hat{P}_z$	-0.11	0.29	0.99	0.68	0.89	1.00	0.36	0.67	0.99
	$\hat{P}_x$	0.12	0.58	1.00	0.34	0.41	0.20	0.25	0.50	0.48

3.7 illustrates the results of using proper and mismatched H_d matrices. In the case where the proper H (i.e. the proper basis set) is used, the computed polarizability is exact. For example, the sphere at any depth is shown to be properly estimated with unit polarizability in the vertical and horizontal directions. The same is true for the flat plates and the cylinders. Use of a mismatched bases, however, results in extremely misleading estimates.

In the case of additive noise contaminating the signal, a similar result is observed. Table 3.8 contains a small amount of additive noise. All canonical objects, however, are estimated with little error. Increasing the noise in the observations, increases the error in the final estimates.

Table 3.9 shows the effect of higher noise. Looking at the subspace identification results of Section 3.3.3, it is clear that the depth estimation algorithm will fail before the polarizability estimator of Section 3.3.4. If the depth is determined using another sensor, the polarizability estimator will be able to classify objects by their shape even in the presence of significant noise.

3.3.5 Subspace Method Conclusions

Two basis functions have been presented that form a basis for metal detector signals. These functions are the Λ and W basis functions. It has been shown that objects from the

Table 3.9: Polarizability Estimates (Noise Var: 0.05)

		Shallow	Mid	Deep	Shallow	Mid	Deep	Shallow	Mid	Deep
Shallow	$\hat{P}_z$	1.06	0.95	0.42	0.97	0.71	0.38	0.99	0.84	0.40
	$\hat{P}_x$	1.12	0.37	-0.40	0.23	-0.33	-0.66	0.49	0.02	-0.53
Mid	$\hat{P}_z$	0.52	1.05	0.75	0.89	0.96	0.61	0.84	1.00	0.67
	$\hat{P}_x$	0.87	1.00	0.09	0.37	0.12	-0.53	0.64	0.53	-0.23
Deep	$\hat{P}_z$	-0.17	0.33	0.97	0.63	0.89	1.07	0.36	0.65	0.96
	$\hat{P}_x$	0.08	0.58	1.00	0.28	0.36	0.22	0.31	0.50	0.47

same depth have the same basis functions regardless of shape and metal content. Object size and metal content affect the weightings of the two basis functions. Object depth, on the other hand, affects the width of the functions.

A subspace projection method was introduced that identified the proper basis of a measured signal from an object at unknown depth. The method was shown to work perfectly in a low noise environment. When noise is added, however, the similarity between subspaces made depth determination difficult. This was especially true of the flat plate object.

Once object depth was determined (or if it was provided from another sensor), the object shape was determined by estimating the polarizability of the of the object in the vertical and horizontal directions. Objects that are significantly different, like the sphere, cylinder, and flat plate, are easy to identify even in the presence of significant noise. A mismatch in depth estimation, however, was shown to cause significant error in the estimated polarizability values.

This work has shown how the physics of the magnetic field produced by a metal detector can be used to identify a signal basis set. This basis is composed of two principal functions with which all metal detector signals can be represented. A careful use of the these bases can be made to reveal both the depth of the object and its basic shape. Future research will expand the analysis to scanning two spatial dimensions, as well as, considering buried object response to multiple frequencies.

CHAPTER IV

STATISTICAL APPROACHES

4.1 Multimodal Detection

Landmine detection often employs multiple sensors due to the diversity of sensor signatures encountered. Two commonly used sensors are ground penetrating radar (GPR) and electromagnetic induction (EMI) metal detectors. Both sensor technologies have been proven to be very effective in detecting metal landmines. The GPR has been shown to detect non-metal mines because radar signals are reflected by the dielectric discontinuity between the soil and the plastic mine casings. Also, in some cases the EMI has been used to detect non-metal cased mines by detecting the small amount of metal contained in the mine's firing pin. Theoretically, therefore, both sensors are capable of detecting all landmine types. In practice, however, performance of each sensor is challenged by low signal-to-noise ratios on some landmines depending on type of mine, burial depth, and environmental conditions.

In this work two environments are considered. The first is a clay background and the second is gravel. These two backgrounds offer a look at how EMI and GPR sensor statistics change based on the environment surrounding the landmine.

4.1.1 Multimodal Landmine Detection

Multi-modal sensor systems describe a single sensor that utilizes separate sensor modes or a collection of sensors that employ different physical phenomenology. By utilizing multiple modes, a greater diversity of information is obtained. In this work we look at

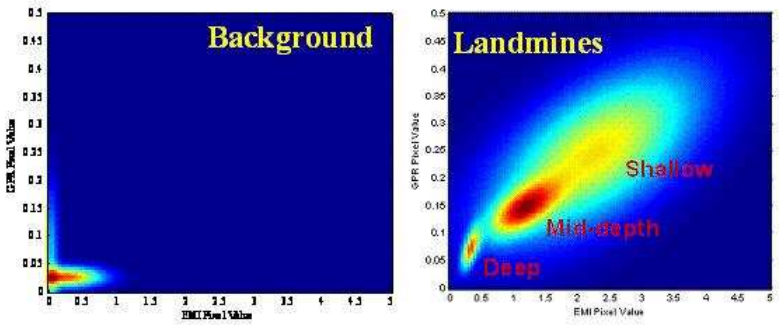

Figure 4.1: Estimated Joint Probability Density Functions

a vehicle mounted landmine detection system using an array of EMI and GPR sensors. The two sensor arrays each raster scan an image of the ground response as the vehicle moves forward. The two images are registered at the pixel-to-pixel level for detection of landmines.

Joint Probability Densities

A set of training data is used to establish a 2D joint probability density between the pixels of the EMI image and the pixels of the GPR image. Six classes of landmines are considered. The classes are arranged according to depth for both metal cased and plastic cased mines. The landmine classes are: 1) deeply buried metal cased 2) mid-depth metal cased 3) shallow depth metal cased 4) deeply buried plastic cased 5) mid-depth plastic cased and 6) shallow plastic cased. All classes are for anti-tank mines. A seventh class is designated background.

Figure 4.1 shows the estimated joint probability densities for background pixels and metal cased landmines. These PDFs were generated by extracting pixels of each class from EMI and GPR training images. The sample mean, variance, and correlation were then computed, and the PDFs generated using a bivariate Gaussian model. These PDFs will be used to generate the posterior probabilities described in Section 4.1.1.

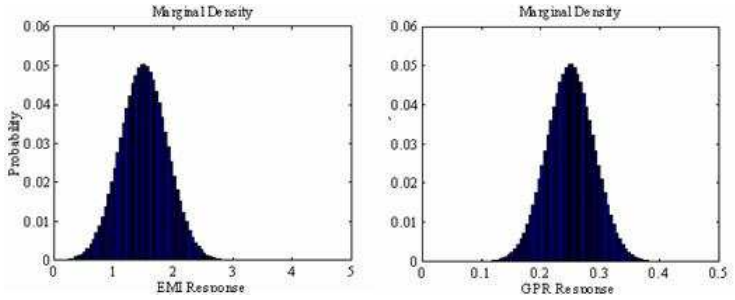

Figure 4.2: Marginalized Probability Density Functions of Mid-depth, Metal Cased Landmines

Single Mode (Marginalized) Densities

Single-mode approaches for the MAP detector exist for both the GPR and EMI sensors. The 2D PDFs are marginalized to only include the statistics of one sensor. This is done by ”integrating out” one of the sensors. The MAP approach described in Section 4.1.1 can be used in the multi-modal approach or in single mode with either sensor. Section 4.1.3 shows the performance advantage of utilizing the multi-modal approach.

Maximum A Posteriori Detection

In this application we have seven classes of objects. The sensors respond to each object class in a different way. This difference manifests itself statistically in the resulting observations as a change in the probability distributions of the observed pixels. For example, the amplitudes of the received signals for both sensors are greatly affected by the distance from the sensor to the object. This results in very different pixel probabilities between landmines buried shallow and landmines buried deep. This can be seen in Figure 4.1 where the mean and variance of the deep, mid-depth, and shallow landmines have significantly different values. The idea behind the MAP detector is to make a measurement and use that observation to determine which probability distribution is the likeliest to have produced that observed value. For this application, all classes have signatures that occupy more than 1 pixel. This fact can be used in the MAP processor by performing multiple measurements on the same object as it passes beneath the vehicle.

The Maximum A Posteriori (MAP) detection approach proposed here takes N

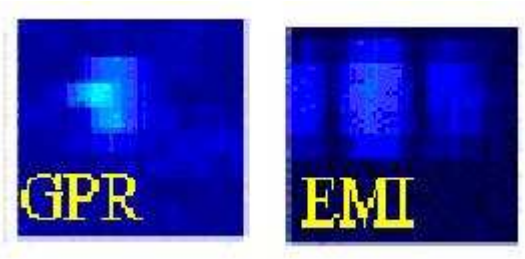

Figure 4.3: Signatures from a Mid-depth, Metal Cased Landmine

looks at an object sequentially as the object passes by the sensor. Before beginning the measurements, an a priori probability is assigned to the classes. Since there are seven classes, the a priori probability is set to $\frac{1}{7}$ for each class. After each measurement Bayes Rule is used to update the probability assignments. Equation 4.1 is called the Update Equation. For the first measurement it translates the prior probability assignment to a posterior probability. Likewise, for all subsequent observations it continues to update the probabilities as new measurements are made. $P(y|x)$ in Equation 4.1 is the observation model for a given class x. The probability $p_n(x)$ is the probability that an observed object is class x for the n^{th} observation, y_n.

$$p_n(x) = \frac{p(y_n|x)p_{n-1}(x)}{\sum p(x, y_n)} \tag{4.1}$$

4.1.2 Adapting to the Environment

The probability distributions shown in Figures 4.1 and 4.2 are for landmines in a clay background environment. If this environment were changed, it would be reflected in a new set of distributions. Figure 4.4 illustrates the tremendous variability that can be seen between observations made in a clay background and observations in a gravel background. The gravel lane shows a significantly higher amount of attenuation than the clay lane. This is likely due to the amount of moisture that is held within the material. Clearly there is a need for the sensor to adapt to this change in class statistics.

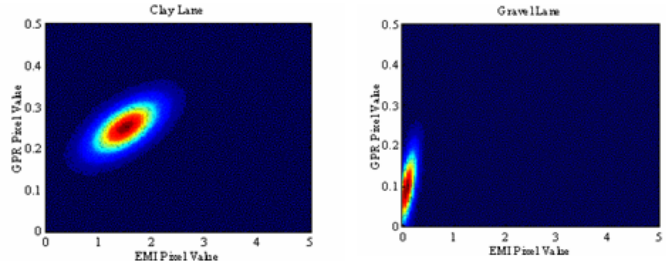

Figure 4.4: PDFs of EMI and GPR pixels from mid-depth buried metal landmines. (left) Lane material is clay. (right) Lane material is gravel.

One way to assist in adapting the sensor statistics is the use of electromagnetic models coupled with measurements of the environmental parameters. A GPR measurement of the ground dielectric permittivity can be made by looking at the ground bounce return. Mapping the reflection coefficient into dielectric permittivity for a homogeneous ground follows Equation 4.3 [36].

$$R_{12} = \frac{1 - \frac{1}{\sqrt{\epsilon_r}}}{1 + \frac{1}{\sqrt{\epsilon_r}}} \tag{4.2}$$

Figure 4.5 shows the inverse mapping. Wet ground represents a relative permittivity in the range of 40 to 60. Dry ground represents a relative permittivity from 3 to 10. It can be shown that an estimate for dry ground is somewhat robust to noise in the observation. In other words, a few observations of the ground bounce return can be averaged to very effectively estimate the permittivity value. Once this value has been obtained, the statistics of the seven classes can be estimated based on a simple electromagnetic scattering model. When the ground is wet, however, the estimation process is more complicated. A small amount of noise in the reflection coefficient could double the estimated permittivity value. This means that many observations will need to be averaged to produce a robust estimate. However, once a robust estimate is obtained, simple scattering models can be use to generate the class probabilities.

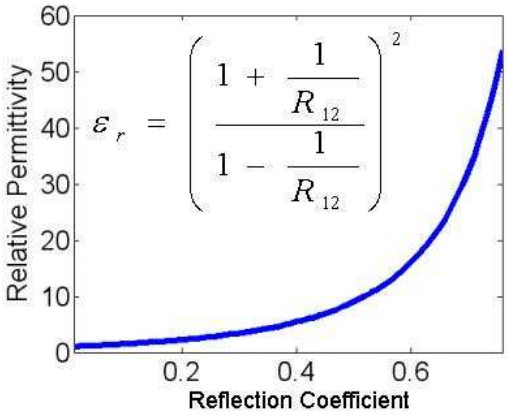

Figure 4.5: Inverse Mapping from Reflection Coefficient to Dielectric Permittivity

4.1.3 Detection Performance

In this section the results of applying the sequential MAP detector to multi-modal and single mode landmine data are shown. For each case 5 observations are made on each object as it passes the sensor arrays. The results show that multi-modal processing outperforms single mode.

Here it is also shown that adapting to the environment is an important part of optimal performance. The multimodal MAP detector is re-trained for application to a wider set of environmental conditions. In this case the conditions include a clay soil background and a gravel background. Training for both environments simultaneously means widening the class statistics to handle measurements that are more variable. The consequences of this generalization are a significant reduction in detector performance.

Multimodal Versus Single Mode

Here the MAP detector described above is applied in both multi-modal and single sensor modes. In single sensor mode the EMI and GPR sensors apply the trained 1D PDF 5 times as the objects are encountered. The EMI initially has the better performance because it is very good at detecting metal cased landmines. Eventually, however, the GPR reaches the maximum detectible number of objects before the EMI because it is able to better handle

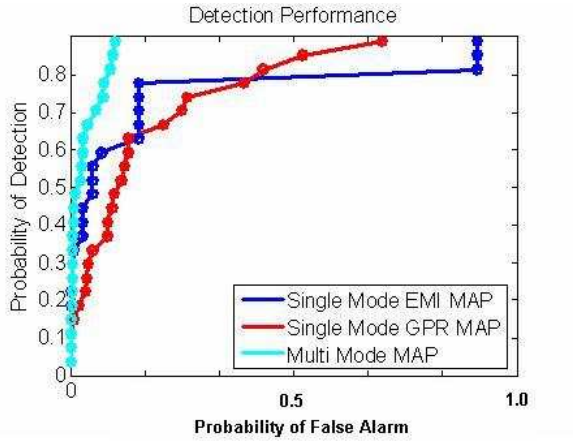

Figure 4.6: Multi-modal Versus Single Mode MAP Detection Algorithms - Multi-modal processing has a clear advantage.

the plastic cased mines.

The multi-modal detector has the advantage of utilizing the EMI's ability to detect metal and the GPR's ability to detect plastic. Also, it has another significant advantage. The background clutter shown in the Left Frame of Figure 4.1 appears to have a bifurcated nature. That is there appear to be some clutter objects in the background that a observed by the EMI and not the GPR while others are observed by the GPR and not the EMI. The EMI may be seeing metal or metal residue from very small metallic clutter objects. These objects have too small of a radar cross section to appear in the GPR data. The GPR, on the other hand, is observing rocks or other dielectric discontinuities that are not observable by the EMI. This nature of the background noise allows for a powerful discrimination in the 2D PDFs. This is due to the correlation that exists between the EMI and GPR sensors when observing landmine signatures.

Performance With and Without Adapting

The importance of adapting to environmental changes cannot be stressed enough. Soil that is wet will produce very different sensor statistics than soil that is dry. In this section we illustrate the need for adaptation when the soil environment changes. The two lanes consist of the clay and gravel lanes described in Section 4.1.2. In Section 4.1.2 it was observed

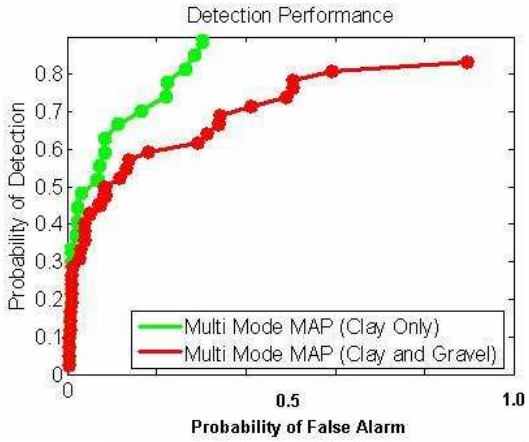

Figure 4.7: Multi-modal MAP Detector Trained and Applied to Clay Background Compared to a Generalized Detector Trained and Applied to Clay and Gravel Backgrounds

that the mid-depth landmine statistics show much greater attenuation in the gravel lane than in the clay. This could be an indication of moisture being present in the gravel lane. Moisture causes the dielectric permittivity and the conductivity of the soil to increase as much as an order of magnitude. Since attenuation of electromagnetic energy is directly determined by the permittivity and conductivity of the soil, the statistics of the signatures found in the collected imagery change.

For the combined training of the MAP detector, a set of lanes was sequestered from both the clay and gravel backgrounds. The 2D PDFs were determined and applied to the remaining lanes of both backgrounds. The result is a detector that is generalized to handle both backgrounds. Unfortunately, the performance of the detector is reduced significantly.

4.1.4 Multimodal Summary

In this work a maximum a posteriori (MAP) detection algorithm is developed that utilizes sensor statistics to classify metal and plastic cased landmines. The MAP sensor can be applied multi-modally using a 2D PDF trained from signatures produced by an electromagnetic induction (EMI) metal detector and a ground penetrating radar (GPR). It can also be applied to either sensor in a single sensor mode. Application to experimental data shows that the multi-modal approach significantly outperforms either sensor run in

single sensor mode. The data was obtained from a clay background mine lane.

A second experiment shows that the statistics of the sensor can change significantly between the clay background lane and a gravel background lane. The second experiment trains the MAP detector for both environments. This makes the detector more general but the end results is a for less powerful detection performance. Adapting the trained statistics when background changes occur is an essential part of optimized system performance.

Future work in the area of adaptive algorithms will include the employment of physical models for assisting the prediction of sensor statistics. Also, the MAP detector will be expanded to take advantage of the spatial signatures observed from the landmines in two and three dimensions. This work considered only landmine classes. In a real world environment, clutter classes from metal and/or non-metal objects lying on the surface will also be taken into account. An approach for scheduling additional sensor measurements to discriminate target and clutter types is proposed in [37]. And, finally, future work will include non-myopic approach that will account for the time required to make certain sensor measurements. This approach will choose sensors appropriately to minimize the amount of time required to traverse a specified distance. [38] [39] [40] [41]

4.2 Bayes Networks

A Bayesian Network is a way of thinking about joint probabilities. It allows for an associated PDF to be broken down into a system of conditional dependencies [42]. Using Bayes rule a joint PDF can be rewritten as a product of conditional probabilities. The attraction of this is that the conditional probabilities may be easier to train than the full joint PDF.

In [42] a burglar alarm problem is considered. The event of the alarm going off is a binary random variable, Z. The alarm can be set off by a burglar or by an earthquake (the problem takes place in southern California). Two neighbors have been asked to call the owner at work when the alarm goes off. Probabilities of calling are given for each

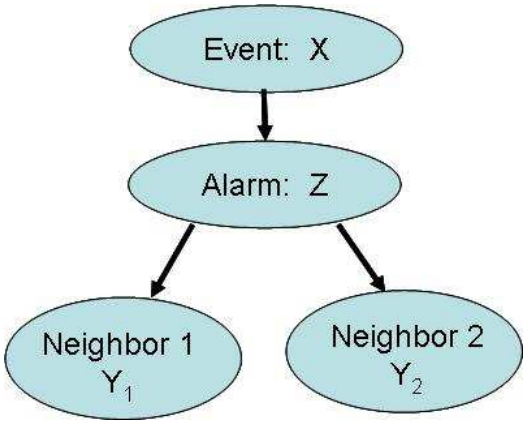

Figure 4.8: A Bayesian Network Structure for the Burglar Alarm Problem

neighbor. The events of the neighbors calling are, Y_1, Y_2. The root event, X, is a random variable taking on the value 0 for an earthquake, 1 for a break in, and 2 for no alarm (the neighbors are calling for some other reason). The joint probability of all these events can be modelled as:

$$P(Y_1, Y_2, Z, X) = P(Y_1|Z)P(Y_2|Z)P(Z|X)P(X) \tag{4.3}$$

The conditional probabilities and their relationship can be graphically displayed in an $acyclic\ directed\ graph$. For the burglar alarm problem, this looks like Figure 4.8. The variable X here is called the parent of Z. Z, meanwhile, is the parent of Y_1 and Y_2. The layer of the network inhabited by Y_1 and Y_2 is called the observation layer. Z, on the other hand, is in the $hidden\ node$ layer. The term hidden nodes implies that we (here the owner) does not directly observe the alarm going off. The goal is to use probabilistic reasoning to decide whether the alarm is due to a burlary or due to an earthquake. This decision is to be made based on the observations.

We wish to apply this technique to the landmine detection/classification problem. In this case, the event is the existence of a landmine. The alarm event could be an anti-personnel, anti-tank, a false alarm, or any number of a collection of non-mine objects.

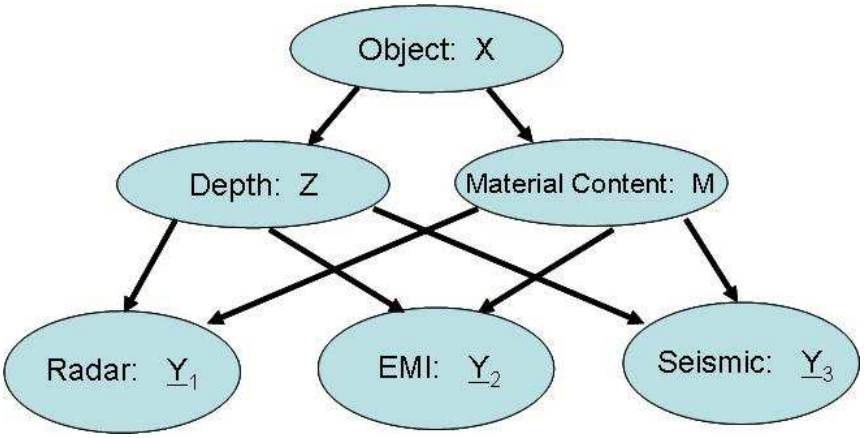

Figure 4.9: A Bayesian Network Structure for the Landmine Problem

The hidden nodes could be associated with soil types, object depths, and object metal content. (Plastic mines have low metal content while metal cased mines have high.) A possible network structure for this problem is shown in Figure 4.9.

CHAPTER V

SENSOR SCHEDULING

5.1 Single Confirmation Sensor - Active Sensing

Active Sensing is a popular form of sensor scheduling that utilizes a measure of increased certainty called information gain to dynamically choose a sensor to apply to a given decision problem [43]. In this section a basic application of the concepts of Active Sensing are applied in the area of landmine detection. Active sensing is a way of scheduling multiple sensors, which have diverse capabilities and uses. Each sensor is considered a resource and a statistical model of how objects of interest react to each sensor is known. As a sensor system begins interrogating an area for objects it decides dynamically which sensor to use to provide the maximum amount of information.

The architecture proposed in this work uses traditional vehicle mounted scanning sensors (EMI and GPR arrays) to assign prior probabilities to all locations in the mine lane. This information is given to the ”Sensor Management Decision Engine”, which applies Active Sensing to decide the most powerful confirmation sensor to deploy. In the myopic case, a sensor is always deployed to interrogate every 1ft by 1ft square of the mine lane. The time sensitive case, however, sometimes chooses not to deploy a sensor.

Myopic sensor management algorithms consider only the immediate situation when determining what action to schedule [44]. (Webster’s Dictionary defines myopic as, ”Lacking long-range perspective in thinking or planning.”) Non-myopic approaches consider other information concerning the situation or the environment that can impact

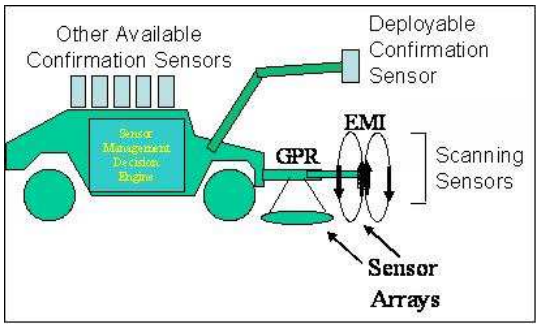

Figure 5.1: Proposed Architecture for Applying Sensor Management to a Vehicle Mounted Landmine Detection System

the performance of the system [45]. All sensors do not perform their measurements in the same amount of time. By taking time into account, the platform can traverse the given territory in the minimum amount of elapsed time. In the example situation presented here, the myopic only approach traversed the mine lane in 270 minutes. By accounting for processing time the approach traversed the lane in 25 minutes. Some degradation in classification performance was incurred in the faster case.

Information gain is a quantity that describes the amount a sensor reduces the uncertainty in information about an object. In a tracking application this implies knowing the object's location and velocity with greater accuracy. In the landmine area this implies better knowledge of an object's depth and/or type. In landmine detection some sensors are capable of providing information about some objects and not others. For example, a metal detector can be used to provide information about metal content for metal cased mines. This information can be used to eliminate false-alarms caused by metallic clutter on the surface. It is less useful, however, to use the metal detector when interrogating a low-metal object. In the case of the plastic cased landmine a metal detector may pick up a small amount of metal in the firing-pin. However, this measurement is sometimes not available due to small signal-to-noise ratio. The sensor system would likely do better in this situation by deploying a chemical detector (olfactory sensor) that could detect the presence

of TNT. Or it might be more useful to utilize the ground penetrating radar to determine if the object is laying on the surface or buried. If the object is on the surface it may be most useful to aim a visible light camera to investigate the object. The goal, therefore, is to schedule sensors appropriately based on observations made by the sensor platform. Active Sensing is a method of realizing effective sensor scheduling by predicting the information gain potential of available system resources. In this work a Sensor Management Decision Engine has been implemented in software that decides what confirmation sensor to deploy (if at all) based on information provided by the scanning sensors.

5.1.1 Sensor Management using Active Sensing

Over the years many sensor technologies have been proposed and developed for detecting landmines. A few of these include: ground penetrating radar, electromagnetic induction metal detectors, magnetic quadrupole resonance, infra-red radiometers, visible light cameras, passive magnetometers, olfactory sensors, and many more. Some sensors have been useful as long-range scanning devices. These are technologies that can be used at a large standoff distance. Examples of standoff sensors are: synthetic aperture radar, infra-red radiometers, and passive millimeter wave radiometers. Other sensors can be used for scanning, but are only effective at close distances. Examples of these close-in sensors are: passive magnetometers and electromagnetic induction metal detectors. Other technologies have been shown to be useful for scanning only small regions. These latter sensors have become known as confirmation sensors.

The focus here is on the use of active sensing on a vehicle based detection system. The starting point is an assumption that all classes of objects are equally likely. By employing a scanning sensor an initial observation is made. Bayes rule is then used to update the uniform priors. Equation 4.1 is known as the update equation.

Where $p_{n-1}(x)$ represents the class probabilities for the state vector x for the previous observation. The statistical model $p(y|x)$ is the knowledge of how the sensor measurement,

y, will respond statistically to the object state, x. The summation in the denominator is a normalizing constant.

Once the scanning observation has been made, the sensor manager must decide what confirmation sensor to deploy (or to not deploy one at all). Here the Rényi divergence is used to predict the expected information gain for the available sensors [46].

$$D(\hat{p}_n||\hat{p}_{n-1}) = \frac{1}{1-\alpha} \ln \left(\int \hat{p}_n^{\alpha}(x) \hat{p}_{n-1}^{1-\alpha}(x) dx \right) \tag{5.1}$$

The probabilities P_n are the expected probability distribution of the classes after the next observation. P_{n-1} is the probability distribution of the classes after the previous observation. The divergence computation responds to the probabilities with a larger divergence value if the variance in the second probability distribution has a lower variance than the first. This means that if P_n is describing the class with more certainty, then the sensor is more likely to be chosen and deployed. The sensor out of all the resources that provides the greatest divergence (i.e. the greatest information gain) is deployed. Note that the α parameter is a shape parameter that can be adjusted to optimize performance.

The classes that will be considered in this paper are: 1) deeply buried, metal cased anti-tank mine, 2) mid-depth buried, metal cased anti-tank mine, 3) shallow buried, metal cased anti-tank mine, 4) deeply buried, plastic cased anti-tank mine, 5) mid-depth buried, plastic cased anti-tank mine, 6) shallow buried, plastic cased anti-tank mine, 7) aluminum clutter on surface, 8) non-metal clutter on surface, 9) iron clutter on surface. The prior distribution that will be applied to these classes is 0.1 (that is, a uniform prior.)

Active sensing can be employed at all levels of the landmine detection problem. If standoff (i.e. airborne) sensors were used to identify a minefield, the information collected by these sensors could be held on-line for assigning the prior probability distributions of given regions. This implies a co-operative network of airborne and ground based vehicles involved in the landmine detection process. Such a network could have the airborne

vehicles queuing ground based vehicles to specific locations or ground based vehicles queuing stored airborne assets for confirmation [47].

5.1.2 Scanning Sensor Simulations

For the purpose of studying a realistic vehicle based landmine detection system, a system with traditional scanning sensors and a suite of confirmation sensors is proposed. The simulated scanning sensors will be used to acquire possible landmines and the confirmation sensors will be used to show how the additional sensors are able to eliminate uncertainty using Active Sensing. In this section the scanning sensor simulations are introduced. These sensors are an array of electromagnetic induction metal detectors and an array of ground penetrating radar.

Figure 5.2 shows a sample simulation of an EMI signature. This simulation was generated using a point model of a magnetic dipole source (i.e. a current loop) over a conducting half space [47]. The sample rate in the along track direction is 2" (5cm). The sample rate in the cross track direction is 16" (40cm). The cross track sample rate represents the distance between adjacent sensors mounted on the system.

The target in Figure 5.2 is an anti-tank landmine buried at 3". (That is, 3" from the earth surface to the top of the landmine.) The brightest part of the signature corresponds to the sensor passing directly over the top of the mine. The dark regions surrounding the center are negative voltage readings. This sign reversal is caused by the incident magnetic field of the metal detector coil. As the coil passes over the mine, the dipole nature of the magnetic field reverses in direction. Some real world sensors handle this phenomenon in different ways. Typically, an absolute value is taken by the receiver. In this simulation we have chosen to take the real part, which retains the sign reversal. The operating frequency of this simulation was 75Hz.

The GPR produces a similar scanning signal. Figure 5.3 shows a 2D representation of the GPR signature. This simulation was produced by simulating a stepped frequency radar

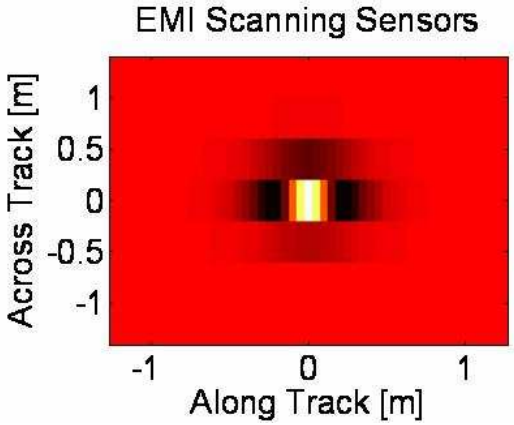

Figure 5.2: Simulated Signature of an EMI Scanning Sensor Array

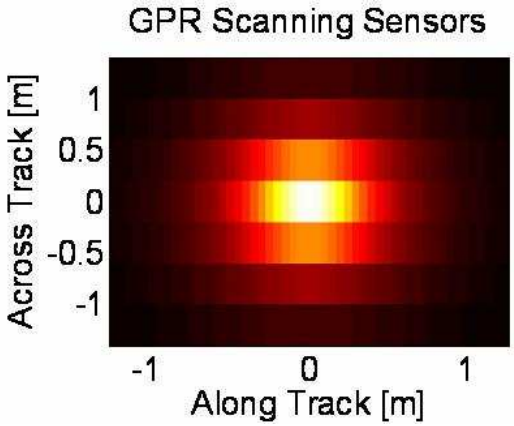

Figure 5.3: Simulated Signature of a GPR Scanning Sensor Array

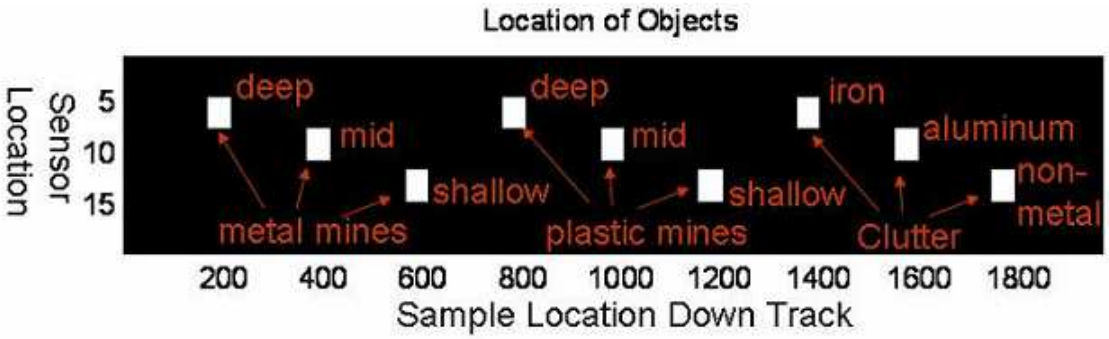

Figure 5.4: A Virtual Test Lane - Locations of simulated landmines and clutter objects

system [45]. The starting frequency is 500MHz and the ending is 2GHz. 128 frequency steps were generated. The target is modeled as a point source with the expected RCS of an anti-tank landmine. At each of the 128 frequencies the radar link equation was used to generate an expected return. The returns were FFT'ed to convert from frequency into depth and the vertical sum of the energy is computed. This is a traditional approach to creating an image with an array of ground penetrating radar sensors. The sampling rate of the simulation in along track and cross track directions is the same as that of the EMI (5cm x 40cm). Both arrays are assumed to be mounted 1 foot above the surface. In the end, pixel level registered images are generated for the two sensors.

The two sensor technologies described above are often used on vehicle mounted mine detection systems. They have been proven effective over the years for detecting both metal and non-metal cased mines. Using the models described above, a virtual test lane was simulated. Figure 5.4 shows the locations and types of landmines and clutter objects.

5.1.3 Confirmation Sensor Models

In addition to the scanning mode described in Section 5.1.2, EMI and GPR sensor technologies have multiple other ways to be utilized. The EMI, for example, can be pulsed and the decay rate of eddy currents induced in the object can be measured. These decay

Table 5.1: Averages

	1	2	3	4	5	6	7	8	9	10
1	0.01	4.5	5.5	6.5	1.5	1.6	1.7	4.5	9.0	1.5
2	0	8	8	8	2	2	2	6	6	0.5
3	0.25	0.25	0.25	0.25	0.25	0.25	0.25	0.25	0.25	0.25
4	0	9	9	9	4.5	4.5	4.5	1.5	1.5	0.75
5	0.75	9	6	3	9	6	3	3	3	3
6	0	9	9	9	9	9	9	3	3	4.5

Table 5.2: Variances

	1	2	3	4	5	6	7	8	9	10
1	2	0.5	0.5	0.5	2	2	2	0.5	0.5	2
2	3	1	1	1	2	2	2	1	1	3
3	0.25	0.25	0.25	0.25	0.25	0.25	0.25	0.25	0.25	0.25
4	1.25	1.25	1.25	1.25	2.25	2.25	2.25	3.25	3.25	4.25
5	0.75	2.25	1.25	0.75	2.25	1.25	0.75	0.75	0.75	0.75
6	1.25	3.25	2.25	1.25	3.25	2.25	1.25	1.25	1.25	1.25

rates reflect the metal content of the object. With additional processing, the induced dipole moments of the buried object can be estimated [48] [49]. The induced moments in the x, y, and z-directions are a measure of the object's size and orientation. The amplitudes of these induced moments are another measure of the object's metal content. The size and depth of the object can be estimated by forming an image with the GPR data. Many other sensors have been developed and are currently under development.

In this work we consider six confirmation sensors. Each sensor is a deployable resource on-board the mine detection platform. When deployed, each sensor takes a

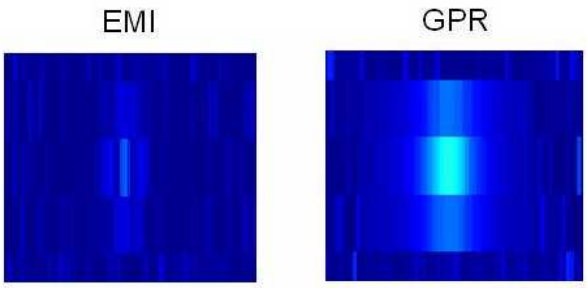

Figure 5.5: Simulated Signatures of the Iron Clutter Object

measurement, which is modeled as a random number with mean and variance that depends on the object type being measured. Table 5.1 and 5.2 summarizes the mean and variance of the measurement for each sensor and each object type. The statistics were designed with a particular confirmation sensor in mind, but are basically generic. These statistics simply represent 6 possible sensors available to the Sensor Management Decision Engine. Note that Sensor 3 models a sensor that provides no useful information. It can be viewed as a broken sensor, or, as seen later, it can be viewed as a non-operation (NO OP).

5.1.4 Clutter Rejection Example - Myopic

One of the challenges faced by close-in landmine detection systems is surface clutter. A piece of metal clutter laying on the surface could look statistically like a buried anti-tank landmine. A primary goal of the sensor management system is to properly identify an object as landmine or clutter. Here we will look at an example of iron debris, and show how the Sensor Management Decision Engine corrects for an initial misclassification of this object. We also show a confusion matrix for all objects.

Figure 5.5 shows a simulated signature observed by the EMI and GPR scanning sensors. When the system first encounters this object, the scanning sensors assign a 60% probability that the object is a deeply buried, metallic cased landmine. In truth, this object is iron debris laying on the surface. The scanning sensors assign a 40% probability to the iron clutter class.

Active Sensing is shown to be effective at determining that the object is in fact

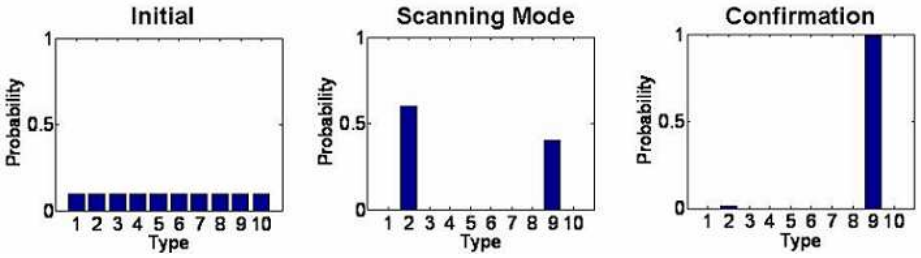

Figure 5.6: Type Probabilities: a) Prior Distribution b) After Scanning Sensors c) After Confirmation Sensor. The correct type for this case is Type 9 (Iron Clutter).

iron clutter rather than a deeply buried, anti-tank mine. Figure 5.6 shows the process of assigning probabilities to the object. Initially, no information exists concerning the object so the probabilities are all set to 10%. This is a uniform distribution. The 10% value reflects the assumption that there are 10 object classes that can be detected. The scanning sensors are fused using an adaptive, multimodal detection algorithm discussed in Section 4.1. At each step along track, Equation 4.1 is applied for the scanned EMI/GPR pair. The divergence described by Equation 5.1 is then computed for all six confirmation sensors. The divergence output will be highest for the sensor that reduces the entropy of the measurements the most. This sensor is chosen and deployed. After making the measurement, the platform moves on to the next pixel.

Figure 5.6 shows the class probabilities of a pixel over the iron debris. After the scanning measurement 60% mine and 40% iron clutter probabilities are reported. After deploying a dynamically determined confirmation sensor, the ambiguity is resolved and the correct class is assigned.

The exact confirmation sensor used to resolve the object class is not completely intuitive. Figure 5.7 shows a map of the sensors deployed for each 1ft x 1ft square in the region surrounding the iron debris. Sensor 6 is used directly above the object. In the region surrounding the object Sensor 5 was used. For the myopic case proposed here, a single confirmation sensor is deployed for every 1ft x 1ft square. In all the background locations surrounding the object Sensor 2 was chosen. There is clearly a switch in sensor choice

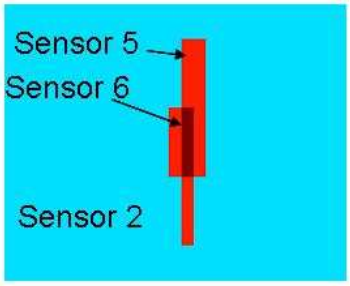

Figure 5.7: Myopic Sensor Actions Taken for Iron Clutter Object

Table 5.3: Confusion Matrix for Scanning Sensors

	2	3	4	5	6	7	8	9	10
2	0.9	0	0	0	0	0	0.1	0	0
3	0	0.7	0.1	0	0	0	0	0.2	0
4	0	0.1	0.8	0	0	0	0.1	0	0
5	0	0	0	0.8	0.2	0	0	0	0
6	0	0	0	0.4	0.5	0	0	0	0.1
7	0	0	0	0.1	0.4	0.5	0	0	0
8	0.1	0.2	0	0	0	0	0.7	0	0
9	0.4	0	0	0	0	0	0	0.6	0
10	0	0	0	0	0.3	0.1	0	0	0.6

when an object is encountered. This is due to the scanning sensors detecting the object and reported a different prior. Note that Sensor 3, which is a sensor that contains no useful discriminating information is never chosen. In this case Sensor 3 could be interpreted as a broken sensor. It is encouraging that this sensor is never chosen by the decision engine. Sensor 3 cannot give useful information so it never provides the maximum information gain.

Consider now the performance of the scanning/confirmation system under the management of the Active Sensing decision engine. Table 5.3 is a confusion matrix for the scanning sensors. This table shows the ability of the scanning sensors to correctly classify

the objects encountered in the virtual mine lane. Object Types 2,3,4 are all metal cased landmines. They types are designated based on the object's depth. Type 2 is deep (i.e. 6" to top), Type 3 mid-depth (3" to top), and Type 4 shallow (flush with surface).

The scanning sensors correctly identify Type 2 objects 90% of the time. Type 3 objects are correct 70%, and Type 4 80%. Note that Type 4 objects are classified as Type 3 20% of the time. This error is not catastrophic. The landmine is identified as a landmine, but at the wrong depth. Unfortunately, this is not always the case. Type 2 and Type 3 objects are sometimes classified as Type 8 and 9. This is a miss, since Type 8 and 9 are metallic clutter objects. (Type 8 is aluminum surface clutter. Type 9 is iron surface clutter.) These misses justify the need for an expensive (in time) confirmation sensor.

A similar analysis as the previous paragraph can be given for the non-metal cased mines - Types 5,6,7. The scanning sensor struggles to perform perfectly here due to fact that the EMI scanning sensor actually provides little or no information [50]. The GPR is doing all the work itself. A 10% misclassification rate is shown for Type 6 - mid-depth low-metal mines.

Types 8,9,10 are all clutter types. Note that several times the system misclassifies the surface clutter. However, these misclassifications are not catastrophic. It simply represents a false-alarm. The scanning sensors are correct 60% or 70% of the time.

The goal of the confirmation sensors is to reduce the non-catastrophic false-alarms and remove (hopefully) the catastrophic misses. Table 5.4 illustrates this for the simulated confirmation sensors described in Tables 5.1 and 5.2. After deploying the dynamically determined virtual sensor and reclassifying, an improved performance is observed.

Note that each class shows increase correct classification. Also, all misses have been removed, and the number of false-alarms reduced. It is important to note that this good

Table 5.4: Confusion Matrix after Confirmation Sensors

	2	3	4	5	6	7	8	9	10
2	1	0	0	0	0	0	0	0	0
3	0	1	0	0	0	0	0	0	0
4	0	0	1	0	0	0	0	0	0
5	0	0	0	0.7	0.3	0	0	0	0
6	0	0	0	0.2	0.8	0	0	0	0
7	0	0	0	0	0.2	0.8	0	0	0
8	0	0.1	0	0	0	0	0.9	0	0
9	0.1	0	0	0	0	0	0	0.9	0
10	0	0	0	0	0	0.2	0	0	0.8

performance is in part due to good confirmation sensors. The decision engine makes good choices of confirmation sensors based on the increased information provided by the sensors. If the confirmation sensor statistics are not favorable (i.e. the sensors aren't very good), then this will be reflected in the system's performance. The decision engine based on Active Sensing provides the best performance with the sensor resources it is provided.

5.1.5 Accounting for Processing Time

Now we consider an extension to the information gain approach. Active Sensing insures that sensors will be chosen to maximize information gain. However, it is also important that the decision engine monitor time. The amount of time that the system is allowed to run may be limited based on economic reasons or based on battlefield conditions. If the platform is in a potentially dangerous environment on a battlefield, then significantly less time can be given to the interrogating of a given area.

Times have been assigned to each sensor. Table 5.6 summarizes these times. With the exception of Sensor 3, these times have been chosen arbitrarily. Sensor 3 was assigned the smallest processing time. In this case, Sensor 3 can be interpreted as a non-operation. That is, the choice of Sensor 3 is equivalent to the sensor not deploying a confirmation sensor. It just moves on.

Figure 5.8 shows a modified decision statistic. The statistic allows for a balance

Table 5.5: Processing Times Associated with Each Sensor

Sensor	Time (secs)
1	1
2	10
3	0.5
4	1
5	20
6	5

$$(1-\alpha)D(f_1 \| f_0)+\frac{\alpha}{T_a}$$

Figure 5.8: Modified Decision Statistic Based on Balancing Information Gain and Required Processing Time

between information gain and required processing time. The Rényi divergence is specified by $D(f_1||f_0)$ and the required processing time (Table 5.5) is represented by T_a. The statistic used here is a first generation approach. It simply balances the two factors using an optimizable parameter, denoted by α.

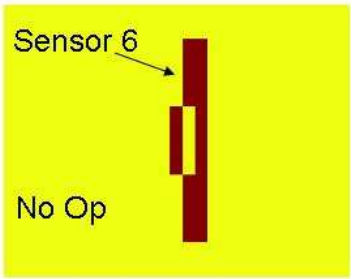

Figure 5.9: Sensor Actions Taken for Iron Clutter Object with Time Monitoring

Table 5.6: Confusion Matrix after Confirmation Sensors with Time Constraint

	2	3	4	5	6	7	8	9	10
2	0.9	0	0	0	0	0	0.1	0	0
3	0	0.9	0	0	0	0	0	0.1	0
4	0	0	1	0	0	0	0	0	0
5	0	0	0	0.8	0.2	0	0	0	0
6	0	0	0	0.2	0.6	0	0	0	0.2
7	0	0	0	0	0.4	0.4	0	0	0.2
8	0.2	0.1	0	0	0	0	0.8	0	0
9	0.2	0	0	0	0	0	0	0.8	0
10	0	0	0	0.1	0.4	0.1	0	0	0.4

The performance of the time sensitive approach is summarized in the confusion matrix of Table 5.6. Note that some degradation in performance is observed. More false-alarms are reported as well as catastrophic misses. (Future work will investigate further into extensions to the information gain approach including non-myopic approaches.) Despite its slightly degraded performance, it is still better than using the scanning sensors only. Also, using the assigned times of Table 5.5, the information gain only processing case required 270 minutes (11 hours) to complete the entire virtual mine lane. The time sensitive extension case, however, required only 25 minutes.

The tremendous decrease in lane traversal time is due to the decision engine's ability to choose not to deploy a sensor. This can be seen in the iron clutter example previously introduced. Figure 5.9 shows the action map for the time sensitive case.

When the system is observing background clutter, the system chooses to take no action. That is, it does not deploy a confirmation sensor. In this simulation this choice is equivalent to choosing Sensor 3, which provides no information about objects, but requires the least amount of time. Sensor 3 is, therefore, a No Op. When the system encounters an object, as illustrated by the iron clutter, the decision engine switches to choosing Sensor 6.

5.1.6 Single Confirmation Sensor Summary

This work is an initial example of incorporating sensor scheduling into a vehicle based landmine detection system. Simulations of two scanning sensors are used to generate a virtual mine lane containing ten object classes. Three of these classes are metal cased mines (at varying depths), three are plastic cased mines (at varying depths), and four are types of surface clutter and background noise. The scanning sensors used are electromagnetic induction (EMI) metal detectors and ground penetrating radar (GPR). Six unspecified confirmation sensors are proposed. Each sensor responds differently to the ten object classes. An example is shown where the sensor platform encounters the iron surface debris object. It initially labels the object as a deeply buried, metal cased mine. However, it reports a 40% chance that the object is iron debris. After deploying a confirmation sensor, the label assigned to the object is changed to the correct class.

Two approaches were taken in implementing decision criteria for choosing confirmation sensors. The first approach considered information gain only and showed tremendous improvement in the system's classification performance. The second approach considered a simple extension that included processing time. This time sensitive approach shows how the system can decrease its required lane traversal time from 270 minutes to 25 minutes with some degradation in classification performance [16] [51] [52].

5.2 Multiple Confirmation Sensors - Reinforcement Learning

Sensor scheduling is a research area that deals with the optimal deployment of sensing assets to accomplish a particular purpose. This could come in the form of a vehicle mounted system that utilizes scanning and confirmation sensors. In this case a single platform traverses a potential minefield. If a location is determined to have a reasonable probability of containing a landmine, the system can deploy its confirmation sensors. The sensor scheduling problem here is to choose the sensor that is going to provide the

most powerful information regarding the object that has been encountered. It may also be necessary for the system to deploy more than one sensor. Thus, part of the sensor scheduling problem is to determine when to declare the object mine/non-mine and move on to the next object. Because landmines come in various configurations, depths, and types, the sensor scheduler may choose from a variety of sensor assets according to a predetermined decision metric. The ultimate goal is to assign the correct label to the object while minimizes the number of sensors that must be deployed to make measurements at that location.

Without loss of generality, the concept of operation described above can be applied to multiple autonomous sensors. A scanning sensor, airborne perhaps, can point to potential landmine locations while a ground station based sensor scheduler determines the appropriate sensor to vector towards that location. In this work, regardless of whether the sensors are on one single platform or several autonomous platforms, it is assumed that the sensors are centrally controlled by a central location, which is the sensor scheduling software engine [37]. Some other approaches being researched include the swarm of sensors architecture [53], which assumes a number of independently operating and interacting sensors.

The approach used in this work utilizes a reinforcement learning approach to train a neural network [54]. Laboratory data acquired by Georgia Tech [55]. is used to assign a HIGH, MEDIUM, and LOW sensor response value to three sensor technologies. Responses from multiple landmine types and background are collected. From this data, a Sensor Response Table is determined. This table is used to simulate the performance of the reinforcement learning algorithm. In the end, an optimal policy for what sensor to apply given a particular sensor response is determined. This policy can then be adapted dynamically as more information comes available. The final result shows which policy to use to give the minimum number of sensor deployments (dwells) at a particular probability of correct classification.

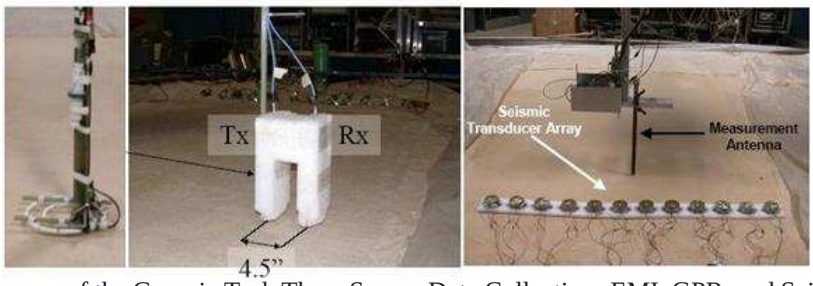

Figure 5.10: Sensors of the Georgia Tech Three Sensor Data Collection: EMI, GPR, and Seismic Vibrometer

5.2.1 Landmine Detection Technologies

It is an unchallenged doctrine that one technology will not solve the landmine problem. As technology advances, new and increasingly novel sensors are becoming available for application in the landmine detection problem. Some of these sensors are easily imaginable as scanning sensors. That is, as sensor that can be used to cover a relatively large area quickly. Other sensors, do to processing time or power requirements, are most useful as confirmation sensors. This is a sensor that is deployed to settle a question of ambiguity. The confirmation approach helps prevent the occurrence of false-alarms in the overall system. In this work, three sensors are considered. These are: 1) electromagnetic induction (EMI) sensor (a.k.a. metal detector), 2) ground penetrating radar (downward looking), and 3) seismic vibrometer. Each of these sensors were under development at the Georgia Institute of Technology under the direction of Professor Waymond Scott [55]..

Figure 5.10 shows the three sensors used in this work. From left to write the sensors are: the EMI, the GPR, and the vibrometer. The EMI sensor, or metal detector, is naturally very useful in finding buried metal objects. It is a point-to-point measurement device meaning that it is physically moved to a location where a measurement is taken. The particular EMI sensor used in this work is broadband. It measures 51 frequencies between 600 Hz and 60kHz [55].

The ground penetrating radar in this work is a downward looking version [56] [57]. The system in a frequency range from 60MHz to 8GHz. It emulates a time domain system transmitting a differentiated Gaussian pulse with a center frequency at 2.5GHz. This pulse

propagates into the ground, reflects off the objects, and an echo response is measured by the receiver in time. The radar antennas are then scanned across the region of interest making measurements at each location [55].

The seismic vibrometer generates a surface wave that propagates over the region of interest. (This is the Rayleigh wave.) The presence of a buried object can affect the height of the ground surface. The effect is observable when the object is hollow. In this version of the system, a radar is used to measure the surface displacement height. A vibrometer array is placed at the edge of the area of interest while the radar antenna is scanned across the entire region [55].

5.2.2 Landmine Types and Responses

It is well known that landmines come in both anti-tank and anti-personnel varieties. They can be composed of various materials including metal casings (typically aluminum) or non-metal casings (plastic or even wood). Anti-tank mines are sometimes found at deeper depths (6” to 10” to the landmine top) and are always large as they contain enough explosive material to damage a tank. Anti-personnel mines are shallow and small. Their aim is typically to maim rather than kill their victims.

The vast variety of mines results in a very diverse set of sensor responses. The three sensors of Section 4.1.1 respond in varying ways to the objects they encounter. Table 5.7 describes qualitatively the response of each sensor. HIGH, MEDIUM, and LOW describe whether a signal from a particular object type is strong, weak, or in between. The object types are: metal anti-tank (M-AT), metal anti-personnel (M-AP), plastic anti-tank (P-AT), plastic anti-personnel (P-AP), Hallow Metallic Clutter (CLTR-1), Hallow Non-metallic Clutter (CLTR-2), Non-hallow Non-metal Clutter (CLTR-3), and empty background (BKG). The values shown in Table 5.7 were chosen based on observations found in the Georgia Tech Three Sensor Data Collection [55]. This table will be used to simulate the training of a neural network using a reinforcement learning approach [54]. In the end, a

Table 5.7: Qualitative Description of Sensor Response to Various Landmine/Clutter Types

	1 M-AT	2 M-AP	3 P-AT	4 P-AP	5 Cltr-1	6 Cltr-2	7 Cltr-3	8 Bkg	Feature
EMI	High High	High High	High Medium	High Medium	High Medium	Low Low	Low Low	Low Low	Conductivity Size
GPR	High High	Low Medium	High High	Low Medium	Low Medium	Low Medium	Low Medium	Low Low	Depth RCS
Seismic	Medium	High	Medium	High	Medium	Medium	Low	Low	Resonance

sensor scheduling policy will be determined.

Table 5.7 shows a qualitative response of the three sensors. The response is reported as features of the measured signal. The chosen features come from typical measured values of signals gathered from the scanned images. The EMI sensor measures an analog to the conductivity of the object. In addition, objects that are deep tend to have wide signatures, while shallow objects have narrow signatures. This info is captured in the ”Size” feature of the EMI sensor. Features measured by the GPR are the depth and radar cross section (RCS) of the object. Finally, in this work, just one feature is consider for the seismic sensor. That is a resonance feature, which comes from the fact that the seismic sensor is ultimately measuring a value related to the hollowness of the object. This hollowness produces a resonant effect.

5.2.3 Sensor Scheduling Policy

A sensor scheduling policy is a rule for determine when to apply a particular sensor or series of sensors. Figure 5.11 illustrates a policy in the form of a decision tree. This illustration states that for a given location, a decision must be made concerning what sensor to deploy to make a measurement. In the example considered in this work, there are three sensors: EMI, GPR, and Seismic. Given the insight provided in the Sensor Response Table (Table 5.7), there is some optimal choice. The question is, ”What sensor provides the best information for the first measurement?” Then, ”What sensor should be applied next?”

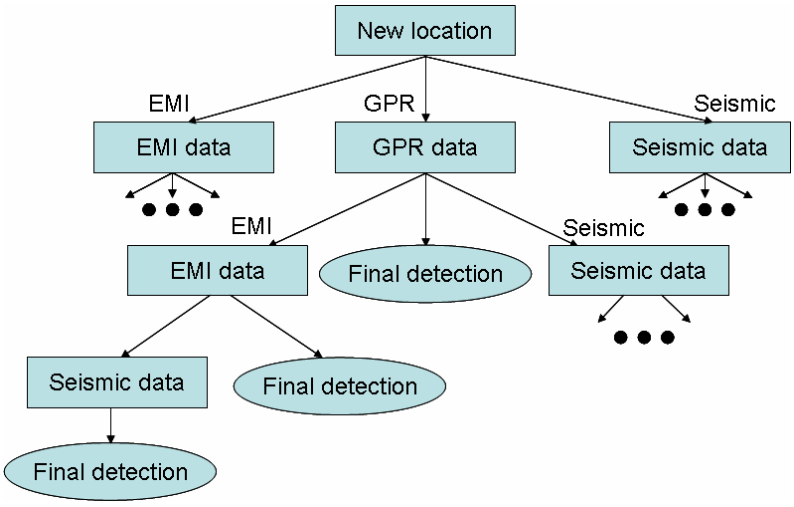

Figure 5.11: Decision Tree for Sensor Management

Table 5.8: The Optimal Policy

	M-AT	M-AP	P-AT	P-AP	Cltr-1	Cltr-2	Cltr-3	Bkg
EMI	1	1	1	1	1	1	1	1
GPR	D	D	2	2	2	D	D	D
Seismic			D	3	3			
				D	D			

Or perhaps, ”Is now the best time to decide what type of object is being encountered?” This last question is relevant when the other available sensors do not provide information that will be useful.

Figure 5.11 is the full decision tree. The optimal policy will be the subset of these possible actions that produces an optimal performance. Table 5.8 summarizes the optimal policy determined by the learning algorithm of Reference [54].

This table states the order in which each sensor should be applied or a decision (D) should be made based on the type of object that is encountered. For example, if the object is a metal AP mine, then the optimal policy suggests that the EMI sensor be deployed followed by a decision. If the object is a plastic AP mine, then the optimal

policy is to deploy the EMI, followed by the GPR, followed by the Seismic, then make a decision. Researchers applying other scheduling algorithms have also reached this same conclusion [53].

5.2.4 Multiple Confirmation Sensor Summary

Close inspection of the information contained in Table 5.8 reveals a consistent explanation of why the learning algorithm chose the specified policy. First of all, the EMI sensor was chosen to always be the first sensor deployed. This is the case because the experiment did not utilize any information that might have been available from a scanning sensor. It only took a queue from the scanning sensors that an object existed, and moved to make a measurement of that object. The EMI sensor provides the most power on average in separating the MINE/NOT-MINE classes. Looking at the table it is observed that the EMI sensor responds (high,high) for the two EMI features, if the object is a metal landmine. If the object is non-metal clutter, the EMI responds with (low,low). If all objects occur with an equal probability, as was assumed in this experiment, then using the EMI allows for easy classification of 5 out of the 8 classes (or 62.5%). Therefore, it is always chosen to go first. If the object, however, is a P-AT, P-AP, or Cltr-1 type, then the EMI does not give a conclusive result. This means that another sensor should be deployed. The optimal policy thus states to deploy the GPR. If the object is a P-AT type, then the GPR responds with a (high,high), while the other two objects (P-AP and Cltr-1) respond identically with a (low, medium). The P-AT, which gave a (high,high) reading can now be declared. Since another ambiguity exists in the measurements, the optimal policy calls for the third and final sensor to be deployed. Thus, a measurement with the Seismic sensor is made to completely resolve the ambiguity.

CHAPTER VI

SURFACE PENETRATING RADAR IMAGING

Surface pentrating problems often require an imaging step. This step removes the effect of the sensor from the data. A real world system will often blur the data. The system $point\ spread\ function$ characterizes this effect. Imaging in the radar sense is the process of removing the system's point spread function.

In this chapter we explore several aspects of radar imaging. We begin with the generic radar imaging algorithm - backgpropagation. This is cast it into the paradigm of an inverse problem by identifying a forward and adjoint operator in matrix form. Speed and memory considerations motivate the reformulation of backpropagation into a second type of radar imaging algorithm - wavenumber migration. We show how wavenumber migration can also be cast into the inverse problem paradigm. The final implementation of this algorithm makes use of both FFTs and matrix multiplications making it quite efficient. Next we explore sparse reconstruction of radar signals. This is an iterative approach that makes use of the intrinsic nature of radar signals. Radar signals are a natural "edge detector" meaning that it is the dielectric changes between materials that gives rise to the echo. Since by nature the radar echos generate edges, many pixels (or voxels) within the scene of interest are zero. Several tools can be used to enhance radar images by taking advantage of this fact. The next step involves the incorporation of "multi-path imaging" into the sparse reconstruction. This method requires the use of a method of moments tool for predicting scattered fields. And finally, adaptive imaging is expored. This final subject explores the idea of scheduling observations of a small array of sensors to produce an approximate

image that would have been produced by a large array. The scene itself is used in the scheduling process to vector the small array to the most useful observation locations.

6.1 Backpropagation Radar Imaging

Back propagation image formation takes its name from applying a propagator that reverses the propagation direction of an observed wave field. In practice the form of the back propagator is $|r - r'|e^{+jk_l|r-r'|}$. Here r is the observation location and r' is the location of the pixel (or voxel) to be imaged. For a set of observations made at M locations with L frequencies in each observation, Equation 6.1 produces the backpropagation image of the scene of interest.

$$\hat{x}_n = \sum_{l=1}^{L} \sum_{m=1}^{M} |r - r'|e^{+jk_l R(m,n)} y_{lm} \tag{6.1}$$

If the total number of independent observations (from frequency or location) is greater than the number of unknowns, an image of the scene will be successfully produced.

Before showing how back propagation can be put into the form of an inverse problem, some justification for this practice is in order. Consider the vector potential A in three dimensional E&M wave theory. Let J_z be a single vector current element. We will measure only the vertical electric field produced by this source. In general, the fields produced by any vector potential are given by:

$$\vec{H} = \vec{\nabla} \times \vec{A} \tag{6.2}$$

$$\vec{E} = -jw\vec{A} + \vec{\nabla}\vec{\nabla} \cdot \vec{A} \tag{6.3}$$

A scalar Green's function exists that propagates the vector potential from a source

point r' to an observation point r. The form of this Green's function is well known:

$$A_z = \frac{e^{-jk|r-r'|}}{|r-r'|} J_z \tag{6.4}$$

Where k is the wavenumber given by $\frac{2\pi f}{c}$. The electric field can be specified from (7.2). Actually computating this term, however, can be difficult due to the multidimensional term $(\vec{\nabla}\vec{\nabla}\cdot\vec{A})$. By making a far field approximation and because we are only concerned with sources and observations oriented in the z-direction, a simpler expression can be produced:

$$E_z = (-j\omega + cos^2(\theta))A_z \tag{6.5}$$

Note again that this is a far field expression and assumes that the source current density has only a vertical component, J_z, while the other components (J_x and J_y) are zero. Evaluating 7.4 according to the vector potential Green's function gives:

$$E_z = (-j\omega + cos^2(\theta))\frac{e^{-jk|r-r'|}}{|r-r'|} J_z \tag{6.6}$$

Applying the back propagator removes the phase and range term resulting in a value that is the quantity of interest (J_z) times a complex scale value, α.

$$|r-r\prime|e^{+jk|r-r\prime|}E_z = (-j\omega + cos^2(\theta))J_z = \alpha J_z \tag{6.7}$$

The double summation in 6.1 is necessary to complete the backpropagation imaging algorithm. When the propagator for an adjacent (empty) pixel is applied to the observation, the result does not add constructively. The final result is an image containing the "peaks" where scatterers truly exist and "zeros" elsewhere. Removing the scale factor and dividing by the number of elements included in the summations will produce the average current

density over all observation frequencies.

6.1.1 Inverse Problems

Inverse problems and radar imaging are closely related fields. A better statement is that radar imaging is a subset of the more general field of inverse problems. An imaging problem involves the collecting of observations of an unknown scene. Fourier methods (among others) are often used to construct the final image. Inverse problem methods are generally thought of as matrix operations that map a vector from an observation domain into a state domain. These often include the minimizing of a cost function and constraints (i.e. Lagrange multipliers) imposed on the solution. The observations are modeled as being produced by an operator applied to a state vector. This operator is called the forward operator. An adjoint operator is one that maps the data from the observation domain back into the state domain. Determination of the forward and adjoint matrix operators is a crucial part of the inverse problem.

$Inverse\ Problems$ is a well studied field [58]. It involves the use of cost functions to reconstruct a state vector from observations. The observations may have been corrupted in a random or deterministic way. The standard approach is to minimize the cost function to produce the best reconstruction. Lagrange multipliers [34] are used to add constraints on the final result based on known details of the problem. These constraints could be a "smoothness" or an "energy" or other knowns.

In this work the starting point is to assume a deterministic convolution with additive noise model [59],

$$\underline{y} = H\underline{x} + \underline{n} \tag{6.8}$$

Here $\underline{x}$ is a 2D or 3D image of scene reflectivity. H is the deterministic (but not necessarily fully known) forward process that transforms the scene of interest into the

observation domain. This is called the forward operator. $\underline{n}$ is the random contamination to the data in the form of additive noise.

A typical cost function to use is the sum of squared error: $L(\underline{x}) = \|\underline{y} - H\underline{x}\|^2$ where "$\|\cdot\|$" denotes the Euclidean norm [60]. Note that H^T implies hermitian (i.e. conjugate) transpose for complex valued H.

$$\underline{\hat{x}} = [H^T H]^{-1} H^T \underline{y}$$

If the noise, $\underline{n}$, is distributed as an i.i.d circularly Gaussian complex random variable ($(real(\underline{n}), imaginary(\underline{n})) \sim (N(\underline{0}, \sigma^2 I), N(\underline{0}, \sigma^2 I))$), then this solution is the Maximum Likelihood estimator of the scene $\underline{x}$.

This solution does not always produce the best reconstruction of the scene. Among the possible problems are numerical errors caused by matrix inversion. The use of prior information to constrain the solution is necessary. For the radar application, a highly useful tool is $sparsity$. This concept will be explored in Section 6.3.

6.1.2 Backpropagation as an Inverse Problem

The backprojection operation described above fits into the paradigm of an inverse problem as a linear estimator [Book -detection of signals in noise]. It makes no claims on the statistical distribution of the observation noise. Earlier we described the observation noise as circular Gaussian. This means that the real and imaginary part of the noise have the same variance and are independent. In this case the Minimum Variance Unbiased estimate of the scene will be given by the linear estimator [61]. ($scene$ here implies the average reflectivity over all observed frequencies.)

Let us now look at populating the forward operator with the necessary values to model a given scene. We start with just one frequency, f_0 with angular frequency $2\pi f_0 = \omega_0$. To populate the forward operator consider the n^{th} scene cell being observed at the m^{th} location. The approximate propagator as described above is given by:

$$h_{mn} = \frac{(-jw_0 + cos^2(\theta))e^{-jk_0R(m,n)}}{R(m,n)} \tag{6.9}$$

Where $R(m,n)$ is the distance from the n^{th} image pixel location to the m^{th} observation location and θ is the angle formed from the z-coordinate direction and the vector from image location to observation location. In the applications primarily considered here (i.e. see-through-wall and ground penetrating radar), θ is taken to be 0^o, so the cosine term vanishes. Also, in practice the jw_0 term is left out because it is just a complex scalar. This is done because the data is often uncalibrated.

With the definition of h_{mn} the forward process becomes:

$$y_m = \sum_{m=1}^{M} h_{mn}x_n \rightarrow \underline{y} = H_0\underline{x} \tag{6.10}$$

Since we are looking at a 2D or 3D scene, we say that the problem has been $vectorized$ by "unwrapping" the columns of the scene into an Nx1 vector.

Backpropagation is generally performed in a brute force way. That is, the back propagator is determined as $R(m,n)e^{jk_0R(m,n)}$ for a given cell with respect to a given observation. This occurs for each observation and the results are accumulated for the scene cell of interest. The algorithm then steps to the next cell. This can be done more efficiently by populating the forward operator and then multiplying the observations by its transpose:

$$\underline{\hat{x}_0} = H_0^T\underline{y}$$

The above forward operator was denoted H_0 to imply that only one frequency was included. Now let us expand the discussion to muliple frequencies. A forward operator can be populated for each frequency being observed. In the inversion process, the quantity of interest is the average reflectivity over all the frequencies.

$$\underline{\hat{x}} = H_1^T \underline{y}_1 + H_2^T \underline{y}_2 + \cdots + H_l^T \underline{y}_l$$

This can be reduced to a single operator H^T by horizontally concatenating the matrices as: $H^T = [H_1^T H_2^T \ldots H_l^T]$. This is applied to the vertically concatenated observation vector:

$$\underline{y} = \begin{bmatrix} \underline{y}_1 \\ \underline{y}_2 \\ . \\ \underline{y}_l \end{bmatrix}$$

To complete the average, each cell should be divided by L the number of frequencies.

6.2 Wavenumber Migration

Algorithms exist that can speed up the backrpopagation process. Wavenumber Migration is one of these. This term is synonymous with Seismic Migration [62], Range Migration [63], and Wavefront Reconstruction [64]. It requires that observations be made along a regular sampling grid. The forward process that generates the observations discussed in Section 6.1 is nearly a Fourier Transform of the scene reflectivity. Because it is not quite a Fourier Transform, applying an inverse Fourier Transform to the observations will not achieve the optimum resolution. Wavenumber Migration seeks to reconstruct the 2D or 3D Fourier spectrum of the scene. In the end, the image is produced by an inverse FFT. The use of FFTs allows for much faster production of the desired image.

$$d(x,z) = \frac{1}{(2\pi)^2} \int \int D(k_x, k_z) e^{j(k_x x + k_z z)} dk_x dk_z \tag{6.11}$$

This is a 2D Fourier Transform of the received data after proper conditioning. $D(k_x, k_z)$ is an altered form of the 2D Fourier Transform of $r(x,t)$, the time domain Fourier Transform of the waveform received by the radar and the spatial domain Fourier

Transform of the data in the x-direction.

$$D(k_x, k_z) = R(k_x, k_z)F(k_x, k_z) \tag{6.12}$$

A change of variables is performed to go from $R(k_x, \omega)$ to $R(k_x, k_z)$ space in this expression. This conversion involves solving the dispersion relation for and then interpolating the samples onto an equally spaced sampling grid in the k_z domain. The dispersion relation is given by:

$$k_z = \sqrt{(\frac{2\omega}{\nu})^2 - k_x^2} \tag{6.13}$$

This implies that proper imaging requires knowledge of ν, the speed of light in the medium. In practice the change of variables and interpolation step is conducted in the Stolt Interpolation stage. The $F(k_x, k_z)$ function is a phase compensation term that is often called $the\ matched\ filter$. It has the following form:

$$F(k_x, k_z) = \frac{|k_z|}{\sqrt{k_x^2 + k_z^2}} e^{-j(\sqrt{k_x^2+k_z^2} - k_z)z_0} \tag{6.14}$$

Figure 6.8 illustrates wavenumber migration in block diagram form [63]. Since the algorithm is linear an entire image with multiple scatterers is applied in the same manner.

6.2.1 Landmine Imaging with Wavenumber Migration

Vehicle based landmine detection systems employ a suite of sensors. These sensors often include metal detectors and ground penetrating radar. Metal detectors naturally perform well in detecting metal landmines. They also will detect any other metal in the vicinity of the sensor. One approach to eliminating unwanted detections of non-threatening metal objects is to utilize a ground penetrating radar (GPR). Since GPR can determine range and

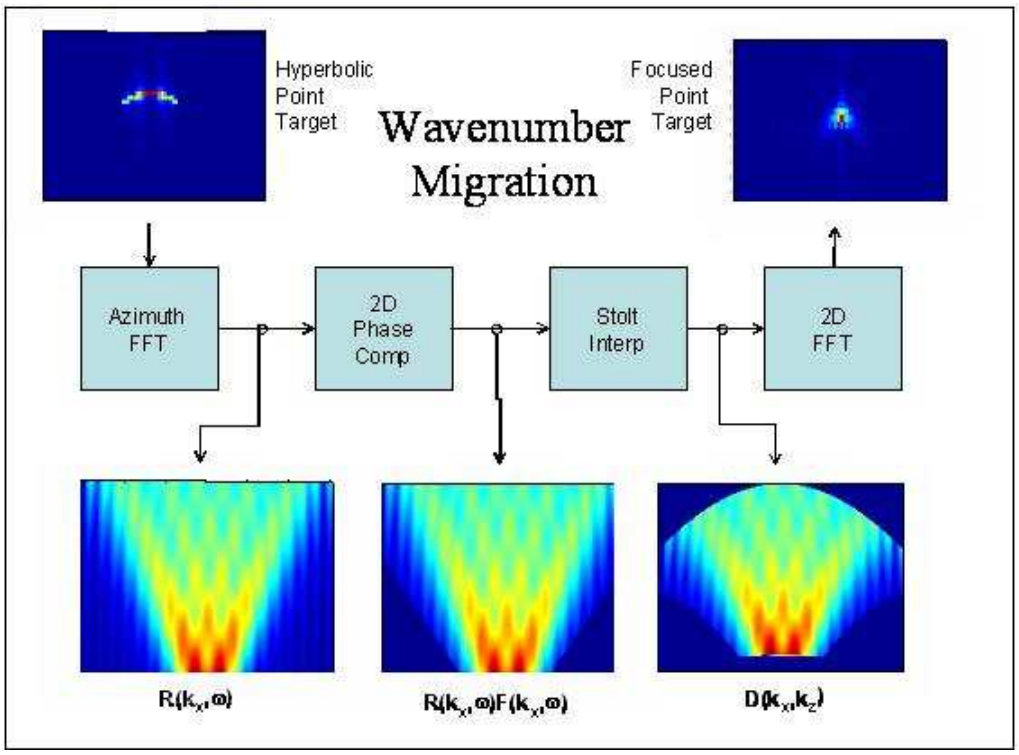

Figure 6.1: Block Diagram of the Wavenumber Migration Process

can be imaged using synthetic aperture radar techniques, it can be used to determine the burial depth and size of an object detected by a metal detector.

In this paper an imaging technique called wavenumber migration is employed, and an automated algorithm is presented for finding the depth and burial size of objects. Since landmines are typically buried at depths between 3” and 10” (to the top of the mine) and have a diameter on the order of 1’, knowledge of size and depth can provide great insight in identifying the object or at least in determining that an object cannot be a landmine.

In a battlefield environment many metallic and non-metallic objects will be strewn across the field. One example of a non-threatening metal object is a spent rifle cartridge. There could be thousands of these objects lying on the surface of a battle field. Even though these objects are small, each one will be very detectible to a metal detector. The ability to determine that these objects are too small to be a landmine will allow them to be eliminated from a detection report.

In this study ground penetrating radar data is utilized to estimate the size and shape of a Russian TM-62M landmine. It will be shown that using the wavenumber migration algorithm to image the radar data consistently provides a signature from which estimates of size and depth can be made. A repeatability study has been conducted using ten independently measured signatures from the same landmine. The essence of the algorithm is that the imaging process resolves reflections from the top and bottom of the landmine. This allows an automated algorithm to extract the depth and size of the resolved edges. Preliminary results show that depth and mine height can be measured to about 0.5" accuracy. This is the size of one resolution cell in depth. Landmine diameter can be measured to an accuracy of about 2.5".

Stepped Frequency Ground Penetrating Radar

One method for building a cost effective GPR system is known as Continuous Wave, Stepped Frequency Radar. In this approach, each antenna is pulsed with N frequencies in a stepped fashion. That is, one single antenna transmits a single tone for a specific time duration - the dwell time. After this dwell time, the response of the earth is sampled. Then the tone is stepped up (or down) in frequency by a specified amount. For example 256 samples can be collected for the frequency span from 500MHz to 2000GHz with frequency steps of 5.86MHz. Below is a detailed description of the depth and azimuth processing of this signal to produce an image of the landmine. Because of the frequencies used and the size of the targets of interest, only reflections from the top and bottom edges of the landmine can be seen. Despite the low resolution nature of the data, the image obtained is enough to extract depth and size estimates.

Depth Processing

The ground response to a continuous wave, stepped frequency radar can be thought of like a black box. The radar inputs sinusoidal signals at known frequencies and amplitudes into the inputs of the black box. At the output, the radar samples the amplitude and phase

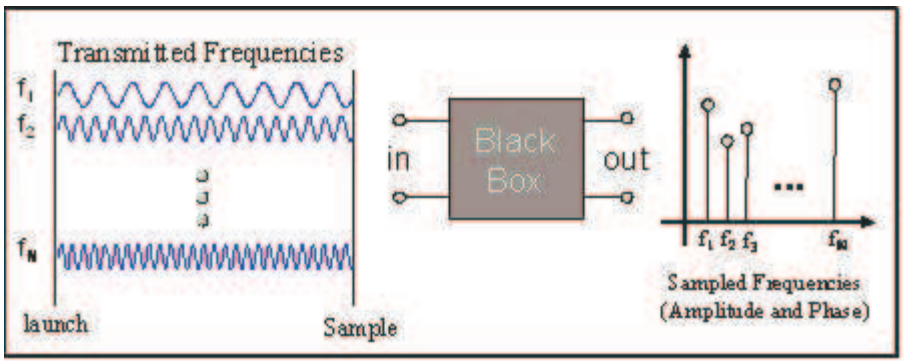

Figure 6.2: The antennae and ground may be viewed as a black box.

response to that frequency.

This is like making a direct measurement of the system's frequency response (i.e. Transfer Function). A Discrete Fourier Transform using an FFT algorithm converts frequency information to depth. This works because the response of the ground has the form:

$$r(f) = \int_{z=0}^{\frac{\nu\tau}{2}} \rho(z) e^{j\frac{2\pi f}{\nu}2z} dz \tag{6.15}$$

Where ν is the speed of propagation in the medium and z is the depth. At the moment the receiver samples the return echo, energy from the continuous wave will be returning to the receive antenna from the surface to a depth of $\nu\tau/2$. Where τ is the length of time a tone is transmitted - the dwell time. If the dwell time is $0.15\mu s$, then in free space this depth would be $22.5m$. However, the effect of propagating in a medium other than free space is that the speed of propagation decreases. A typical decrease for a non-lossy earth is a factor of 3. So this depth window would be reduced by the medium to around $7m$.

The dwell time determines the depth that will potentially receive energy from the radar during the transmission of a single pulse. However, this energy will undergo attenuation as it propagates into the ground. So the entire $7m$ of depth may not actually receive any illumination due to the energy attenuating away. It is important to consider both the dwell

time and the penetration depth when choosing the frequency step size. The frequency step determines a depth, Z_{max}, below which all energy must be attenuated to prevent aliasing of the return signals. Objects that are illuminated by the radar, and echo back a signal, but are beneath this Z_{max} depth will "fold into" (i.e. alias into) the depths less than Z_{max} . They will appear in the final output as an object with the wrong depth. In radar terminology, Z_{max} is called the unambiguous range.

To prevent aliasing from occurring, the frequency step should be chosen properly. The expression for Z_{max} as a function of step size is given by:

$$Z_{max} = \frac{\nu}{4\pi\Delta f} \approx \frac{c}{4\pi\sqrt{\varepsilon_r}\Delta f} \tag{6.16}$$

The final form of this expression is approximate. The velocity of the wave is equal to the speed of light divided by the square root of the relative permittivity ε_r, only if the medium is weakly lossy [16].

If we assume that ε_r is 9, then a dwell time of $0.15\mu s$ will illuminate $7m$ of the ground. A proper choice of Δf to prevent the aliasing is then:

$$\Delta f = \frac{c}{4\pi\sqrt{\varepsilon_r}Z_{max}} = \frac{3\times10^8}{4\pi\sqrt{9}7} = 1.14MHz \tag{6.17}$$

It should be noted that the dwell time can be longer than $0.15\mu s$ for the situation above, if it is known that the lossy material will prevent the energy from propagating past $7m$. (For soil, this is a pretty good bet.) In this case the deeper targets cannot alias into the shallow region since they do not return enough energy to the radar to be measured. The examples shown in Section 3.1 were sampled with a frequency step of $5.86MHz$. This corresponds to an unambiguous range of $1.4m$.

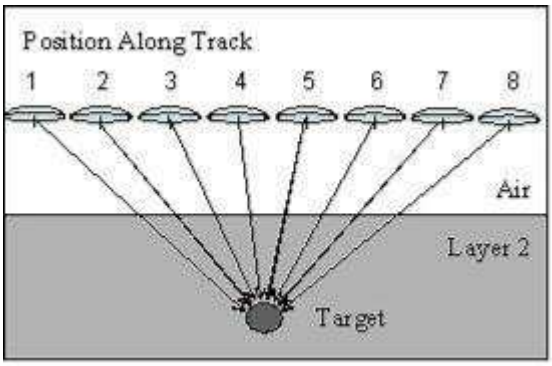

Figure 6.3: Geometry of Signature Collection

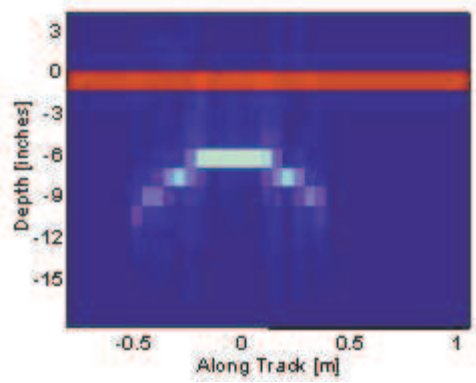

Figure 6.4: Simulated Signature

Azimuth Processing

In the azimuth (along track) direction, the collection of the radar returns gives rise to a special signature that can be exploited to remove false alarms produced by non-real objects. Real objects have a hyperbolic shape characteristic [16].

Figure 6.3 shows the geometry of an antenna passing over the top of a buried object. In free space the distance from the antenna to the object at position x_i (and $z = 0$) is given by:

$$d = \sqrt{(x_i - x_0)^2 + z_0^2} \tag{6.18}$$

Where the object is located at (x_0, z_0). This distance affects the radar response $r(x, t)$

as a time delay from transmission of the sinusoidal tone to its reception.

$$r(x,t) = e^{-j2\pi f(t_0 - \frac{2d(x)}{\nu})} \tag{6.19}$$

Here t_0 is the time when the radar launched the tone, and f is the frequency of the tone. (This expression contains only the phase information. The amplitude effects due to attenuation, propagation loss, input power, and other physics is not shown. It is a normalized expression.) To produce the signature of Figure 6.4 the time domain is Fourier Transformed (i.e., "range compressed") to produce $R(x,\omega)$.

After performing the depth processing described in Section 6.2.1, the signature shown in Figure 6.4 is the result. The hyperbolic characteristic is a result of the changing distance from the radar antenna to the object, $d(x)$. As the antenna approaches its closest point of approach (directly above the object) the return reaches the apex of the hyperbola. Then as the antenna moves on the response moves further away until it passes out of the antenna beam. The signature of Figure 6.4 was produced using a point target simulator operating from $500MHz$ to $2GHz$. This bandwidth provides a depth resolution of 4" in free space. Because the soil slows down the propagation of the energy by a factor of $\frac{1}{\sqrt{\varepsilon_r}}$, the resolution is improved. If ε_r is 9 (i.e. 9 times denser than free space), then the resolution in depth improves to 1.3".

6.2.2 Matrix Implementation

A powerful and novel way to implement Wavenumber Migration is as a matrix operation. All the steps shown in Figure 6.8 can be placed into a correction matrix. This would give the imaging operation the form $\hat{X} = vect^{-1}[\Psi vect[Y]]$. Where $vect$ and $vect^{-1}$ denote the operation of vectorizing. The correction matrix Ψ is composed of the following matrix operators:

$$\Psi = Q_2^{-1}\Phi Q_1 \tag{6.20}$$

Here the Q_1 operator is a 1D FFT. This corresponds to the first step of Figure 6.8 and places the observations into the $\Omega - k$ space. This operator is straight forward as it conducts a 1D FFT operation. The Q_2 operator, however, is quite complicated. It is the matrix implementation of a 2D FFT, which performs the final step of Figure 6.8. Note that the notation Q_2^{-1} denotes a 2D inverse FFT. The remaining two steps can be eloquently folded into the Ψ matrix.

For practical reasons it is best to implement the Q_2 and Q_1 operations with standard FFTs. We will, therefore, only present the contents of the Φ matrix and use the following operation to implement wavenumber migration:

$$\hat{X} = vect^{-1}[FFT_2^{-1}(\Phi vect[FFT_1(Y)])] \tag{6.21}$$

FFT_1 here implies the 1D FFT and FFT_2^{-1} denotes the 2D inverse FFT.

The interpolation step was originally reported by Stolt [65]. This is a 1D interpolation between sampled frequencies in the wavenumber domain. To implement this operation as a matrix we can start with the simple two point (linear) interpolator. Equation 6.22 shows this. If we denote the set of observations by $y[n, m]$ where n corresponds to the n^{th} spatial location along the synthetic aperture and m corresponds to the m^{th} transmitted frequency, then the Stolt interpolation can be written:

$$y'[n, m] = a_m y[n, m] + b_m y[n, m + 1] \tag{6.22}$$

This operation can be placed into a sparse matrix, which we call Φ_s (the Stolt Interpolation Operator).

$$\Phi_s = \begin{bmatrix} a_1 & b_1 & 0 & 0 & & 0 & 0 \\ 0 & a_2 & b_2 & 0 & & 0 & 0 \\ 0 & 0 & a_3 & b_3 & \cdots & 0 & 0 \\ & \vdots & & & & & \\ 0 & 0 & 0 & 0 & & a_M & b_M \end{bmatrix} \tag{6.23}$$

The values of a_m and b_m must be populated as required for the two-point linear. Here, k_m denotes the wavenumber at the m^{th} frequency and k'_m is the wavenumber of the interpolated observation.

$$k_m = \frac{4\pi f_m}{c} \tag{6.24}$$

$$a_m = \frac{(k'_m - k_m)}{(k_{m+1} - k_m)} \tag{6.25}$$

$$b_m = \frac{(k_{m+1} - k'_m)}{(k_{m+1} - k_m)} \tag{6.26}$$

The value of k and k' are known a priori, so the matrix operator of Equation 6.23 can be populated.

Any number of other interpolation approaches can be used. However, if the observations have been sampled densely enough, the linear approach described above is sufficient. Since this matrix is quite sparse, the linear approach allows for a fast and efficient implementation.

To complete the development of the Φ matrix, the phase correction step must be added to Φ_s. This is done by placing the phase corrections into the a_m and b_m coefficients [63]. Equation 3.5 contains the necessary changes:

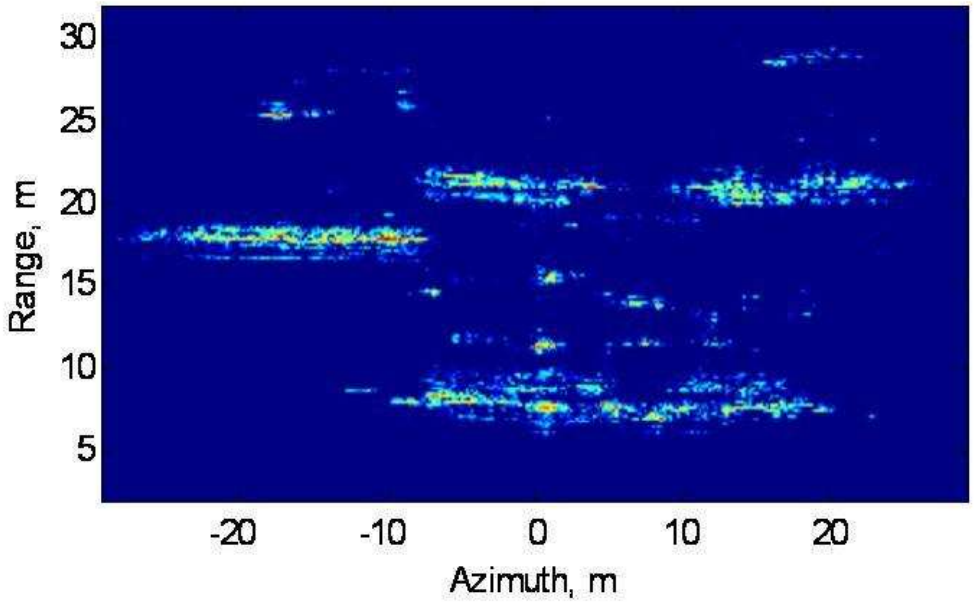

Figure 6.5: STW Radar Example: Wavenumber Migration

$$a'_m = \frac{(k'_m - k_m)}{(k_{m+1} - k_m)} e^{-j(k_m - k'_m)R_s} \tag{6.27}$$

$$b'_m = \frac{(k_{m+1} - k'_m)}{(k_{m+1} - k_m)} e^{-j(k_{m+1} - k'_m)R_s} \tag{6.28}$$

R_s here is the slant range distance from the aperture to the scene center line. With this change the Φ_s matrix becomes the Φ matrix used to correct the observations in preparation for the 2D inverse FFT.

6.3 Exploiting Sparsity as Prior Knowledge

Radar detects waves that are scattered by a change in the environment. For example a change in the dielectric parameter of the medium. This could be a wall, or the ground, or a cloud, etc. As a result imaging the scattered fields reveals a mapping of the edges of

structures in the environment. As a result radar is an effective edge detector.

$Sparsity$ is a concept that refers to the number of voxels in an image that are non-zero. Since radar detects edges, the images produced are often quite $sparse$. Fewer than 25% of the pixels may actually contain non-zero information. We seek to make use of this information in our image reconstruction algorithms.

A novel approach to incorporating a $sparse\ prior$ is reported in [66]. The approach models radar image intensities with a probability density function.

$$f(x) = (1-\omega)\delta(x) + \omega a e^{-a|x|} \tag{6.29}$$

The delta function in this expression states that a number of intensity values are exactly zero. The other part of the expression models the continuous distribution of non-zero voxel intensities as an exponential PDF. This is slightly different from the approach taken by Ting in [66] where a two sided exponential was used. In the radar intensity application, however, intensity values are positive numbers. This PDF with its ω and a parameters represent the $sparse\ prior$.

Incorporating the $sparse\ prior$ into an inverse problem as described before is not straight forward. It cannot be applied easily as a Lagrange Multiplier. Instead a novel approach is used that utilizes an expectation maximization approach on a voxel by voxel basis [59]. This takes the following E and M step form [67] :

$$\begin{aligned} (E)\ \ \hat{Z}^{(n)} &= \hat{X}^{(n)} + \alpha H^T (Y - H\hat{X}^{(n)}) \\ (M)\ \ \hat{X}^{(n+1)} &= \arg\min_X \Big(\frac{\|\hat{Z}^{(n)} - X\|^2}{2\sigma^2} + \log f(X) \Big). \end{aligned} \tag{6.30}$$

The E Step is a Landweber iteration. It functions as a control loop that projects the data back and forth between the image and observation domains. The starting point for this process is $\underline{\hat{x_0}}$, which could be either a backpropagated or wavenumber migrated image.

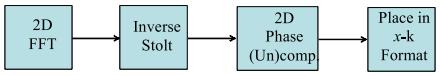

Figure 6.6: Block Diagram of Reverse Wavenumber Migration - An approximation to the Forward Operator

Here the adjoint and the forward operators could be implemented as in Section 6.1. As mentioned earlier, however, memory issues begin to make the straight forward application of H and H^T intractable. Instead, the function of H^T is implemented as an imaging step using Wavenumber Migration. The function H is implemented in an extremely novel way as $Inverse\ Wavenumber\ Migration$. Introduction of the Reverse Wavenumber Migration (un)-Imaging is found in [60].

$Inverse\ Wavenumber\ Migration$ is motivated by the $Method\ of\ Moments$. It is a way of propagating the estimated reflectivity of the scene back to the observation domain. The process is shown in the block diagrams of Figure 6.6 and 6.7.

By implementing the forward propagator H as inverse wavenumber migration, all the power of this imaging technique is brought to bear. The iterations are quite fast. A 256 x 256 scene can be processed without sparsity in under 7 seconds with a laptop computer.

The M step can be implemented as a soft threshold [67]. The sparsity information is contained in the details of the soft thresholding. Namely, the threshold setting is determined by the sparsity parameters.

The following steps impose a sparse prior on radar imaging using wavenumber migration. As described previously a Landweber iterative method is used.

(1) $\hat{x}_0$ = Wavenumber Migrated Image

(2) $Z_0 = softthreshold(\hat{x}_0)$ Soft Thresholding

(3) $\hat{y}_1 = H\hat{Z}_0$ Propagate the fields back to the observation domain.

(4) $\epsilon_n = y - \hat{y}_n$

(5) $\hat{x}_{n+1} = X_n + H^T\epsilon_n$

(6) iterate

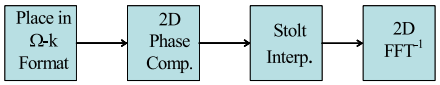

Figure 6.7: Block Diagram of Wavenumber Migration

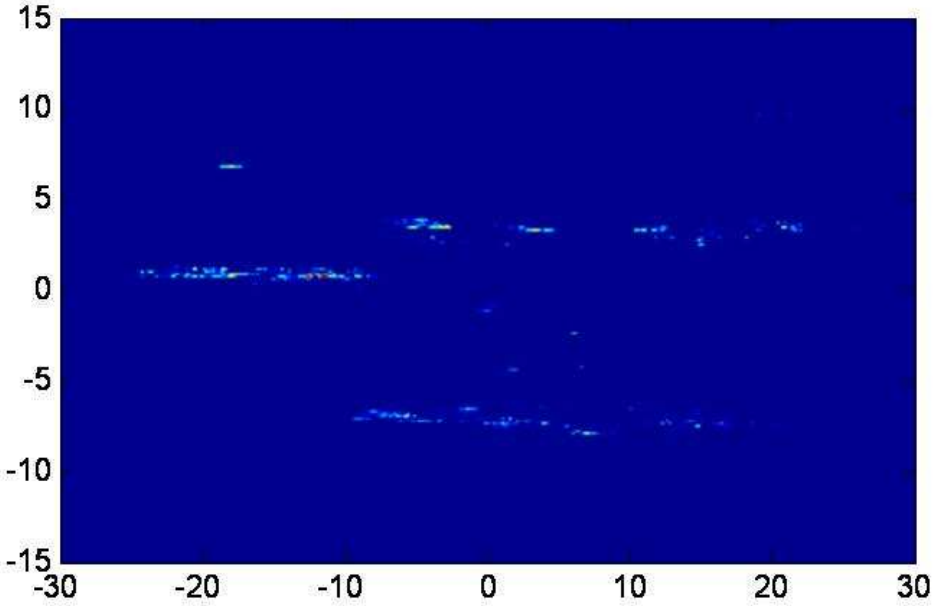

Figure 6.8: STW Radar Example: Sparse Reconstruction

CHAPTER VII

ITERATIVE REDEPLOYMENT OF IMAGING AND SENSING

7.1 Phenomenology of See-Through-Wall Radar

Geometrical Optics (GO) is a method of approximating electromagnetic wave propagation. Due to the simplicity of its form, it is powerful for solving problems and accurate at higher frequencies. This method is synonimous with “ray tracing”. For the STW application, some special assumptions have to be made within the approach. Because the hand-held radars being considered here are often near the building, the electric fields emitted and reflected are considered to be spherically spreading waves. At the interface with the wall, however, the waves are treated as plane waves. This allows for the prediction of field transmission and reflection by Fresnel scattering parameters at material interfaces [68] [69]. Thus, it allows for the modeling of diffraction within the wall and also accounts for ray attenuation and slowed propagation speed within the wall. Refraction of the plane waves is addressed by Snell’s Law [12]. In addition, scattering objects are viewed as point scatterers with a radar cross section, which determines the amount of energy reflected [70] [71]. These assumptions hold as frequency increases. This technique is being called Enhanced Geometrical Optics (EGO).

Two versions of Enhanced Geometrical Optics are used in this work to provide simulated data and to allow for information gain computation. The first of the two simulators is the monostatic case, which provides observations that emulate a backscattering radar. The second is the bistatic simulator, which provides electric field

predictions for the virtual transmitters.

Monostatic RADAR Model

Radar can be operated in a number of configurations. The most traditional is a single antenna that operates as a transmitter and receiver. This configuration measures the backscatter response of objects, and is referred to as monostatic. In lieu of observations made by a real radar system this work utilizes the EGO monostatic radar for simulating the data. In this section, the operation of the EGO monostatic radar will be described mathematically.

Radar is often described as operating in the time domain or the frequency domain. A time domain system transmits some predetermined time waveform, waits for the signal to propagate to the scene of interest, then ”listens” to the response. Subsequent processing of the signal is required to form an image of the scene. A frequency domain system, on the other hand, will transmit a set of tones. This can sometimes be done simultaneously or in a stepped fashion. A robust way to implement a radar system is the single tone stepped frequency approach. The radar begins transmission of an initial frequency, then samples the return of that tone from the scene. It then steps to the next frequency, transmits, and samples. This process is performed for all frequencies of interest [72]. Ultimately, the two approaches are mathematically identical. They only differ in their implementation. By a careful weighting of the stepped frequencies, the stepped frequency radar can emulate any time domain waveform.

The mathematical model for a monostatic radar under the EGO assumptions is shown in Equation 7.1 and 7.2. Equation 7.1 models the return from the object behind the wall. The modeled quantity is the observed electric field at location x for frequency f.

$$E_R(f,x) = E_0 \left[\left(\sqrt{\frac{G_T G_R}{(4\pi(h+\tau+d)^2)^2} \frac{(\lambda)^2}{4\pi} \sigma_{RCS}} \right) T_{12}^2 T_{21}^2 e^{-2\alpha\chi} e^{-j2\beta\chi} \right] e^{-j2k(h+d)} \quad (7.1)$$

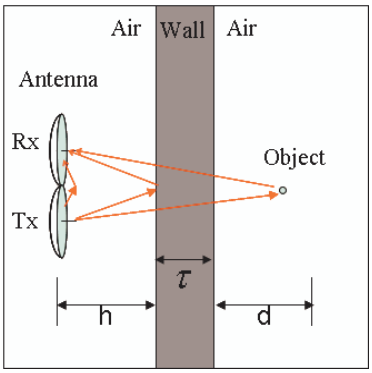

Figure 7.1: Geometrical Optics Wall Model

This expression comes from the radar equation - a well known approximation used widely in the design of wireless communication systems. In the expression's original form, the starting point is input power P_0. This is reflected in Equation 7.1 as the system constant E_0. The power put into an antenna is transduced into the surrounding environment with a gain of G_T. This power spreads spherically from the antenna producing an energy density over the sphere of $\frac{P_0 G_T}{4\pi R^2}$. Where R is the radius of the enclosing sphere. This energy density at the location of the object induces electric currents in the object, which re-radiate to form the scattered field. The radar cross section σ_{RCS} captures the strength of the reflected power. This power then spreads spherically incurring another $4\pi R^2$ loss when it reaches the antenna. In the act of sensing the reflected power, the antenna collects $G_R \frac{\lambda^2}{4\pi}$. The $\frac{\lambda^2}{4\pi}$ term is a conversion factor that changes the antenna gain value to the effective area of the antenna [73]. A simple way of approximating the received electric field amplitude is to take the square root of this received quantity. The polarization of this field is generally considered "out of the page".

The phase approximation follows from the time harmonic spherical Green's Function. That is the phase is given by: $e^{j(\omega t - kR)}$. Here ω is the radial frequency and t is time. The time contribution is often suppressed during calculations. The phase of the spherically spreading electric field is therefore: e^{-jkR}, where k is the wavenumber, which is given by: $k = 4\pi \frac{f}{c}$. The 4π arises from this being round trip phase. Also, c is the speed of light in a vacuum.

Up to now only the standard radar equation has been introduced with a square root to approximate electric field and a phase term that comes directly from the 3D time harmonic Green's Function. Now, the wall is introduced. To handle it, we assume that the incident wave is a time harmonic plane wave. This means that the wall is considered to be an infinite slab of homogenous material with a constant permittivity ϵ_2 and thickness τ. Penetration of the electric field is governed by the Fresnel transmission coefficients T_{12} and T_{21}. The electric field amplitude is attenuated inside the material by a frequency dependent dampening factor: $e^{-2\alpha\tau}$. And, finally, the phase term inside the wall is governed by $e^{-2j\beta\tau}$.

This completes the pieces of the EGO model as described by Equation 7.1. Note that T_{12} and T_{21} correspond to the transmission coefficient from free space into the material and from the material into free space respectively. These coefficients are squared because the wall is traverse twice in the round trip.

The model can be expanded to include the response of the wall. Equation 7.1 shows the direct return from the front of the wall as implied by Figure 7.1. A more complete model would include the return from the back of the wall and also multiple bounces between the front and back.

$$E'_R(f,x) = E_0 \left[\left(\sqrt{\frac{G_T G_R}{(4\pi h^2)^2} \frac{(\lambda)^2}{4\pi}} \right) R_{12} \right] e^{-j2kh} \tag{7.2}$$

This expression is derived using similar arguments to Equation 7.1. In this case the Fresnel reflection coefficient R_{12} is used to capture the field reflected from the front of the wall interface. The final observation made by the monostatic radar is the sum of the return from the object and the return(s) from the wall.

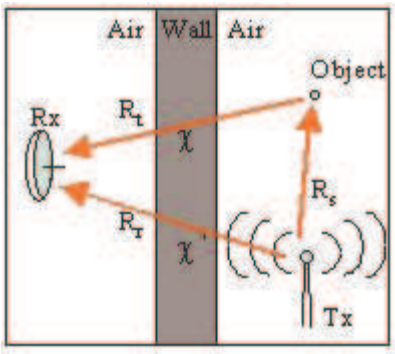

Figure 7.2: Geometrical Optics Bistatic Model

Bistatic RADAR Model

The virtual transmitter concept places (virtually) an omnidirectional transmitter inside the building being imaged. It does this by generating a building model composed of discrete scattering elements. A numerical electromagnetic prediction of the fields produced by the virtual transmitter is computed for locations outside the building. This field is used to predict locations where the best measurement conditions exist from which to re-illuminate the location of the transmitter.

To support this stage of the algorithm, an extended geometrical optics model for forward scattering has been developed. This model is called bistatic because the receiver and the transmitter are not co-located. Figure 7.2 illustrates the concept.

$$E_R(f,x) = E_0 \left[\left(\sqrt{\frac{G_T G_R \lambda^2}{((4\pi)^3 R_s^2 R_t^2} \sigma_{RCS}} \right) T_{12} T_{21} e^{-\alpha\chi} e^{-j\beta\chi} \right] e^{-jk(R_s+R_t-\chi)} \qquad (7.3)$$

The bistatic model is mathematically developed with similar arguments as the monostatic model. Equation 7.3 is the result.

Here the parameter R_s is the distance from the transmitter source to the scattering object, R_t is the distance from the object to the receiver, and, χ is the straight line distance of the path within the wall medium. In this bistatic version, the radar cross section σ is the non-backscatter RCS. For simplicity, this parameter is considered constant regardless of the illumination and observation directions. This does not in general have to be true. The scattering objects could have directional qualities, which would be represented by an RCS

function $\sigma(\theta, \phi)$. Note that this expression no longer contains round trip distances.

The direct path from the transmitter to the receiver passes through the wall. Equation 7.4 describes the link including the wall's contribution. The R_r parameter is the transmitter to receiver distance.

$$E'_R(f,x) = E_0 \left(\sqrt{\frac{G_T G_R \lambda^2}{(4\pi R_r)^2}} \right) T'_{12} T'_{21} e^{-\alpha \chi'} e^{-j\beta \chi'} e^{-jk(R_r - \chi')} \tag{7.4}$$

The observed field measured by the receiver is the sum of Equation 7.3 and 7.4.

7.2 The Outer Wall Problem

Approximations and simulations are used in this work to gain physical insight into the spatial signatures produced by objects observed by surface penetrating radar. The radar system is a receiver/transmitter pair that scans along the outside of a building. The returns can be used to produce an image (slice) of the interior of the room.

The imaging approach used in this work is wavenumber migration. It was first introduced in synthetic aperture radar imaging by [62]. The method was first developed for seismology [63], [74]. The principal contribution of this paper is the application of this approach to See-Through-The-Wall radar imaging.

The wavenumber migration algorithm works as follows. The 2D complex spectrum of the image is constructed by properly reformatting the plane waves received by the radar system. The reformatting requires exact knowledge of the phase of the propagating waves. When a wall of unknown thickness and permittivity is introduced, the algorithm can no longer focus the image because the wall imposes an unknown delay on each plane wave due to the decreased and unknown propagation speed within the wall. To properly reformat the waves, the wavenumber migrator must know the bulk effect of these two parameters (unknown permittivity and unknown thickness) and remove that phase delay from the recorded data.

Adding to the complication of this problem is the fact that the reflection coefficients of the wall are unknown. In this work we will assume that the radar return from the wall is composed of a reflection from the front surface and a reflection from the back surface. These two returns sum together to form a signal in noise with two unknown reflection coefficients and one unknown phase. Due to the non-linear nature in which these three parameters manifest themselves in the returned signal, some assumptions will have to be made in order to estimate them. Two approaches can be considered.

The first approach assumes that the reflection from the wall surface has been removed by some other means. This greatly simplifies the problem and allows for the back of the wall reflection coefficient and the phase at all required frequencies to be removed using a sine and cosine or dual phase technique. This approach is, therefore, a non-parametric approach that estimates the phase at all frequencies. In practice, it may be a significant technical challenge to eliminate the surface reflection contribution as required by this method. Therefore, a second technique is proposed.

The second technique is a dual frequency approach. Here it is assumed that the frequencies are close enough together so that the reflection coefficients of the wall are nearly constant in frequency. The phase unknown is reduced to its fundamental unknown part, which is the product of the wall thickness τ and the square root of the wall permittivity $\sqrt{\epsilon_2}$. By relying on a cross-demodulated signal (that is a transmitted cosine mixed with a sine on receive) the wall return is naturally rejected. Two separate soundings are made at the two frequencies. After the cross-demodulation the reflection coefficient of the back of the wall and the phase parameter are non-linearly coupled within the signal. A non-linear iterative maximum likelihood estimation approach is used to separate these two parameters via the Newton-Raphson algorithm. When this algorithm converges, it provides a parametric estimate of the thickness-permittivity-squareroot product. With this estimated parameter, the phase delay for any frequency of interest can be predicted.

We adopt a physical optics model for electromagnetic wave propagation for a simple

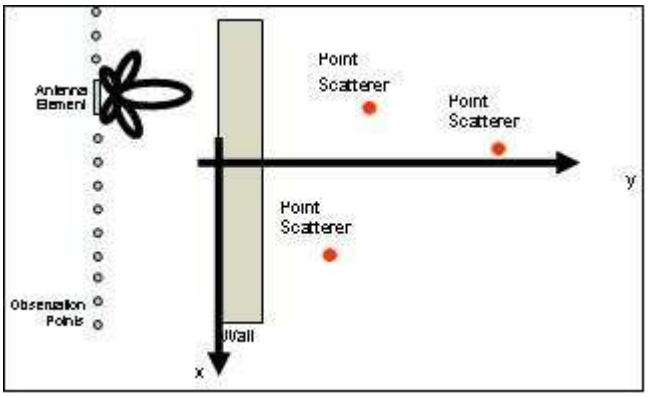

Figure 7.3: Three Point Scatterer Simulations

environment consisting of three point scatterers placed behind the wall. These simulations are used to show the result of correcting the imaging signals with the estimated phase. Images produced without phase correction are also provided to demonstrate the need for correcting unknown phase distortion.

7.2.1 Point Target Simulations

The simulation consists of a stepped frequency radar generating frequencies from 500MHz to 2.5GHz with equal steps, a homogeneous wall, and three point scatterers. Figure 7.3 shows the point scatterer arrangement. The radar is pointed directly at the wall. The imaging algorithm operates on a measurement of radar backscatter at 256 frequencies observed at 201 locations parallel to the wall. We define a local coordinate system (also shown in Figure 7.3) at a specified center of the generated image.

We employ a physical optics model of radar wave propagation through the medium. Specifically, the radar rf field is mathematically modeled as plane waves. The reflections from the wall and back of the wall are governed by Fresnel Reflection Coefficients, which are valid for time harmonic plane waves. For this work, refraction effects predicted by Snell's Law have been ignored for simplicity. Snell's Law predicts that the waves will be bent as they enter and leave the non-free space media In this paper we neglect this effect and assume that the waves travel straight through the wall regardless of angle of incidence.

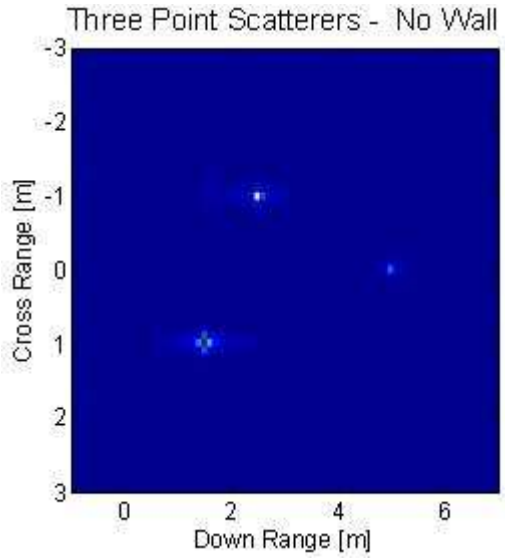

Figure 7.4: Point Simulation - No Wall

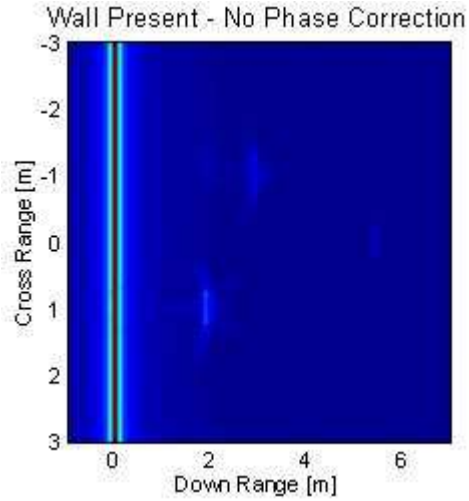

Figure 7.5: Point Simualtion - Wall Inserted

The imaging algorithm used to reconstruct the image of the three point scatterers is wavenumber migration. This method transforms the received signals into the 2D frequency space and manipulates the phase of each wavenumber. Interpolations (i.e. resampling) is also applied to format the data properly in preparation for a 2D inverse FFT. With correct interpolation and phasing, the energy of point scatterers become focused [63]. This can be seen in the free space (no wall) simulation shown in Figures 7.4 & 7.5. The 3 point scatterers are clearly well focused into point targets in this simulation. Their amplitudes can be seen to fade for targets that are further away from the wall. This is due to the $\frac{1}{r^2}$ spherical spreading of the energy in the transmitted wave. In these simulations the radar is just 6 meters from the farthest point scatterer. At these distances beam divergence loss of the transmit energy can't really be ignored. The point targets have the same radar cross section (10dB).

Figure 7.5 shows the motivation of this work. When the wall is inserted between the radar and the point scatterers, the imaging algorithm cannot focus the points. This is due to an unknown phase factor that is now present in the data stream. A simplified model of the observations is given by Equation 7.5.

$$y(f,x) = a_p(f)e^{-j\phi_p(f,x)}a_w(f)e^{-j\phi_w(f,x)}\rho_n e^{-j\phi_n} \tag{7.5}$$

The amplitude and phase labeled a_p and θ_p are due to the free space propagation between the radar and the n^{th} point scatterer. The complex reflectivity of the scatterer is given in amplitude by ρ_n and ϕ_n. The effect of the wall is to produce an attenuation and phase (both of which are unknown) given by a_w and ϕ_w.

Under this model the wall acts as a filter that attenuates some of the incident energy. If this is a function of frequency, it would have to be estimated, if the goal is to reconstruct the true reflectivity of all the pixels in the image. On the other hand, if the goal is to reconstruct the location of the scatterers in the image, the amplitude attenuation can be

ignored [63]. Of course, in the presence of noise or interference the power transmitted by the radar must be enough to provide a usable signal-to-noise ratio of the received amplitudes. The effect of the phase w is to distort the reconstructed image. Hence the phase must be estimated explicitly prior to image reconstruction Note that the wall parameters are the same for all simulations in this work: relative permittivity of the wall is 10 and it is 0.2 m thick.

7.2.2 Wall Phase Determination and Correction

Two methods are proposed here for determining the phase caused by a wall of unknown permittivity and unknown thickness. Both methods utilize a pulsed radar. The pulses contain a cosine waveform with just 1 frequency that lasts 100 μsec. The return signal is assumed to be a superposition of two cosine functions. The first is from the surface of the wall and the second is from the back of the wall. Equations 7.6 and 7.7 shows the expected return.

$$r(t) = a_0 cos(\omega t - \phi_p) + a_1 cos(\omega t - \theta - \phi) + n(t) \tag{7.6}$$

$$\theta = \frac{4\pi f}{c} h \tag{7.7}$$

$$\phi = \frac{4\pi f}{c} \tau \sqrt{\epsilon_2} \tag{7.8}$$

The θ parameter is the expected phase delay due to the waveform propagating to the wall surface and back to the radar. It is reasonable to expect this value to be known. The ϕ parameter, on the other hand, contains the $\tau\sqrt{\epsilon}$ value that is unknown. The α_0 and α_1 values are related to the reflection coefficients of the front and back wall surface. The

noise $n(t)$ is an unknown, performance limiting factor.

Dual Phase Approach

The first approach demodulates the returned pulse with a cosine and a sine waveform. This would be the same as transmitting a cosine and a sine signal and demodulating them both with a cosine. The result is an in-phase and quadrature measurement.

$$R(\omega) = \frac{1}{N}\sum_{i=1}^{N} r(t_i)cos(\omega t_i - \theta)R(\omega) = \frac{a_0}{2} + \frac{a_1}{2}cos(\phi) \tag{7.9}$$

$$Q(\omega) = \frac{1}{N}\sum_{i=1}^{N} r(t_i)sin(\omega t_i - \theta)Q(\omega) = \frac{a_1}{2}sin(\phi) \tag{7.10}$$

Equations 7.9 & 7.10 show the processing steps and the final scalar values. It is assumed that the sampling rate is sufficiently high to prevent aliasing. Note that all the unknown parameters appear in these scalar measurements. A separate measurement must be made at each frequency used in the imaging system.

A significant issue exists in the in-phase value. The a_0 term is the reflection coefficient of the wall surface. This value must be determined prior to the application of this dual phase method. This is the so-called ”layer peeling”. The wall surface must be determined, then the inner wall structure, then the imaging of the area behind the wall. Here we focus only on the solving of the middle problem - the inner wall structure. With the removal of the a_0 value, the in-phase measurement becomes what is shown in Equations 7.11

$$R(\omega) - \frac{a_0}{2} \rightarrow R(\omega) = \frac{a_1}{2}cos(\phi) \tag{7.11}$$

Now the form of the in-phase and quadrature values can be divided to remove a1 (unknown). The result is a tangent of the unknown phase. By taking an arctangent, the

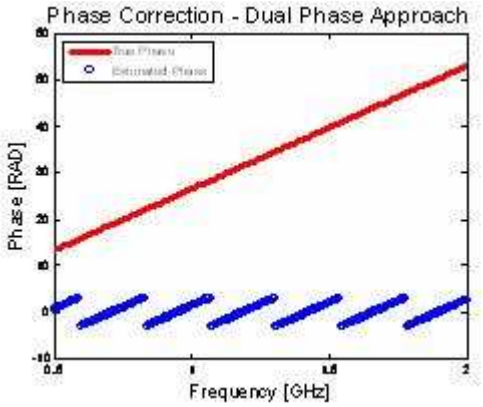

Figure 7.6: Estimated and True Phase

desired value is reached. Equation 7.12 shows the final form. Note that the R and Q values must be measured at each frequency and Equation 7.12 applied. This gives an estimated wall phase value at every required frequency.

$$\hat{\phi}(\omega) = arctan(\frac{Q(\omega)}{R(\omega)}) \tag{7.12}$$

Figure 7.6 shows the estimated phase for the three point scatterer simulation. The red line is the actual phase value at each frequency. The phase is linear because the wall in this simulation is homogeneous and non-dispersive. The phase ramp is due to the linearly increasing frequency. The advantage of this approach is that, were the wall dispersive (meaning that the phase changed non-linearly in frequency), the required phase at each frequency would be sufficiently determined.

The blue wrapping phase is the estimated value. The wrapping occurs because the range of the arctangent function cannot determine the phase outside of the $-\pi$ to π interval. However, mathematically, it is not necessary to determine the true phase. Only the value within this range is required to affect the necessary phase corrections in the image processor. Figure 7.9 & 7.10 shows the resulting image after the correction. Note that the three points have been successfully focused.

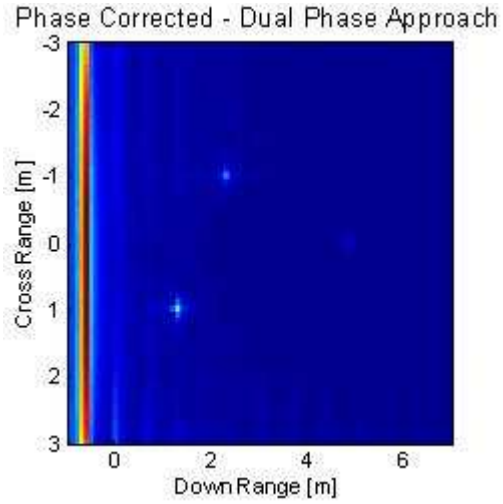

Figure 7.7: Image After Correction with Dual Phase Approach

Dual Frequency Approach

The dual phase approach makes an assumption that may not be practically achievable. This is the assumption that the return from the front of the wall has been removed (i.e. canceled). Because of this a second approach is introduced here. Some assumptions must also be made for this method. Two frequencies will be used to generate a set of non-linear equations that will be solved iteratively using a non-linear, successive approximation method. The assumptions here are that the reflection coefficients remain constant for the two frequencies. Since these values are slowly varying in frequency, this assumption is very nearly true. As long as the frequencies do not get too far apart, this assumption will hold.

Our starting point is with the quadrature measurements R and Q at two frequencies f_1 and f_2. The reason for using quadrature is that the a_0 unknown is naturally removed during the demodulation process. If we also consider the in-phase measurements, we have to solve for the added a_0 unknown. Since a_0 and a_1 are nuisance parameters, we utilize only q_1 and q_2. The expressions for these measurements are given by Equations 7.13-7.16. These are rewritten in the form of functions F_1, F_2 for use in the Jacobian matrix described next.

$$q_1 = \frac{a_1}{2} sin(\phi_1) \tag{7.13}$$

$$q_2 = \frac{a_1}{2} sin(\phi_2) \tag{7.14}$$

$$F_1(\mathbf{x}) = \frac{x_1}{2} sin(\frac{4\pi f_1}{c} x_2) \tag{7.15}$$

$$F_2(\mathbf{x}) = \frac{x_1}{2} sin(\frac{4\pi f_2}{c} x_2) \tag{7.16}$$

$$J = \begin{bmatrix} \frac{\delta F_1(x)}{\delta x_1} & \frac{\delta F_1(x)}{\delta x_2} \\ \frac{\delta F_2(x)}{\delta x_1} & \frac{\delta F_2(x)}{\delta x_2} \end{bmatrix} = \begin{bmatrix} \frac{1}{2} sin(\frac{4\pi f_1}{c} x_2) & \frac{x_1}{2} sin(\frac{4\pi f_1}{c} x_2) \frac{4pi f_1}{c} \\ \frac{1}{2} sin(\frac{4\pi f_2}{c} x_2) & \frac{x_1}{2} sin(\frac{4\pi f_1}{c} x_2) \frac{4\pi f_2}{c} \end{bmatrix} \tag{7.17}$$

The parameter x_1 is the reflection coefficient from the back of the wall. The parameter x_2 is the thickness-permittivity-squareroot product. The x_2 parameter is of primary interest. Knowledge of this value allows for the phase distortion to be corrected.

Define the two element vectors q and F by contacting the two respective terms in Equations 7.13-7.16. The problem of estimating the parameters x_1 and x_2 can be formulated as a non-linear least squares problem, $min_x(|q - F(x)|^2)$, equivalent to maximum likelihood under an additive Gaussian noise model $q = F(x) + noise$. Starting with an initial value of x_1,x_2, we can find the least squares solution using the iterative Newton-Raphson approach. This algorithm uses successive approximations to iterate to a solution. The Jacobian matrix shown in Equation 7.17 is determined using the non-linear equations F_1,F_2.

The Jacobian matrix defines a hyper-plane that is tangent to the manifold of the F_1,F_2

functions at the point of the current estimates of x_1,x_2. A solution to the equations is found within this plane and this solution will be closer to the true answer than the previous estimates. The same is true for the next solution until the estimates no longer change. This is the successive approximation strategy. Mathematically, this can be written as in Equations 7.18 - 7.21.

$$\hat{\mathrm{x}}_k = \hat{x}_{k-1} + (J_{k-1}^T J_{k-1})^{-1} J_{k-1}^T (\mathrm{q} - \mathrm{E}(\hat{\mathrm{x}}_{k-1})) \tag{7.18}$$

$$\mathrm{q} = \begin{bmatrix} q_1 \\ q_2 \end{bmatrix} \tag{7.19}$$

$$\mathrm{x} = \begin{bmatrix} x_1 \\ x_2 \end{bmatrix} \tag{7.20}$$

$$\mathrm{E}(\mathrm{x}) = \begin{bmatrix} F_1(\mathrm{x}) \\ F_2(\mathrm{x}) \end{bmatrix} \tag{7.21}$$

A logical starting point is to choose the initial values of x_1,x_2 to determined by the values we expect (i.e., the mean values) for the wall being interrogated. This incorporates the a priori information we have about the wall. For this simulation only a few iterations are required for the estimates to converge. Figure 7.8 shows the convergence in the x_1 parameter while Figure 7.9 shows the same for x_2. The starting values were 0.8 for x_1 and 0.6 for x_2. The actual values were 1.0 and 0.6325 respectively. The estimated values reached by the algorithm were 1.3 and 0.6270.

The x_2 parameter corresponds to the product, which is the key element in the unknown phase experienced by the waves traveling through the wall. Once this parameter is

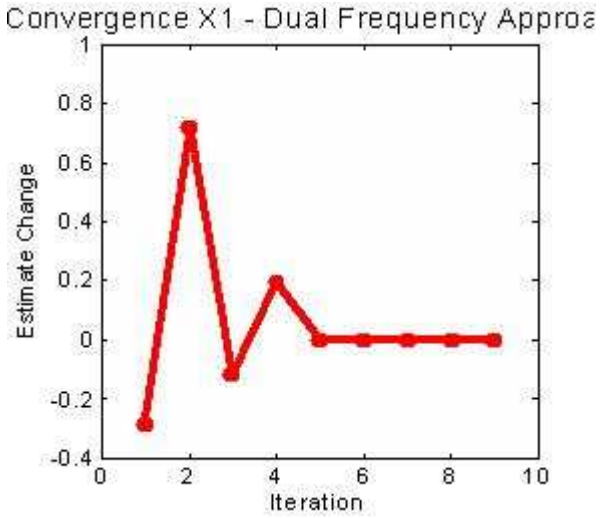

Figure 7.8: Convergence of Parameter x_1

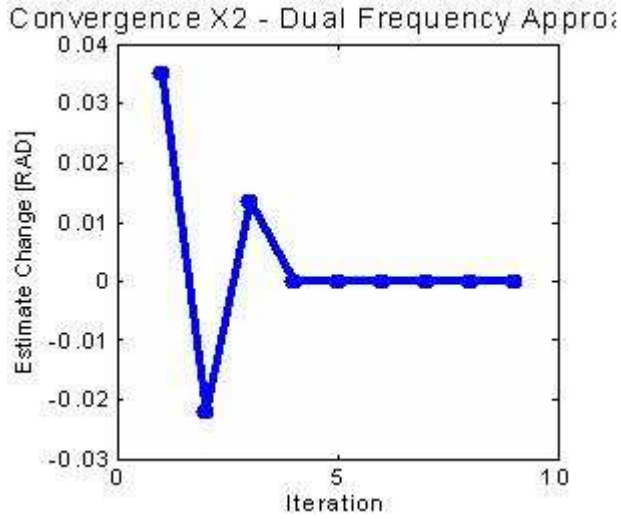

Figure 7.9: Convergence of Parameter x_2

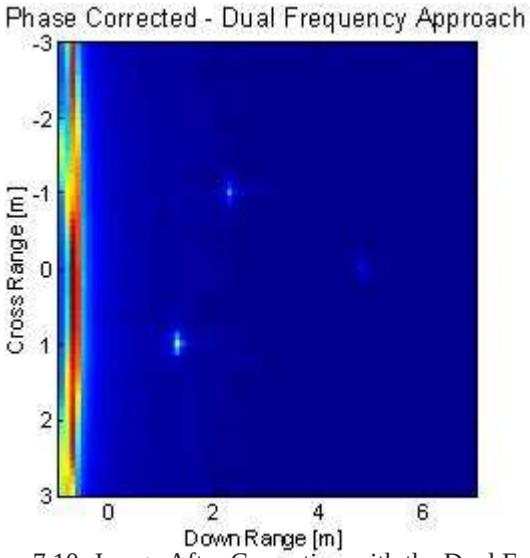

Figure 7.10: Image After Correction with the Dual Frequency Approach

estimated, the image can be phase corrected at any frequency. So, provided that the wall structure does not change, only one sounding has to be made in the dual frequency approach. The resulting image is shown in Figure 7.10.

Note that the three point scatterers are well focused in Figure 7.10. The dual frequency method shows much promise. Unfortunately, it does have challenges to be addressed in future work, namely local minima of the objective function $\|q - F(x)\|^2$ [75].

7.2.3 Outer Wall Conclusion

Two approaches have been proposed for determining the unknown phase produced by plane waves propagating through a wall. It has been shown that this unknown phase prevents proper imaging of the scene behind the wall using a See-Through-The-Wall radar. Both approaches were effective in determining and removing the unknown phase when their underlying assumptions were satisfied.

The two approaches were also quite robust when contaminated with noise. Both functioned well at a signal-to-noise (SNR) of -10dB. (SNR here is defined as the mean squared amplitude of transmitted sinusoid to the variance of the noise.) This robustness is due to the correlating of the return signal with the transmit signal. Each pulse was sampled

in such a way that 1000 points were collected. When all these samples are correlated with the signal and averaged together, a reduction in noise variance of a 1000 is affected.

7.3 The Inner Wall Problem

One of the goals of STW radar is to generate a layout map of the interior of buildings. When the radar frequency is sufficiently high methods like Method of Moments and Finite Element become intractable. Here we propose the use of scattering center models of objects like dihedrals, tophats, cylinders, and spheres as an approximate method for simulating radar response. These scattering primitives can be associated with the objects in the scene. By identifying the primitives, a layout of the building interior can be generated.

The contribution of this section is in the area of inner wall mapping. Others have looked at the problem of determining the characteristics of the outer wall [76] [77] . A great body of research exists on the identification of objects found in synthetic aperture radar imagery [78] [79] [80] . The issue of dealing with and mapping inner walls is a problem unique to STW radar imaging. The approach taken here is to look at the inner walls as dihedral scattering primitives. Dihedrals have a ”two bounce” characteristic that can be identified using polarimetric radar. This approach has been explored in the area of Foliage Penetrating Radar [3] [81] [2] for discriminating trucks from trees.

7.3.1 Inner Wall Simulation

Simulations of radar imagery are employed throughout this study. A building scene contains several basic components: 1) an outer wall, 2) a set of inner walls, and 3) a collection of objects. Of particular interest is the existence of any weapons stored inside inner rooms.

Note that the scene of Figure 7.16 is sparse. This means there is a lot of empty space. A Method of Moments (MoM) approach to modeling this scene might appear to be a good starting point. The MoM approach only deals with the scattering objects within the scene.

Other approaches like Finite Difference Time Domain (FDTD) and Finite Element Method (FEM) will ”grid up” all pixels including the empty space. The rule of thumb in all E&M modeling applications is for the discretization to have ten samples across the shortest wavelength. The building here is 10m x 10m in dimension. At 5GHz this translates to 1.3 million elements in the outer wall (considering only the integrals over the surfaces) and 300 thousand elements in the inner walls, which are 3m long. Inverting a matrix of this size to solve for surface currents would require powerful computing. As an alternative to large numerical simulations, we make several simplifying assumptions. The primary assumption is that a enhanced geometrical optics approach is sufficient.

EGO is discussed in Section VII. It assumes that propagating waves can be modeled as plane waves. In this STTW application the outer walls are modeled using Fresnel reflection and transmission coefficients. This implies that the wall is large and homogenous. The physics of the corners are not truly captured. For cases where the corners are not within the footprint of the antenna beam, this assumption should be adequate. In addition, the walls are considered to have no windows, doors, or other openings. The outer walls are assumed to be reasonably thick - on the order of 0.2m.

The inner walls are simulated using the scattering center approach. A dihedral is formed by the connection between the wall and the floor. The primary goal of this work is to determine the inner structure of the building. This means identifying inner walls and separating them from other objects to form a $building\ model$ from the gathered data. Modeling the inner walls as dihedral scattering objects will not provide a high fidelity prediction of scattered fields. It will, however, capture the polarimetric characteristic of the wall’s response. This will allow for testing of polarimetry based algorithms for identifying the inner walls. The assumption that the inner walls can be modeled as dihedral scattering centers should be adequate for thin inner walls. This means that the radar wave passing through the wall will experience little phase delay and little attenuation due to the inner wall.

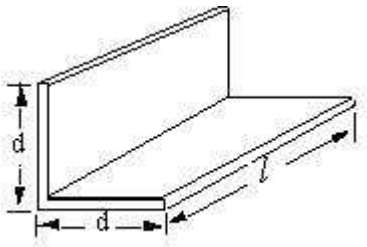

Figure 7.11: Dihedral Scattering Center

Objects within the scene are considered to be point scatterers with varying scattering cross sections. For simplicity, the objects are simulated as constellations of points. All objects within the scene represent potential objects of interest. The goal here is to classify the outer walls, inner walls, and scene objects. In future work the scene objects can be further processed to identify the object class.

Using the scattering center approach, Figures 7.12 and 7.13 were generated. These are produced by illuminating the scene of Figure 7.16 from the bottom (Figure 7.12) and from the left (Figure 7.13). The simulated radar has a bandwidth of 1GHz about a center frequency of 4.5GHz. This frequency is relatively high compared to most existing surface penetrating radar systems. The frequency range was chosen to lend validity to the EGO assumptions underlying these simulations. The beamwidth of the antenna is 90^o in both cross range directions, this beamwidth is intended to match a man portable (hand held) antenna. Likewise, the stand-off distance is 10m corresponding to a system taking measurements from a nearby road.

Several noteworthy items can be seen in these simulations. First of all, the inner walls parallel to the radar line-of-sight tend to vanish. This occurs in spite of the large beamwidth of the antenna. At the wavelengths used in these simulations, there is not much direct backscatter from the inner walls when they are not perpendicular to the radar's line-of-sight. The perpendicular walls do have a small response. These are the edge

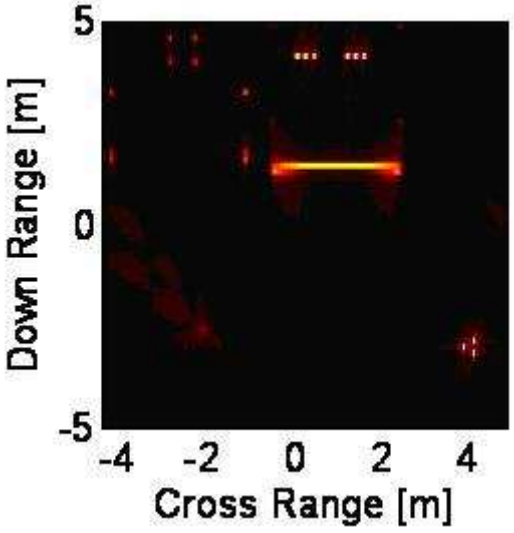

Figure 7.12: Inner Wall Simulation - Bottom Illumination

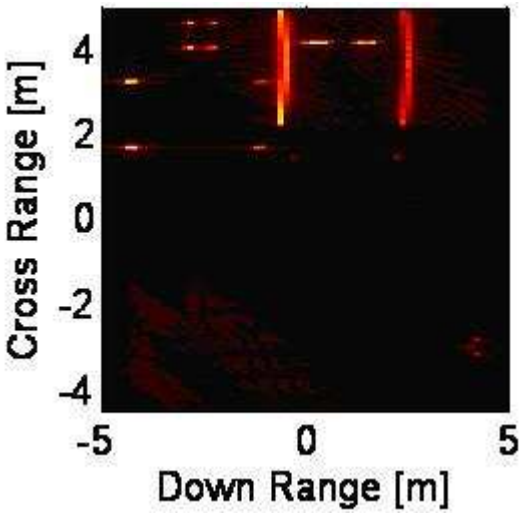

Figure 7.13: Inner Wall Simulation - Left Illumination

diffraction effects (slightly visible) at the edges of the dihedral. Looking at the simulated sink, the reflectance of objects appears to change between the two images. This is due to the spherical spreading of the power emitted by the radar. In Figure 7.12, the illumination is from the bottom. In Figure 7.13, it is from the left. The radar is physically closer to the sink in the bottom illumination. Since the imaging algorithm does not attempt to correct for spherical spreading, the reflectance appears to become weaker in the left illuminated scene.

7.3.2 Layout Mapping

The goal of this work is to determine a $Building\ Model$ from observed imagery. This is similar to a Computer Aided Design (CAD) drawing of the building. This drawing captures the internal layout. To create this product, it is necessary to identify the outer walls, inner walls, and scene objects. These are then stored to the $Building\ Model$ file as objects. To ensure that all inner walls are captured, it is necessary to scan the building from two directions - bottom and left. This insures that all inner walls will be illuminated by the radar beam.

A simple approach to detecting inner walls is to take advantage of the dihedral-like response that is formed by the intersection of the walls with the ground. Polarimetrically, we expect the phase angle of the VV to HH ratio to be 180 for dihedrals. This occurs because the VV polarized wave sees a 180 phase shift while the HH polarization does not have a corresponding phase shift. This fact can be exploited to help map the inner walls of the structure.

Figures 7.14 and 7.15 show the result of applying a simple dihedral scattering center detector. This detector takes a ratio of the VV and HH complex images and finds the pixels with a phase close to 180. The resulting pixel maps correspond to the inner walls. These regions can then be modeled as inner walls in the $Building\ Model$.

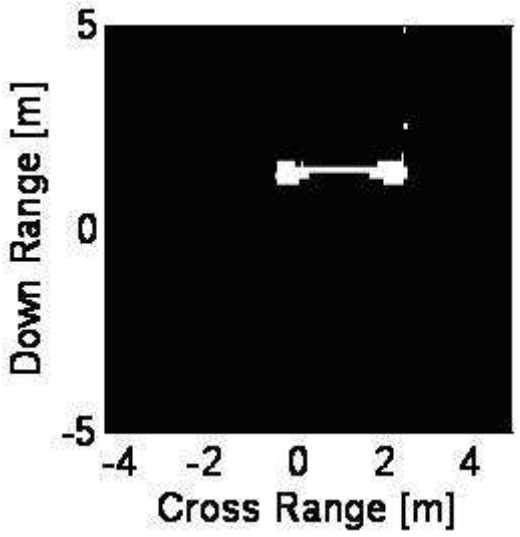

Figure 7.14: Detected Inner Walls - Bottom Illumination

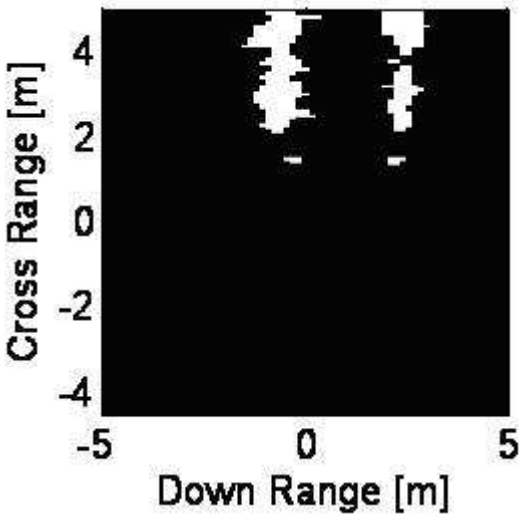

Figure 7.15: Detected Inner Walls - Left Illumination

7.3.3 Inner Wall Conclusion

This section explored the issue of simulating building penetrating radar with a focus on inner wall detection. The simulations were conducted in a frequency range where EGO was expected to dominate. The resulting simulated images were used to propose an inner wall detection and mapping algorithm. The algorithm utilizes polarimetric scattering characteristics to classify pixels as part of the inner walls. Encouraging preliminary results are presented.

7.4 I.R.I.S. Adaptive Imaging

See-through-the-Wall Radar Imaging is an emerging technology useful to both Homeland Security and Law Enforcement. The goal is to provide an imaging tool that gives authorities information. The nature of this information includes the internal layout of a building (location of doors, obstructions, or inner rooms), the existence and location of objects of interest(weapons, methamphetamine labs), and the tracking of suspicious individuals inside. This application is challenging because it requires the processing and interpretation of electromagnetic waves in an inhomogenous media with unknown material parameters and structures. To provide the optimal measurement, it is desired to adapt the observations to a location and/or frequency range that will provide the most powerful information. The proposed approach makes use of a ”virtual transmitter”. The fields observable from the virtual transmitter are predicted from a ”building model” that is determined from previous observations. By reciprocity, the fields observed on the outside of the building reflect the fields that can penetrate the building from that outside location to illuminate the location of interest. Because the building model must be built up (learned) over the course of several measurements, the algorithm is iterative. An interesting location within the building is determined after the first measurement. An initial building model is produced form this observation, the virtual transmitter is placed, and the fields outside the building are predicted using numerical electromagnetic models. After each observation,

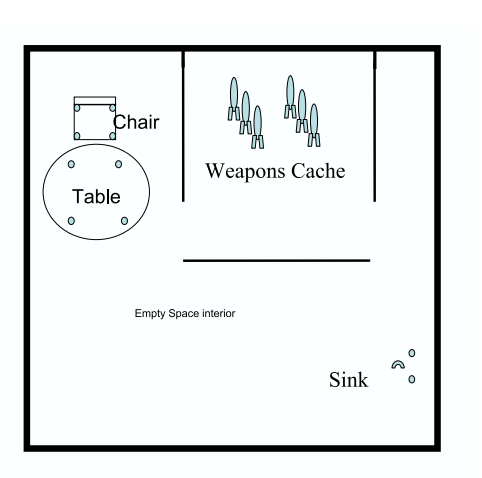

Figure 7.16: 2D scenario used to illustrate the IRIS approach. Room is 10×10 meters and a SAR sensor with 1 meter baseline can be placed at any position parallel to top or bottom walls at exterior of building.

more information is obtained about the building and the building model is updated. This may lead to a new placement of the sensor for the next observation. It may also lead to new locations of interest that should be interrogated by the imaging sensor.

Assume an initial sensor/illuminator configuration has been deployed and that an image has been reconstructed along with its confidence map using the iterative Bayesian algorithm described in Sec. II. The objective of IRIS is to find a new sensor configuration that will allow us to improve upon the initial reconstructed image. For concreteness, we focus on imaging the interior of a building and assume that the space of possible configurations are locations where the baseline of a small SAR sensor could be placed at the building exterior (see Fig. 7.16). The proposed IRIS approach uses the confidence map to identify regions of the image that were poorly resolved, i.e., pixels that have poor confidence values ($P(x_i = 0|Y)$ near 0.5). It then simulates the RF field at the building exterior that would be created by placing a (virtual) transmitter in one of the poor confidence regions of interest. From this simulated field we can extract information about the best location to redeploy the illumination/sensing platform.

For this purpose we define the predicted information gain as a measure of how much a given sensor position might enhance the ability to detect the presence or absence of a scatterer in the vicinity of the virtual transmitter. The value of redeploying the sensor

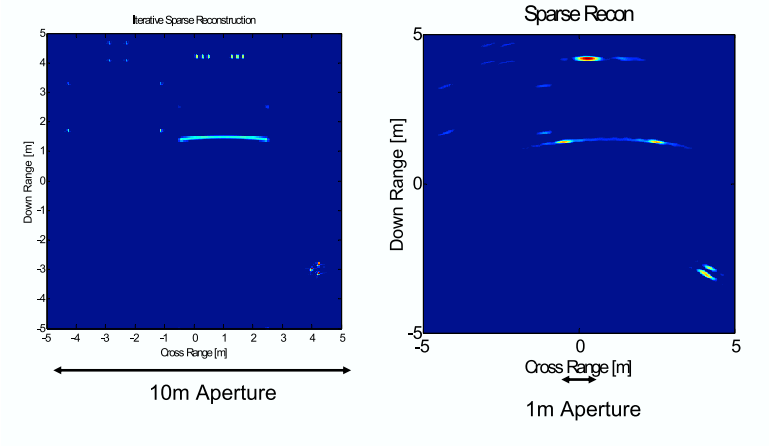

Figure 7.17: Iterative reconstruction of building interior illustrated in Fig. 7.16 after 10 iterations and a full 10 meter baseline (left) and 1 meter baseline (right) monostatic SAR illuminator/sensor.

at a particular location can be measured by the variation of the RF field at that location produced by perturbing the location of the virtual transmitter. Define the energy frequency spectrum $E_{x,y}(\omega)$ of the RF field measured at location y due to an omnidirectional transmitter placed at location x, and for a location x_k define $E_k = E_{x_k,y}$. The spectral variation produced by perturbing the location x from a reference location x_1 to a new location x_2 can be measured by the Kullback-Liebler (KL) divergence

$$D(E_1 \| E_2) = \int E_1(\omega) \log \left(\frac{E_1(\omega)}{E_2(\omega)} \right) d\omega.$$

The KL divergence and its generalizations have been used by many authors in sensor management problems and are often referred to as the information gain [43] [82] [83]. We define the information gain at sensor position y as the sum of the KL divergences of the RF fields produced by cross-range perturbation $x_1 \rightarrow x_2$ and range perturbation $x_1 \rightarrow x_3$ of the virtual transmitter location:

$$\overline{\mathrm{IG}}(x, y) = D(E_1 \| E_2) + D(E_1 \| E_3). \tag{7.22}$$

When viewed as a function of y this quantity sweeps out the information gain field.

7.4.1 Numerical Simulation

We consider a scenario illustrated in Fig. 7.16. A weapons cache is hidden in a room surrounded by four exterior walls and obscured by other interior walls and objects in the room. A mono-static radar can be placed anywhere above the top wall or below the bottom wall. The room is enclosed by a 10×10 meter wall that is 1/3 meter thick. We evaluate the performance of a short baseline (1 meter) SAR sensor that can be placed at any position along the 10 meters of the top or bottom wall at 1 meter standoff distance. The operating frequency of the simulated radar was 4.0GHz to 5.0GHz and the SAR radar baseline was sampled at 10 points (every 10cm) along its 1 meter extent. The simulator modeled each object on the room with a simple superposition of scatterers using physical optics. We assume that the external wall attenuation and phase parameters are accurately estimated, e.g using the method of [76].

For an initial sensor position centered at the middle of the lower wall the two panels of Fig. 7.17 show the results of applying ten iterations of the Bayesian iterative reconstruction algorithm (6.30) with sparseness prior (6.29). The values of a, w and σ were fixed during the entire experiment. The right panel of the figure is significantly lower resolution than the left panel due to its relatively smaller baseline of 1 meter. The left panel is the reconstruction obtained after the first iteration of the IRIS procedure.

The probability map $P(x_i = 0|Y)$ and the associated entropy map $-\log P(x_i = 0) - \log P(x_i = 1)$ are shown in Fig. 7.18. The entropy map is maximum for reconstructed pixels whose *a posteriori* probability of being empty space is close to 1/2. The entropy map therefore measures the *a posteriori* (lack of) confidence in the value of that pixel and is called the "confidence map" of the image. From the confidence map a region of low confidence is identified, e.g., the region near the top of the image, and a virtual emitter is simulated in this region to generate an information gain field for determining the best redeployment configuration for the next iteration of IRIS.

The construction of the information gain field is illustrated in Fig. 7.19 for the scenario

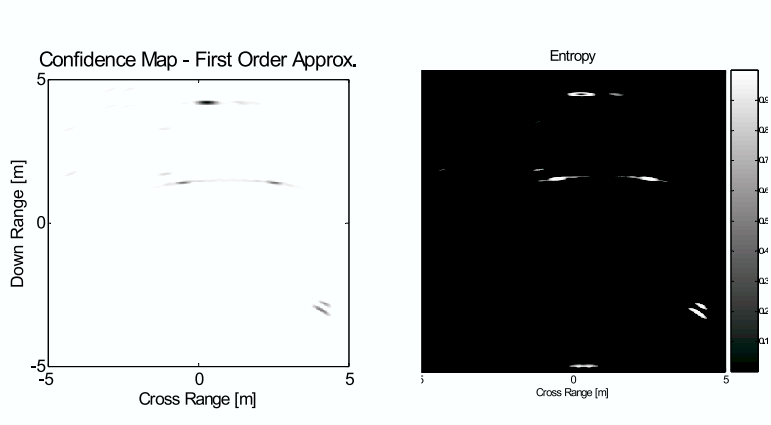

Figure 7.18: Confidence Map (left) and Entropy Map (right) associated with the 1 meter baseline image reconstruction shown in Fig. 7.17.

illustrated in Fig. 7.16 and a low confidence region region identified from Fig. 7.18. On the right of the figure is the frequency spectrum of the induced RF field at a candidate redeployment position at the exterior of the building for the three sensor positions illustrated in the left panel of the figure. The difference between the reference spectrum and the horizontally (cross-range) and vertically (range) perturbed spectra is measured via the information gain formula (7.22). On the left of Fig. 7.19 at the exterior of the building is the color coded field corresponding to the information gain. The distances of the range and cross-range perturbations of the virtual transmitter have been exaggerated for clarity of presentation; actual perturbations would produce less obvious visual differences in the RF spectra.

In Fig. 7.20 the virtual transmitter positions and induced information gain fields are illustrated for iteration 2 and 3 of the IRIS algorithm. Optimal information gain maximizing SAR positions are indicated by the 1 meter baseline white arrows at exterior of the building. After the third iteration of IRIS 4 different sensor positions will have been deployed (including the initial deployment).

On the right panel of Fig. 7.21 a composite of the four reconstructed images (including the final image) obtained from the three iterations of the adaptive IRIS algorithm described above. The recovered resolution using IRIS's total baseline of 4 meters is comparable to

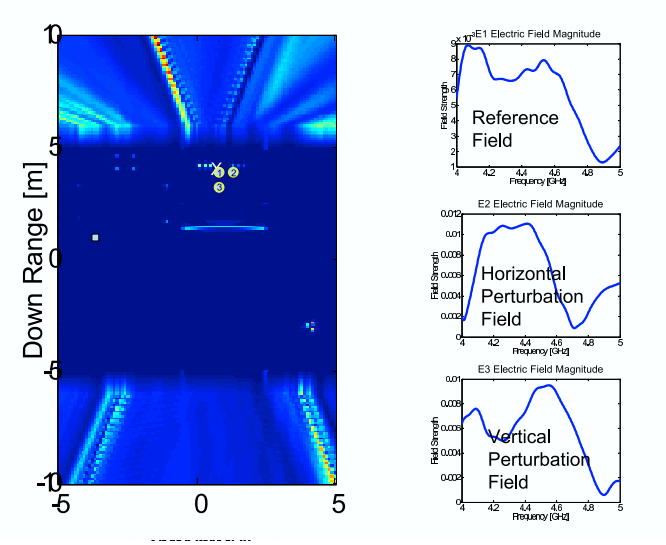

Figure 7.19: The information gain field is computed by simulating the variability of the RF spectrum that a virtual transmitter in the vicinity of a pixel of interest (circle 1 in left panel) would generate at different locations at the exterior of the building. At right are the induced RF fields generated by a virtual transmitter at the reference position (circle 1), cross-range (circle 2), and range (circle 3) perturbations.

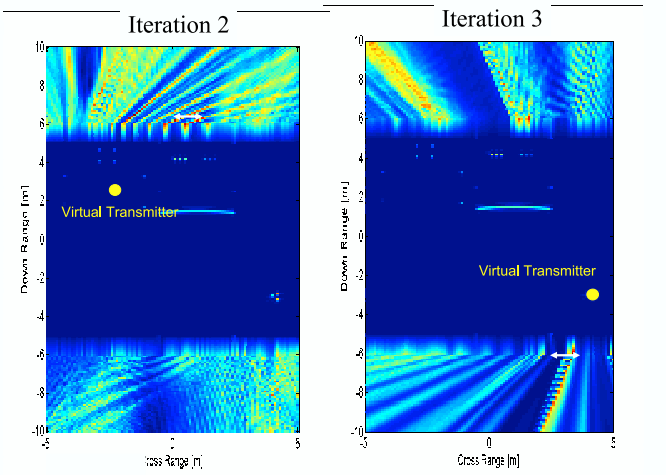

Figure 7.20: Virtual transmitter locations and the induced information gain fields for iteration 2 and 3 of IRIS for the scenario illustrated in Fig. 7.16.

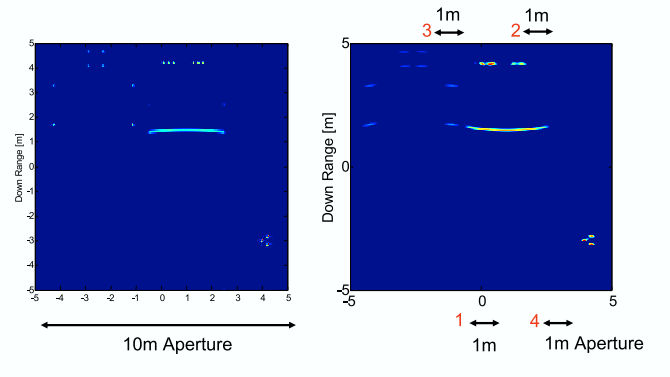

Figure 7.21: Comparison between final IRIS reconstruction after 4 iterations with 1 meter baseline SAR deployments (shown by black arrows) versus one shot IRIS reconstruction using 10 meter baseline. In both cases the reverse wavenumber migration model with EM implementation of MAP algorithm has been used.

the resolution of the non-adaptive one-shot 10 meter baseline shown on the left panel of the figure.

7.4.2 Convergence

The nature of STW radar reveals that objects within the scene have directional characteristics. While many objects are omni-directional, the scattering objects that compose the layout (that is the walls) are directional. Inner walls have narrow beam scattering patterns. This means that a radar must be nearly perpendicular to the wall to illuminate it. The illumination could come from either the “front” or the “back” side. Corners have a wider beam. In contrast to inner walls, however, they will only backscatter in one direction. Therefore, the radar must illuminate a corner from the proper side.

To insure complete detection of all scattering objects in a STW scene, a radar would need to illuminate the entire 360^o aperture. Figure 7.22 shows the simulated test scene imaged from full $10m$ apertures on all four sides. The IRIS algorithm seeks to detect all objects in the scene, while observing (much) less than the total 360^o.

Convergence in the context of the IRIS algorithm is the notion that the image being built adaptively will converge to the correct image. Since the algorithm is building the larger scene from observations of small regions of the scene, it can be argued that the final product will never truely to exactly the same as that observed by a larger aperture array.

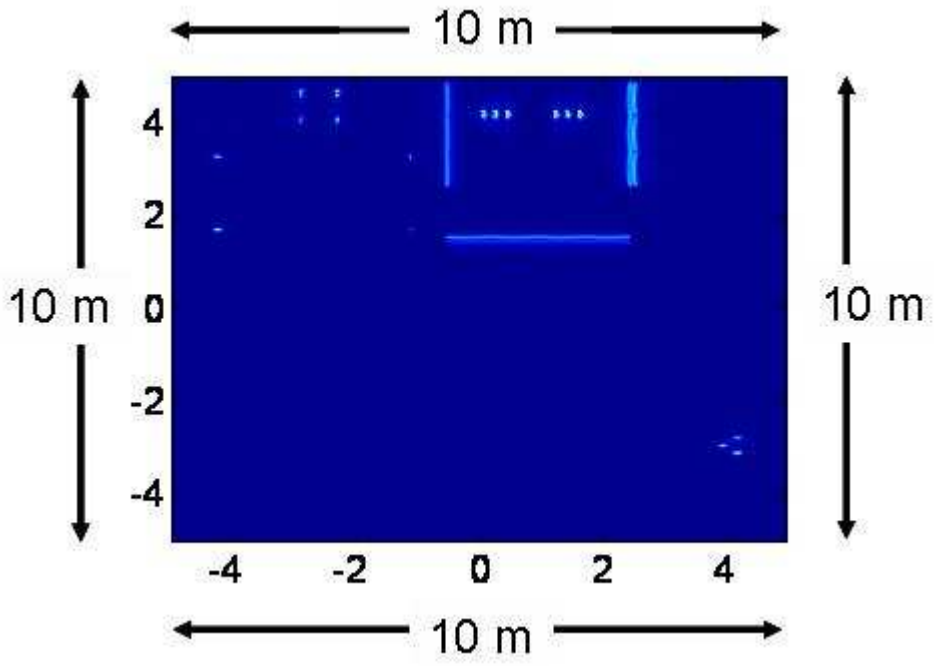

Figure 7.22: Image from 360^o Aperture

However, the fundamental information contained in the image can be the same. For this reason the quantity of interest in convergence is the "probability of detection" of the scene objects.

Figure 7.23 shows the image and the apertures used in the final version of the IRIS algorithm. All objects in the scene have been detected. Note that the inner walls are tricky. They have been detected by the $1m$ aperture deployments, but are only partially revealed. A way to overcome this is to use some other method to determine the wall layout. This could be through the deployment of an airborne asset that would collect the total 360^0 (or $40m$) aperture or by making use of floor plans (if available).

For a useful concept of operation, the IRIS process must come to a final product with less expense of resources (i.e. deployments, time, aperture used) than the full image. Figure 7.24 shows the convergence process. To compare apples to apples the probability of detection is plotted versus $totalaperture$ used. Here we use meters because Figure 7.22

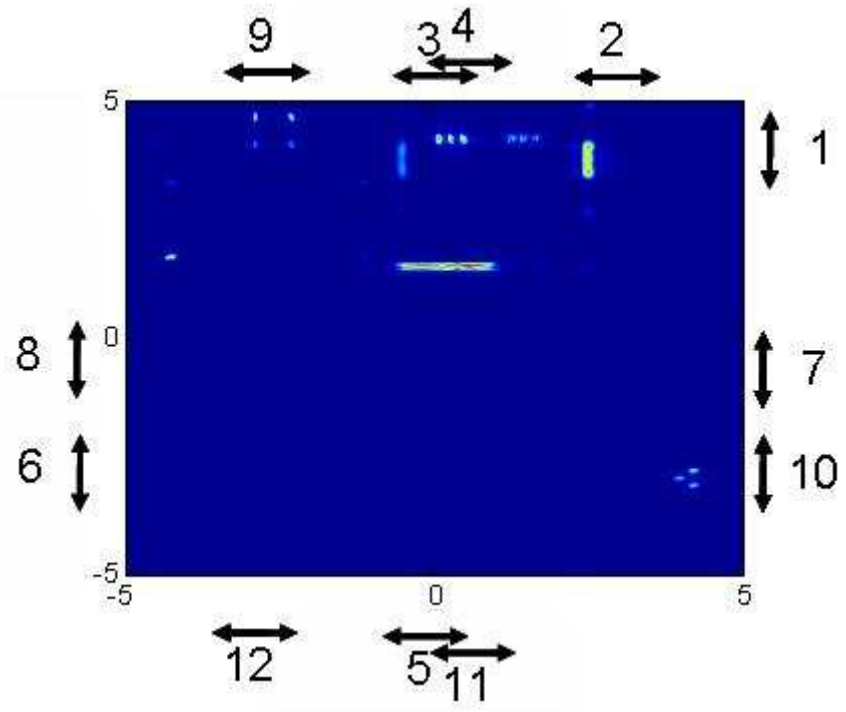

Figure 7.23: Image from IRIS

was produced from $40m$ of total synthetic aperture by observing the $10m$ per side scene from all four directions.

Notice that two stall points are observed at $3m$ and $8m$. These stalls are overcome by an approach inspired by Yuan & Lin [84]. The alogorithm senses that it has reached a stall and takes action to widen its search within the space of the scene. All objects are detected after ten deployments. Necessary confidence in the scene is satisfied after twelve deployments. Thus the IRIS converged in detection probability in $12m$ to produce Figure 7.23 rather than requiring the total $40m$ used in Figure 7.22.

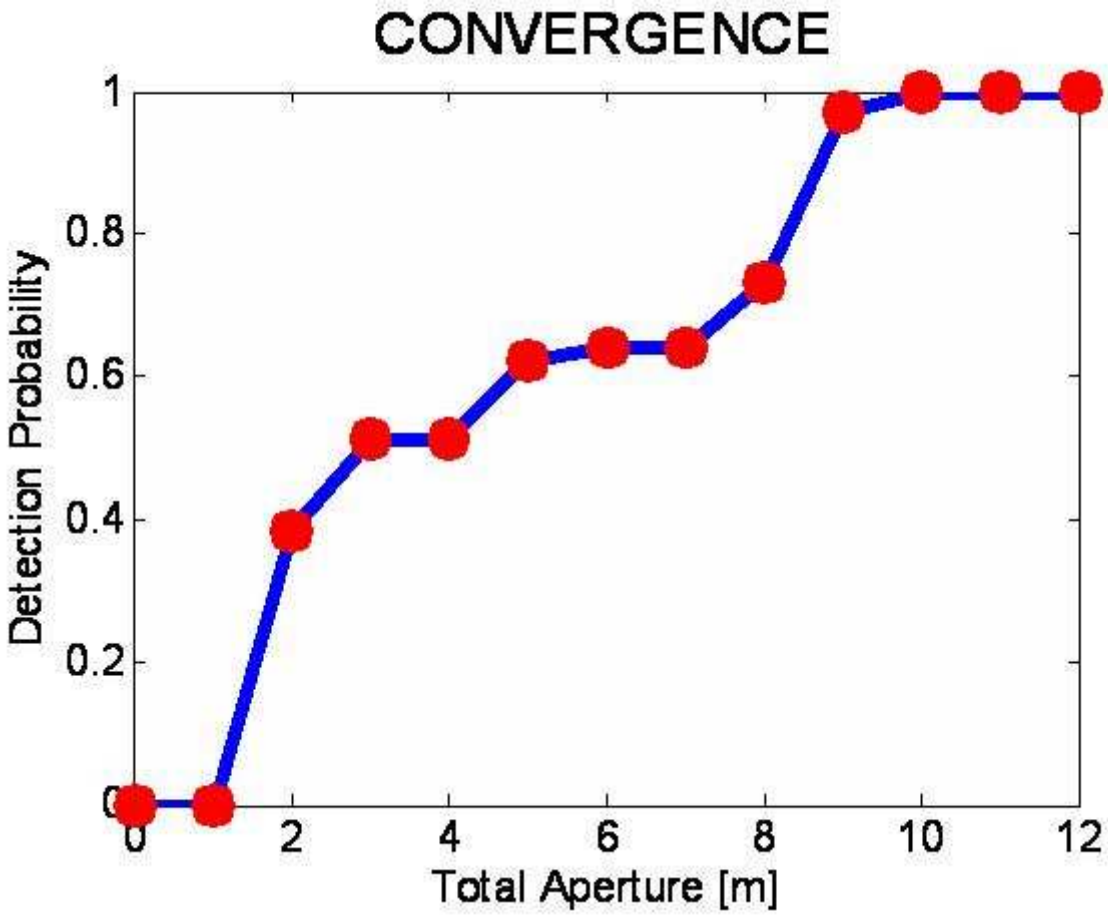

Figure 7.24: Convergence of Imaged Scene

CHAPTER VIII

CONCLUSION

8.1 Discussion of Results

This dissertation has addressed the problem of surface penetration with the goal of detecting objects of interest. The general problem is one of forming an image with an appropriate sensor, detecting points of interest within the image, and reporting objects of intetest while rejecting clutter objects. The two main applications explored in this work are landmine detection and surface penetrating radar imaging.

The first contribution chapter looks at non-statistical approaches to image understanding, signal-to-noise ratio enhancement, and object classification. First, computer vision techniques are used to segment a ground penetrating radar image into target and background regions. A bounding box around the signature is used to determine the object depth and size. Next, a novel approach to signal-to-noise ratio is introduced called the $hyperbola\ flattening\ transform$. This transform applies to ground penetrating radar signals, which have a hyperbolic point spread function. The transform helps to increase the depth of penetration of the landmine by collapsing all the energy in the signature into a point. The third approach applies basis projection operations to determine object depth and size using electromagnetic induction (EMI) metal detectors. By identifying bases derived from a magnetic dipole model of the scattered fields, a unique projection matrix is formed for objects of varying depths and three canonical shapes.

The second contribution looks at statistical approaches. Because of a strong correlation

between object depth, type, and sensor response, pixel classification can be performed. By modeling the response of two sensors (EMI and GPR) as a jointly distributed Gaussian mixture, the object type and depth can be determined by associating the pixel with a specific Gaussian component. Using a Bayesian Network to facilitate training of the joint probability density function is proposed and discussed. Statistical approaches are also used in sensor scheduling. An approach called $Active\ Sensing$ is used to determine the best single sensor to deploy from a set of six hypothesized sensors. It is shown by way of a confusion matrix that the deployment of a single confirmation sensor can increase the probability of correct classification of subsurface objects after detection of the objects using the Gaussian mixture approach. Last in this contribution area a reinforcement learning approach is explored for learning a policy that applies more than one sensor when needed to produce the highest probability of correct classification with the least number of sensor dwells.

The third contribution turns to imaging techniques. First, wavenumber migration is explored for its ability to produce 2D and 3D imaging at an accelerated rate compared to backpropagation techniques. The concept of image sparsity is introduced as a way of reducing image artifacts. The key to implementing sparsity is the ability to perform wavenumber migration $in\ reverse$. With this technique, introduced in this dissertation, Landweber iterations can quickly and efficiently transform data between observation and image domain. The final innovation of this work is applied to See-Through- Wall radar imaging. It is called the Iterative Redeployment of Illumination and Sensing (IRIS) algorithm. This technique is a novel way of approximating a large synthetic aperture radar system with multiple deployments of a much smaller array. The algorithm utilizes the scene itself to determine the best locations to acquire further observations for the given scene. E&M simulation tools dubbed $virtual\ transmitters$ are used to predict fields outside the scene of interest. The tools are limited to Geometrical Optics, but use an enchancement that corrects for phase distortions caused by the outer wall. An information

gain metric is computed on the predicted external fields to direct sensor placement.

8.2 Suggestions for Further Research

Two decades of surface penetrating technology have been applied to the problem of landmine detection and classification. Robotic arms are currently being implemented on tactical vehicles to assist in the probing of suspicious locations. An arm that could select a sensor of choice as directed by a sensor scheduling algorithm could result in high rewards of accelerated performance. Such a device could especially reduce the impact of interrogating non-threatening (false-alarm) objects.

The IRIS algorithm is composed of multiple subcomponents: 1) uncertainty map, 2) sensor information map, 3) virtual transmitter, 4) sensor observations, and 5) imaging. Each of these subcomponents is a potential field of research. For example, the imaging approach used in this work drew upon the principle of image sparsity to control Landweber iterations. Other mechanisms may exist that optimize various other prior information. Also, the virtual transmitter here used compact models (Enhanced Geometrical Optics) to simulate electromagnetic propagation through walls. A more accurate (and more time/memory consuming) approach would be to use advanced numerical simulations (MoM, FEM, FDTD) to give a high fidelity prediction to the external electric fields.

The utlimate goal in STW imaging is to create 3D volumetric images of entire buildings. To accomplish this, high performance parallel computing will be required. Parallel programming in conjunction with the fast and efficient imaging techniques used in wavenumber migration could achieve a 3D result in a reasonable amount of time. These techniques could also be utilized in 3D imaging of landmines. To date the Landweber iterations using wavenumber migration approximations have been applied in “2.5”D. That is, the algorithms have been implemented in 2D and applied to 3D data in slices. A full 3D implementation of the algorithm is easily generalized and an excellent goal for future research.

APPENDICES

APPENDIX A

ELECTROMAGNETIC INDUCTION (EMI) SENSORS

Metal detectors remain a useful tool for detecting buried metal objects. Fundamentally they consist of a coil of wire that is driven by electric current. This current forms a magnetic field that couples to the buried object. In response the object creates a secondary magnetic field that can be sensed at the surface. This process gives this family of sensors the name Electromagnetic Induction (EMI) sensors.

The primary challenge of these systems is separating the field they generate - called the primary field - from the object's response - called the secondary field. In this section we study a typical EMI sensor called the EM61. This sensor operates in the time domain. It generates pulses to create the primary field and measures the secondary field while the primary field is off. Section A.1 describes the time response of the system. It shows how the time decaying signal can be used to identify the object's metal content. Section A.5 describes the expected spatial signal formed by scanning over the object. Section 3.3.1 describes how to extract shape information from the spatial signal.

A.1 EMI System Overview

The EM61 is the property of Geonics LTD of Toronto, Ontario. It is a man portable metal detector capable of measuring mV changes in sensor response, and is shown in Figure A.1. The device consists of a wire loop transmitter and two receiver coils mounted on wheels to form a rolling platform. The main receiver is co-located with the transmitter while the secondary receiver is 40 cm above it.

Figure A.1: The EM61 Metal Detector

The transmitter is continuously pulsed with current, which causes a primary magnetic field to be emitted. This field induces swirling currents (called eddy currents) in the ground below the device. If a target is present, the eddy currents in the metal will continue to flow for a short time after the primary field pulse is shut off. This forms a secondary magnetic field that can be detected at the surface. The receivers sample and store the secondary field during a small time window in between transmitter pulses. This insures that the secondary field is not drowned out by the primary.

To operate the device over a survey area, the operator manually ”raster scans” the area. That is the device is pulled back and forth across the area until it has been completely covered. Samples are taken after each pulse of the transmitter. However, a counter on one of the wheels triggers the receivers’ control electronics to average all samples received since the last count. This is done to reduce noise. Thus, the slower an area is scanned, the more samples over a single position will be averaged. Post test software maps the samples into an image by utilizing along track positions recorded from the wheel counter and from operator knowledge of the separation between scan lines.

A.2 Transmitter Waveform

One of the complications of designing an active metal detector is that the primary field tends to overwhelm the secondary field produced by the target. This is due to the receivers

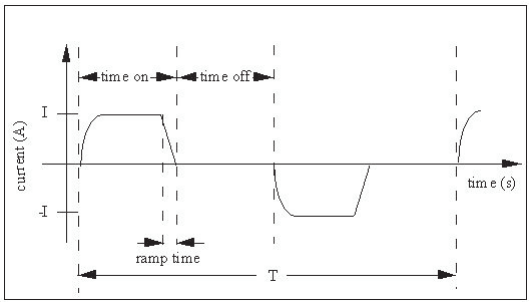

Figure A.2: Transmitter Current Waveform

being closer to the transmitter than they are to the target, as well as, the high power necessary to produce a desired penetration depth. To prevent the primary field from overwhelming the secondary field, the transmitter current is forced to zero as quickly as possible on the trailing edge of the pulse and a sample of the secondary field is taken at a time when the primary field has vanished. This technique is called time domain electromagnetics (TDEM). (It is also referred to as eddy current analysis [85] in the field of nondestructive evaluation.) Figure A.2 is a diagram of one period of the current waveform that excites the transmitter. It is referred to as a "bipolar square wave with 50% duty cycle".

For the purpose of modeling the system's operation, it is assumed that the transmitter can be modeled as a vertical magnetic dipole. This is somewhat of a loose assumption since the transmitter is a 1m x 1m square coil. However, investigation of experimental data shows that this assumption is reasonable. Also, the ramp times are considered negligible. What is important is the frequency at which the waveform in Figure A.2 operates and the transmitter's magnetic moment. Most models of the EM61 operate at a frequency of 75.0 Hz (period: $T = 13.3ms$). The magnetic moment, m_{0z}, is given by $m_{0z} = NIA$, where N is the number of turns in the coil, I is the magnitude of the current pulse, and A is the area of the transmitter coil. The value of the magnetic moment for this instrument is $190Am^2$.

The transmitter waveform can be expanded in a fourier series that is composed of a component at $75Hz$ and its odd harmonics (i.e. $225, 375, 525Hz$, etc.) [86]. In Section A.4 it will be shown that the receiver filters out all frequencies but the $75Hz$ fundamental. So for the purpose of modeling, the transmitter is assumed to be a vertical magnetic dipole

at $75Hz$ with a dipole strength of $190Am^2$.

A.3 Response of a Spherical Target

Many simplifying assumptions are used to approximate the response of a buried target to the primary magnetic field. The approach outlined here is a summary of the research conducted by Y.Guo, which is documented in a Johns Hopkins University/Applied Physics Laboratory technical note [87].

It has already been assumed that the transmitter is a magnetic dipole. Another assumption is that the target is a solid, metallic sphere buried in a conducting half space with a homogeneous conductivity. The problem of quantitatively determining the secondary field produced by the sphere is found in an article by Hill and Wait [88]. Their approach is to determine the magnetic field at the center of the spherical target with the target removed. This is called the unperturbed field. This field is decomposed into vertical and radial components that induce magnetic dipoles in the sphere. The expressions relating the unperturbed magnetic field to the vertical and radial induced dipoles are:

$$m_z = -2\pi a^3 P(\omega, \mu_s, \sigma_s, a) H_{0z}(x_s, y_s, z_s) \tag{A.1}$$

$$m_r = -2\pi a^3 P(\omega, \mu_s, \sigma_s, a) H_{0r}(x_s, y_s, z_s) \tag{A.2}$$

$$P(\omega, \mu_s, \sigma_s, a) = -\frac{2\mu_s (\sinh\alpha - \alpha\cosh\alpha) + \mu_0 (\sinh\alpha - \alpha\cosh\alpha + \alpha^2 \sinh\alpha)}{\mu_s (\sinh\alpha - \alpha\cosh\alpha) - \mu_0 (\sinh\alpha - \alpha\cosh\alpha + \alpha^2 \sinh\alpha)} \tag{A.3}$$

$$\alpha = (i\omega\mu_s\sigma_s)^{\frac{1}{2}}\, a \tag{A.4}$$

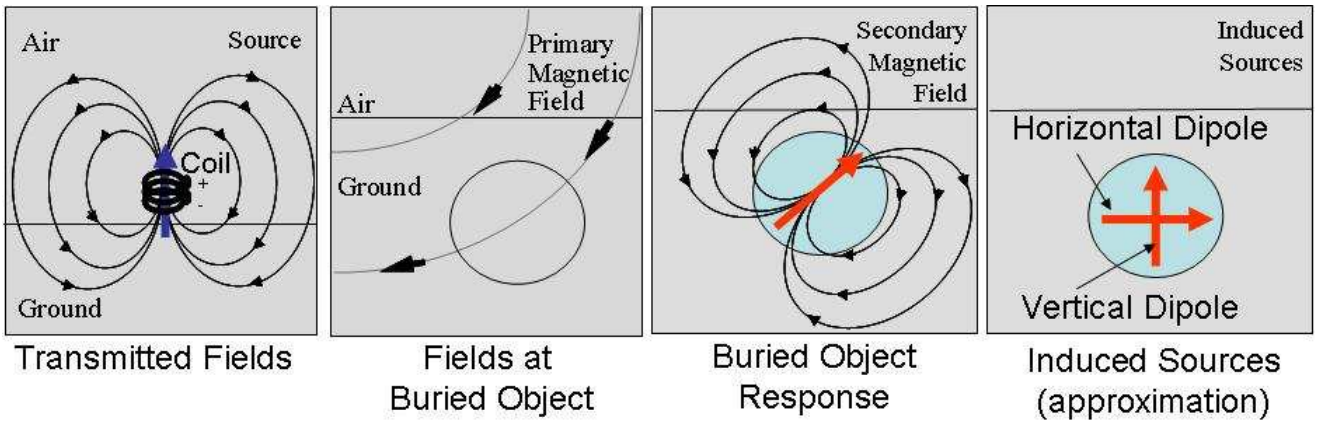

Figure A.3: Phenomenology of Induced Dipole Sources

The target parameters are: a the radius, μ_s and σ_s the magnetic permeability and electric conductivity, (x_s, y_s, z_s) the target's center of mass position with respect to the transmitter. ω is the transmitter frequency and μ_0 is the permeability of free space. The function P is called the polarizability. Note that this factor is the same for both the vertical and radial induced dipoles. This is because the target is a sphere (i.e. all directions are equally polarizable). Figure A.3 illustrates the induction of horizontal and radial dipoles by a vertical magnetic dipole transmitter.

Once the response dipoles have been induced, the secondary fields at the surface are determined by the standard equations for the magnetic field due to a magnetic dipole buried in an infinite conducting half-space. These expressions and the expression for the unperturbed field can be found in [33]. Qualitatively, the fields of the induced dipoles are shown in A.3.

The magnetic field measured at the surface will be a superposition of the fields of the horizontal and vertical induced dipoles. Along with the three major assumptions already pointed out, the expressions in Equations A.1 through A.4 carry with them several additional assumptions. For the sake of clarity, all assumptions concerning this simplified target response model are now listed.

(1) The transmitter is a point magnetic dipole.

(2) The target is a solid, metallic sphere.

(3) The target is buried in an infinite conducting half-space with homogeneous conductivity.

(4) The sphere must be electrically small. This means that the radius of the sphere must be small compared to the wavelength of the transmitted pulses. This is always true for the EM61 case since a transmitter at $75.0Hz$ has a wavelength of $4000km$.

(5) The sphere must be located a sufficient distance from the source/observer. This insures that higher order multipoles can be ignored.

(6) The sphere must be buried a sufficient distance from the interface. This insures that the interaction between the induced dipoles and the interface are unimportant. It has been shown that the sphere-interface separation should be at least two sphere radii [88].

(7) The induced electric dipole moment is negligible. In addition to the vertical and radial magnetic fields, a vertical dipole on the surface also creates an electric field in the azimuthal direction, which circles the vertical axis. This electric field will induce an electric dipole moment in the target that will contribute to the vertical magnetic field on the surface. The electric dipole contribution is negligible for low frequencies (i.e. under 10 kHz), which is always valid for the EM61.

A.4 Receiver Characteristics

This section discusses how the secondary magnetic field is converted into a voltage at the output of the receivers. There are two approaches that could be taken. The first is to consider the primary magnetic field as being excited by a change in the DC level of the transmitter current. After the primary field has been zeroed, the secondary field decays exponentially with the following form [89]:

$$H_s(t) = Ae^{-\frac{t}{\tau}} \tag{A.5}$$

$$\tau = \sqrt{\frac{\sigma_s \mu_s a^2}{\pi}} \tag{A.6}$$

Here A is the strength of the magnetic field at the instant before the transmitter current is brought to zero. τ is the time constant of the secondary field decay with a, σ_s, and μ_s corresponding to the radius, conductivity, and magnetic permeability of the metallic sphere. This approach requires knowledge of the sampling time after the the primary pulse is zeroed, as well as, a Laplace analysis of the receivers to determine the response of the coils to a transient magnetic field. Because the transmitter operates continuously, however, a simpler way of modeling the excitation, induction, and reception problem is harmonically (i.e. in the frequency domain). The transmitter can be thought of as the superposition of sinusoidal magnetic dipoles with frequencies of $75Hz$ and odd harmonics. Since the fundamental frequency of $75Hz$ is demodulated and filtered, it is the only frequency that need be considered. The problem reduces to multiplying the secondary magnetic field by a transfer function $F(\omega)$ that converts magnetic field into an output voltage.

Figure A.4 illustrates an EM61 receiver. Each coil converts an external magnetic field into a voltage that is sampled by the electronics. The sampler opens a window δt seconds wide and averages the coil's response, $r(t)$, over that window. The width of δt is $400\mu s$. The output of the sampler is a digital train of samples that is multiplied by a $75Hz$ cosine wave, which is synchronized to the transmitter. This has the effect of demodulating the $75Hz$ fundamental to base band. Then a low pass filter with a cutoff of $0.8Hz$ is applied to the demodulated stream of samples to reject all frequencies other than $75Hz$. The final result is a DC output level, which is stored in digital memory.

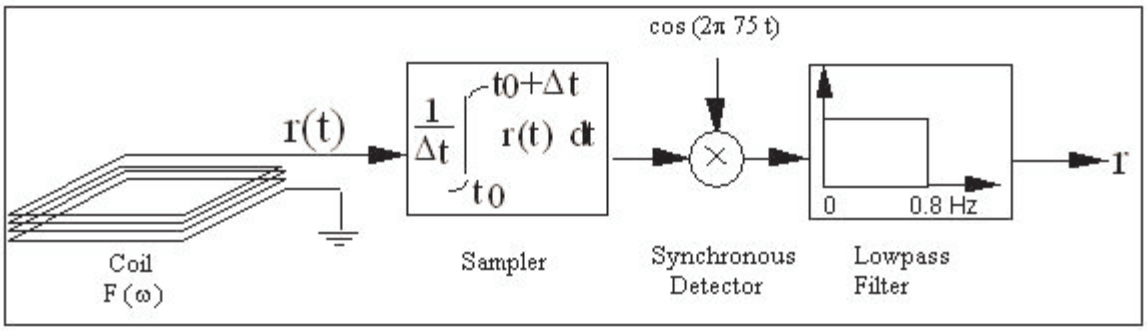

Figure A.4: Receiver Schematic Diagram

A.5 Spatial Response of a Point Sensor

To introduce the modeling of the EM61's spatial response, the sensor will be assumed to be infinitesimally small. In other words a point sensor. The spatial extent of the actual physical sensor has the effect of smoothing the spatial response and is presented in the next section. For the point sensor the spatial response will be denoted $p(x, y)$.

It has been shown that at any location near a buried target the vertical magnetic dipole of the EM61 transmitter induces magnetic dipole responses in the target. These induced sources are the vertical and radial dipoles. Because the EM61 receivers are oriented vertically, the components of the spatial signal, $p(x, y)$, will be the sum of the vertical magnetic fields produced by each induced dipole. The main receiving coil response is developed here. (The secondary coil differs only in the fact that it is located 0.4 m above the main.)

First consider the response of the sensor to the fields of a vertical magnetic dipole below the ground with a constant amplitude of $1Am^2$. The vertical magnetic field as a function of position will be denoted $H_{zz}(x, y)$. The response of the sensor will be the magnetic field times the transfer function $F(\omega)$, which has units of $\frac{V}{Tesla}$, so $V_{zz}(x, y) = F(\omega)H_{zz}(x, y)$. The induced vertical dipole moment, $m_z(x, y)$ scales the received amplitude to give the vertical dipole half of the spatial response, $m_z(x, y)V_{zz}(x, y)$. Similarly, the sensor response from the radially induced dipole will be $m_r(x, y)V_{rz}(x, y)$. Here $V_{rz}(x, y) = F(\omega)H_{rz}(x, y)$ is the response of the sensor to a radial dipole of $1Am^2$ and $m_r(x, y)$ is the radially induced dipole moment. The resulting expression for the point

sensor response is:

$$p(x,y) = m_z(x,y)V_{zz}(x,y) + m_r(x,y)V_{rz}(x,y) \tag{A.7}$$

A subtle point is that the radial induced dipole will always be pointing away from the sensors for any position (x,y). This is because the transmitter is fixed to the receivers. Therefore, the sensor response will be circularly symmetric.

A.6 Accounting for Sensor Size

The physical dimensions of the EM61 coils are 1m $\times$ 1m. This is large enough to suggest that the measured response of buried UXO will differ from the point sensor. The voltage measured by a magnetic induction coil is proportional to the time rate of change of the total magnetic flux passing thourgh the area of the coils. This is Faraday's Law. Thus the sensor response will be proportional to an integral over the magnetic field passing through the coil. This can be accounted for by revisiting the response of the sensor to a vertical and radial unit dipole. The spatial response, $s(x,y)$, is then given by:

$$s(x,y) = m_z(x,y)\int_{x'=-\frac{1}{2}}^{\frac{1}{2}}\int_{y'=-\frac{1}{2}}^{\frac{1}{2}} V_{zz}(x,y) + m_r(x,y)\int_{x'=-\frac{1}{2}}^{\frac{1}{2}}\int_{y'=-\frac{1}{2}}^{\frac{1}{2}} V_{rz}(x,y) \tag{A.8}$$

The position (x,y) is the center of the receiver and the integrals over (x',y') are over the area of the sensor centered at the point (x,y). Note that the induced dipole terms, $m_z(x,y)$ and $m_r(x,y)$ are not included in the integrals. This is because transmitter is still assumed to be a point dipole, and m_z & m_r are scale factors related to the transmitter's position (x,y). (No attempt has been made to account for the physical size of the transmitter because this would involve a multipole expansion of the source fields.) Equation A.8 may be rewritten as a convolution with rectangle functions.

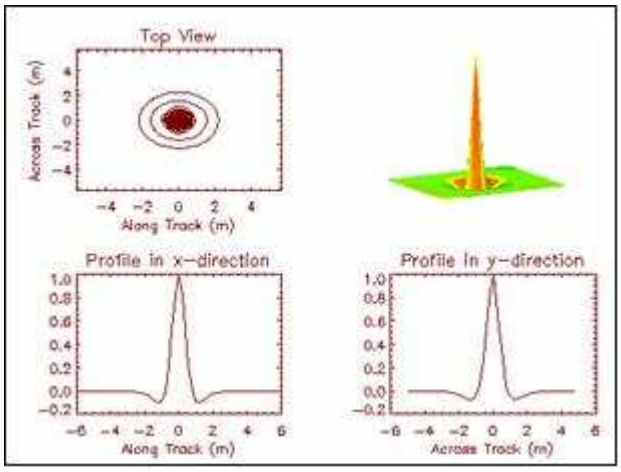

Figure A.5: EMI Spatial Response

$$s(x,y) = m_z(x,y)\,(V_{zz}(x,y) \otimes\otimes rect(x,y)) + m_r(x,y)\,(V_{rz}(x,y) \otimes\otimes rect(x,y)) \quad \text{(A.9)}$$

Here $rect(x,y) := 1$ for $\{-\frac{1}{2} \leq x \leq \frac{1}{2}\}$ and $\{-\frac{1}{2} \leq y \leq \frac{1}{2}\}$ and $rect(x,y) := 0$ otherwise and the operator $\otimes\otimes$ denotes two dimensional convolution. Figure A.5 illustrates the spatial response, $s(x,y)$, for the case of a 0.25m radius, aluminum sphere buried at a depth of 1 m.

APPENDIX B

MAGNETOMETERS

The operation of the Cesium vapor magnetometer is outlined in this work. The primary feature that gives this technology an advantage in landmine and UXO detection is the ”clean” nature of the measurement. That is, the instrument itself does not significantly affect the magnetic field that is being measured. This allows it to interact with the environment without changing it.

DC magnetic signatures measured are cause by the buried object deflecting the Earth’s magnetic field. These changes are detected by the sensor. Only objects that contain iron can be detected. Cesium vapor magnetometers are useful in the detection of unexploded ordnance (UXO).

B.1 Sensor Operation

Cesium vapor magnetometers work on the principle of the Zeeman effect. They are a part of the larger set of instruments known as ”optically pumped magnetometers”. The Cesium atom has a special property. When it is exposed to a DC magnetic field, the electrons can take on three unique energy levels. The first is a high energy level, the other two are lower energy levels. Figure B.1 illustrates the three levels. When light is passed through the vapor, electrons in the ”Low 1” energy level will transition to the high energy state. This absorbs the energy in a single photon. The photon is re-emitted when the electron falls back to one of the lower energy states. There is an even chance that the falling electron will transition to ”Low 2” energy level instead of ”Low 1”. This level does not allow the

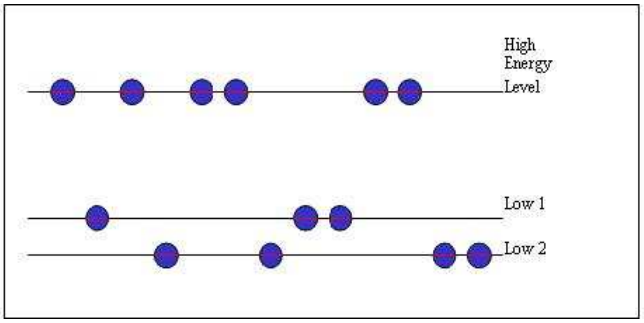

Figure B.1: Electron Energy Levels in a Cesium atom in the presence of a DC Magnetic Field

electrons to be re-excited back to the high energy state. The electron is then stuck [90] .

Initially, all the electrons are randomly populated in the three states. However, eventually all the electrons will become trapped in the ”Low 2” state. The cesium vapor is then oblique to light. If an RF magnetic field, however, is applied to the vapor, the electrons in the lower energy states are ”re-mixed”. That is, the electrons in the lower energy states will again be randomly populated. The vapor can then absorb and re-emit photons again, and the vapor becomes transparent to light. The external magnetic field determines the energy difference between the two lower levels. The energy required to randomize the electrons in the lower states is proportional to the frequency of the applied RF magnetic field. The frequency of the applied RF field is, therefore, a measure of the external DC magnetic field [1].

B.2 Measuring DC Magnetic Fields

The magnetic field that is measured by a pulsed magnetometer is the Earth’s DC magnetic field. The existence of an iron object causes the Earth’s field to be bent in the region local to the object. This is because the field must satisfy the boundary conditions. (Tangential magnetic field can be discontinuous at the boundary by the surface current density. Since no surface current will exist, the tangential magnetic field must be 0.) This is illustrated in Figure B.2. The advantage of using a pulsed magnetometer is that the optical nature of the sensor causes very little change in the magnetic field being measured. The instrument,

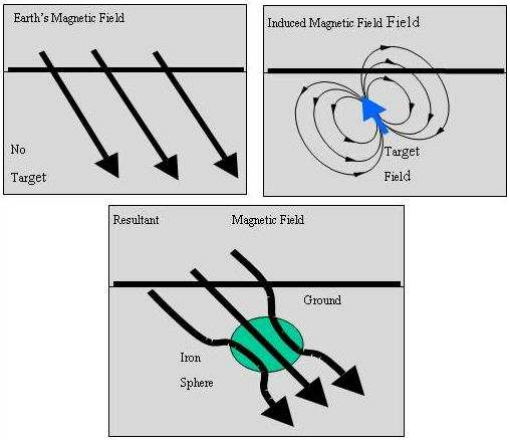

Figure B.2: Effect of an Iron Object on the Earth's Magnetic Field

therefore, minimally affects the observation.

The deviations in the Earth's DC magnetic field are measured by the magnetometer. Figure B.3 shows a simulated signature from an iron sphere buried at 0.5m below the surface. For this simulation, the object is magnetically a dipole oriented in the y-direction (i.e. East). The orientation of the target's source is dependent upon the direction of the Earth's magnetic field, the iron content of the object, and the targets shape. It is difficult to predict exactly how the magnetic signature will behave. Figure B.5 shows the signatures produced on a magnetometer by the four buried targets of Figure B.4. The orientations of the four targets affect the signatures that they produce. BLU-1 is a sphere so it has no distinguishing orientation, BLU-2 is vertical into the ground,

BLU-3 is lying horizontally at a 90 degree angle to North, and BLU-4 is lying horizontally at 0 degrees with respect to North. BLU-2 and BLU-3 have similar features as the simulation shown in Figure B.3. They have a positive and negative peak on either side of the known location of the buried object. The location of the peaks is in the y-direction meaning that the magnetic source is like a dipole oriented perpendicular to the Earth's field. This makes sense for BLU-3 since it is buried with its major axis perpendicular to the direction of North. The Earth's magnetic field lines will tend to be oriented in the direction of the major access. It is less clear why BLU-2 would have this characteristic.

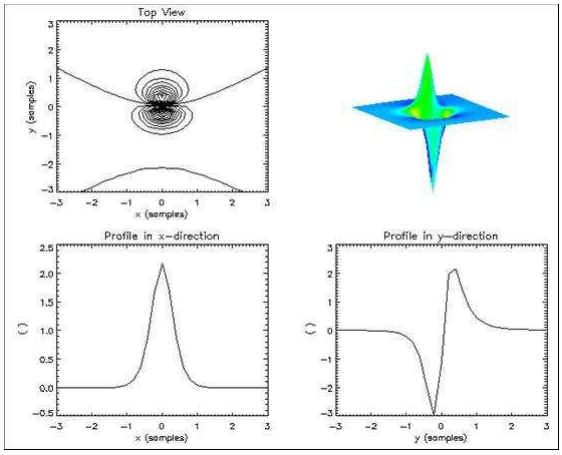

Figure B.3: Simulated Spatial Signal from a magnetometer

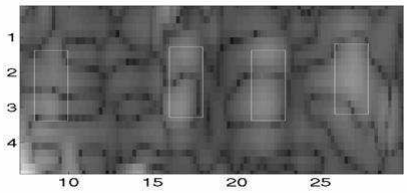

Figure B.4: Signatures of Buried UXO on a Magnetometer

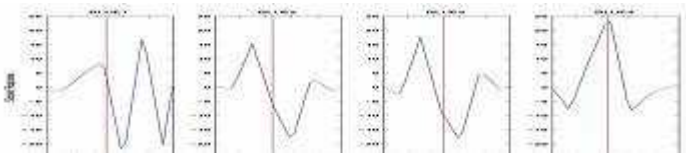

Figure B.5: Along Track UXO Signatures on a Magnetometer Sensor

The vertical lines of Figure B.5 show the target location as listed in the ground truth.

APPENDIX C

X-RAY BACKSCATTER

Since the First World War a single technology for landmine detection has dominated. This technology is the metal detector. A very effective counter measure to this sensor was soon invented - plastic cased landmines. To this day plastic mines are a challenge to detect. This has led to much innovative research. The application of X-ray backscatter technology to the landmine problem is one of these innovations. The primary physical mechanism used is Compton Scattering from the explosive contained in the mine. The key to an observed signature is the difference in the atomic number of soil and that of the explosive material. Another key to this technology is imaging. Since other objects found in the ground have atomic numbers similar to explosives, imaging is required to distinguish between landmines and various false-alarms. In this section the use of X-ray backscatter technology is explored as a solution to the problem of detecting plastic cased landmines.

Figure C.1: Plastic Cased Anti-tank Landmine

C.1 X-ray Backscatter Imaging

Many of the technologies developed for landmine detection have utilized aspects of the landmine packaging. For example metal detectors detect the metal casing of the mine. Ground penetrating radar (GPR) also seeks to detect the casing. In this case the signature is produced by the differing electrical properties of the casing and the soil. In recent years researchers have attempted to utilize the fundamental characteristic that separates landmines from all other clutter objects - the explosive material. The quest for a sensor that detects the explosives in the mine has become the ”Holy Grail of landmine detection”.

C.1.1 Linear Attenuation

X-ray backscatter technology has been an attractive research direction because it keys on the differing atomic number of landmine explosive material (typically about 7) from the surrounding soil (typically about 11) [91]. This and the higher density of soil compared to landmines makes the linear attenuation of x-rays greater when no landmine is present. Observed backscattered x-rays, therefore, show higher fluence levels when a landmine is present. This leads to an observable signal detectable in the imagery produced. Equation C.10 shows the attenuation of x-ray fluence due to attenuation in a material. $\Phi(x)$ is the fluence at location x along the path, Φ_0 is the initial x-ray fluence.

$$\Phi(x) = \Phi_0 e^{-\mu x} \tag{C.10}$$

The density of an average soil is reported to be 2.65 $\frac{g}{m^3}$. The density of TNT explosives, on the other hand, is 1.65 $\frac{g}{m^3}$. The equations governing linear attenuation are shown in Equations C.11 and C.12. Equation C.11 is the relationship for Compton scattering absorption. Equation C.12 is the relationship for Photo-electric absorption. These are the two major mechanism of X-ray absorption in the landmine backscatter problem (for energies less than 1000keV).

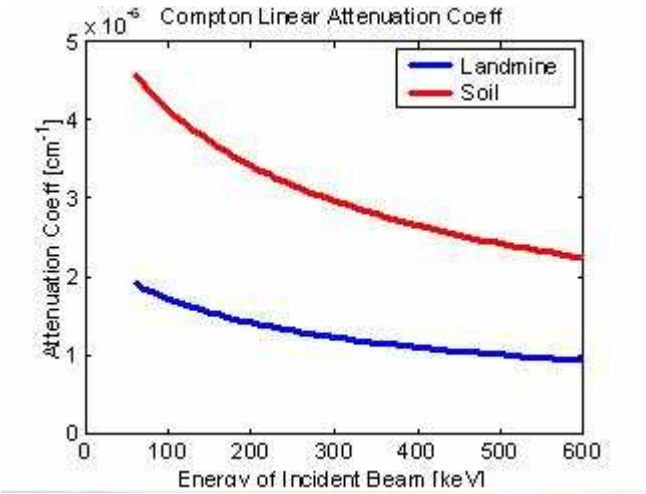

Figure C.2: Compton Linear Attenuation

$$\mu_c = \sigma_c \rho N_0 \frac{Z}{A} \tag{C.11}$$

$$\mu_{pe} = k \frac{Z^4}{E^3} \frac{\rho}{A} \tag{C.12}$$

Where ρ is the density of the material, A is the material's equivalent atomic mass number, Z is the material's equivalent atomic number, E is the energy of the incident X-ray beam, k is a shell constant ($k = 21.86$), N_0 is Avogadro's number ($N_0 = 6.022 \times 10^{23}$), and σ_c is the collision cross section. Note that the collision cross section depends on E and Z and is shown in Equations C.14, C.15, and C.16.

Figures C.2 and C.3 show that soil is a more absorbing material than TNT for all energies between 60 and 600 keV. In energies above around 300keV, Compton Scattering is the main attenuation mechanism. Another attenuation mechanism, pair production, begins to prevail at energies above 1000keV. Section C.2 discusses optimal system design including the choice of incident x-ray energy.

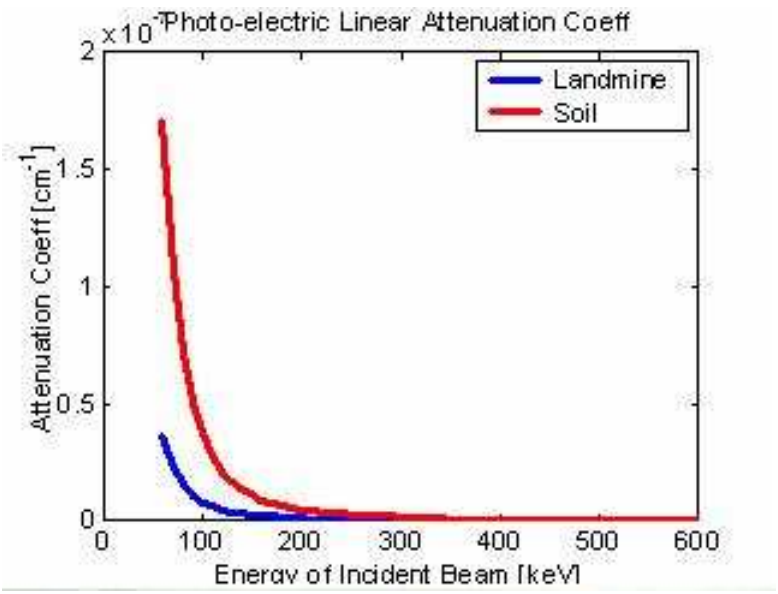

Figure C.3: Photo-electric Attenuation

C.1.2 Compton Scattering

The primary mechanism that allows sensors at the surface to detect x-rays launched from the surface is Compton scattering. This mechanism is proof of the particle nature of photons because the x-rays behave according to the rules of particle collisions. Equation C.13 shows the conservation of momentum equation governing a Compton collision. E_{in} is the energy of incident x-ray beam while

$$\frac{1}{E_{in}} - \frac{1}{E_{out}} = \frac{1}{mc}(1 + \cos 2\theta) \tag{C.13}$$

E_{out} is the scattered beam energy. The speed of light in a vacuum is c and m is the mass of an electron. Equation C.13 has been specially formulated for the angle θ_1 equal to the angle θ_2 (i.e. $\theta_1 = \theta_2 = \theta$). For the case of $\theta = 45°$ the exiting x-ray energy is equal to the incident x-ray energy. In Section C.2 an imaging system is proposed that utilizes this arrangement in a landmine detection system.

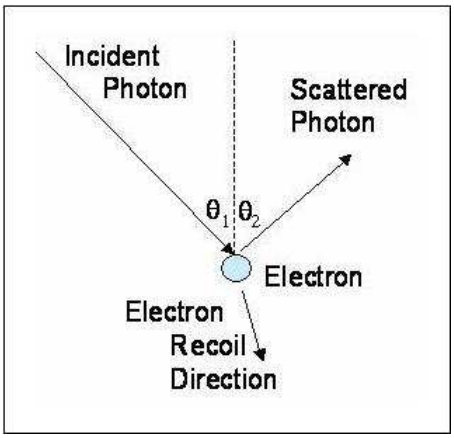

Figure C.4: Compton Scattering

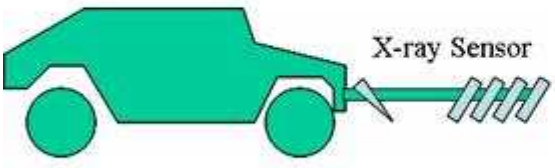

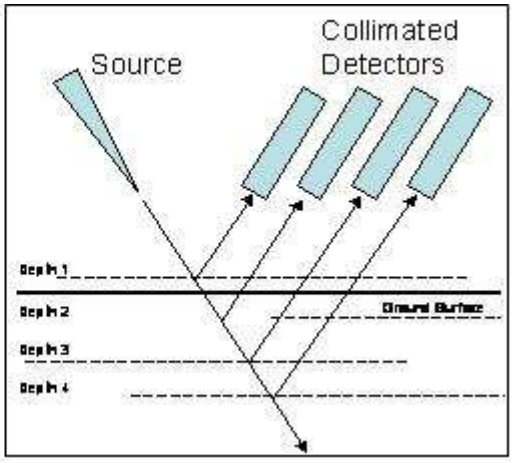

Figure C.5: Proposed X-ray Backscatter Imaging Scanner

C.2 Proposed 3D Imaging Scanner

As early as 1967 systems utilizing X-ray backscatter technology began to appear as research prototypes. One of the earliest pioneers was the University of Florida [91]. With support of the USArmy a directly downward looking system with 130kVp x-ray source was produced. This system is now the U. of Florida's X-ray Mine Imaging System (XMIS) [92]. Another system has been produced by the University of California San Diego with support from Defence R&D Canada. This system is called the High Energy X-ray Imaging Survey [93] [94] (HEXIS) sensor. It has an energy range of 10-200keV [93]. The most recent system to appear is a German effort called ComScan450. This system, built by YXLON International uses a 450kV x-ray tube and detector [95].

The above systems all have similarities and differences. A combination/extension of them is illustrated in Figure C.5. This proposed system utilizes an x-ray source tilted forward at a 45° angle. An array of collimated detectors is shown. Each detector is located a specifically designed distance from the source and has orientations of -45° to match the source.

The choice of distance between source and detector is driven by the depth to be observed. Table C.1 shows the source-detector separation distance for a detector located 3" above the ground surface. This corresponds to a constant separation distance of 7.35" for each detector. By using collimated detectors and a lateral scanning scheme, a 3D image of the subsurface transmission may be obtained.

An optimal incident x-ray energy for the design described here is between 300keV and 1000keV. This choice is driven by the fact that Compton Scattering dominates for energies above 300keV. This is seen in Figure C.6, which shows the ratio of Compton absorption to Photo-electric absorption for energies from 60 to 600keV. This simulation was computed using the material properties of TNT. An excellent choice for mono-energetic x-ray radiation would be 450keV. (The German system is the closest to this situation. It uses a 450kVp x-ray tube.)

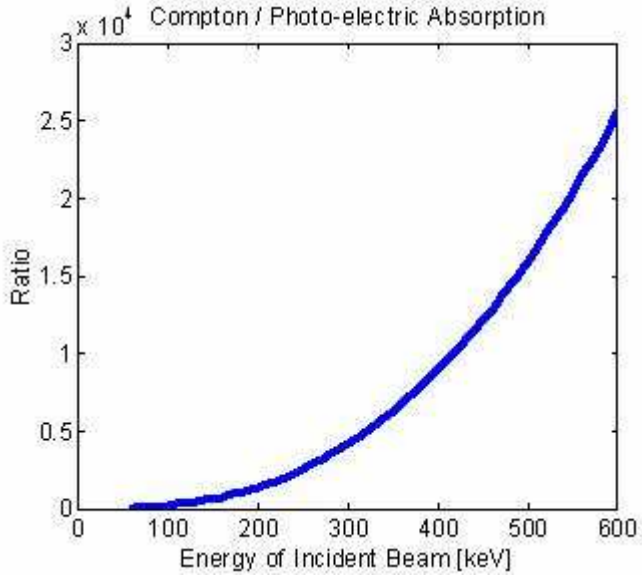

Figure C.6: Ratio of Compton to Photo-electric Absorption

Table C.1: Detector Distances

Depth [in]	Distance [in]
-2	2.45
1	9.80
4	17.15
7	24.49

C.3 Performance Limitations

Several issues limit the performance of the proposed system. Most notably is the issue of power required to generate a signal that can penetrate over 6” and be measured with collimated detectors. Because a 3D image is desired, collimation is necessary. This insures that multiply scattered x-rays will be rejected, but also increases the system power requirements. Two of the issues faced by this system are described below.

C.3.1 Soil Water Content

The primary effect of ground moisture is to increase the density of soil. This makes the linear attenuation of the soil higher. Ultimately, the power supply of the x-ray source must be able to generate x-rays that can penetrate deeper than 6” depth.

A secondary effect of water moisture content is its random nature. Naturally occurring variations in the hydrogen content of the soil due to water produce many false alarms. This is especially true if the ground moisture content is greater than 10% [94]. Imaging combined with fusion with other sensors is a way to mitigate many of these false alarms.

C.3.2 Collision Cross Section

Another challenge for the system is the collision cross section of Compton Events for TNT material. This is the probability of a Compton event occurring within the explosive material. The differing atomic numbers of landmines and soil actually make it more likely for scattering to occur from the soil than from the landmine. This poses a signal-to-noise ratio problem that must be overcome by system power.

The dependence of collision cross section to atomic number is shown in Equations C.14, C.15, and C.16. This expression is linear in atomic number. Since a material with higher atomic number has more electrons, the probability of an event is increased. (An assumption is made here that all electrons of the material are available as free electrons. This isn’t necessarily always true.)

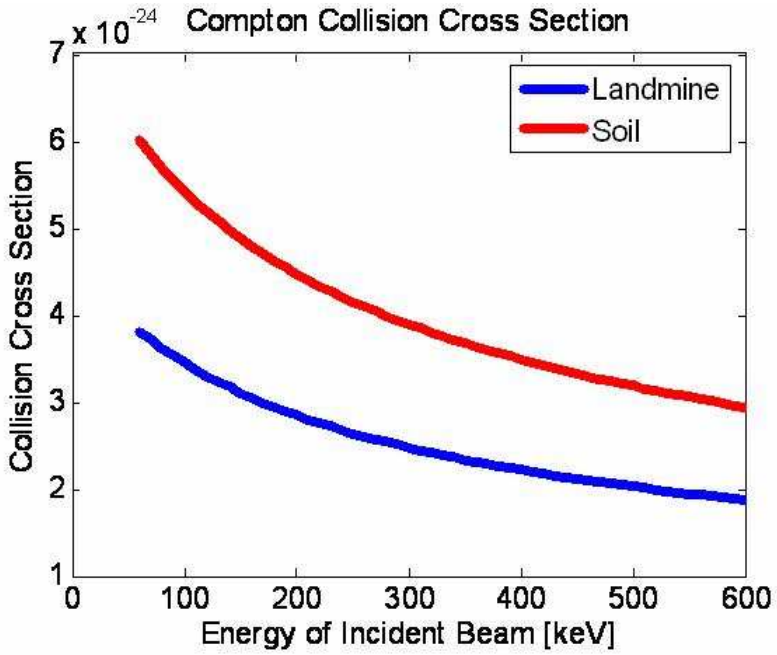

Figure C.7: Collision Cross Section of Compton Events

$$\sigma_c = Z\sigma_0 \frac{3}{4}\left[\frac{2(1+\alpha)^2}{\alpha^2(1+2\alpha)} + \frac{\log(1+2\alpha)}{\alpha}\left(\frac{1}{2} - \frac{1+\alpha}{\alpha^2}\right) - \frac{1+3\alpha}{(1+2\alpha)^2}\right] \tag{C.14}$$

$$\sigma_0 = \frac{8\pi}{3} 2.818 \times 10^{-13} \tag{C.15}$$

$$\alpha = \frac{E}{511} \tag{C.16}$$

Where E is the energy of the incident X-ray in keV, and Z is the atomic number of the material [96]. The collision cross section, therefore, depends on incident energy, E, and material atomic number, Z. Figure C.7 shows the energy dependence of the cross section for the 60-600keV range.

Note in Figure C.7 that the soil cross section is almost twice as high as the explosive material of the landmine. This means that more backscattered x-rays will be generated by the soil than by the explosive material. Images containing landmines will, therefore, have lower signal-to-noise ratio than images without landmines.

C.4 X-ray Backscatter Conclusions

In this section the application of X-ray Backscatter Technology to the detection of low-metal landmines has been explored. This approach makes use of Compton Scattering of x-rays and differing linear attenuation coefficients of explosive material and soil. The difference arises from the atomic numbers (TNT: about 7 and soil: about 11) and the fact that soil is significantly denser (TNT: 1.65 $\frac{g}{m^3}$ and soil: 2.65 $\frac{g}{m^3}$).

Investigation of the mathematical dependence of Compton and photo-electric attenuation shows that the best choice of x-ray energies is in the 300 to 1000keV region. This is the region where Compton scattering is the dominant attenuation effect. A system utilizing a set of collimated detectors is proposed. By employing a scanning scheme, the system is able to acquire a 3D image set of the subsurface attenuation.

Because X-ray Backscatter keys on the material characteristics of the explosive material, rather than the landmine casing, it is considered an ideal technology for non-metal cased (plastic) landmine detection.

BIBLIOGRAPHY

BIBLIOGRAPHY

[1] H. Ksienski, Y. Lin, and L. White, "Low-frequency approach to target identification," *Proceedings of the IEEE*, vol. 63, pp. 1651–1659, 1975.

[2] M. Allen, J. Jauregui, and L. Hoff, "Fopen-sar detection by direct use of simple scattering physics," in *Proceedings of SPIE Algorithms for Synthetic Aperture Radar Imagery II*, (Orlando, FL), pp. 45–55, 1995.

[3] J. Gorman and J. Marble, "A low complexity multi-discriminant fopen target screener," in *Proceedings of SPIE Algorithms for Synthetic Aperture Radar Imagery V*, (Orlando, FL), pp. 307–317, 1998.

[4] C. Baum, *Detection and Identification of Visually Obscured Targets*. Bristol, PA: Taylor and Francis, 1988.

[5] J. Lee and S. Mudaliar, "Optimum polarizations in the bistatic scattering from layered random media," *IEEE Trans. Geoscience and Remote Sensing*, vol. 32, pp. 169–176, 1994.

[6] A. Freundorfer and K. Iizuka, "A study on the scattering of radio waves from buried spherical targets using the step frequency radar," *IEEE Trans. Geoscience and Remote Sensing*, vol. 31, pp. 1253–1255, 1993.

[7] J. Ackenhusen, Q. Holmes, C. King, and J. Wright, *Detection of Mines and Minefields*. Ann Arbor, MI: Infrared Information Analysis Center, 2001.

[8] L. Carin, N. Geng, M. McClure, J. Sichina, and L. Nguyen, "Ultra-wide-band synthetic-aperture radar for mine-field detection," *IEEE Trans. Antennas and Propagation*, vol. 41, pp. 18–33, 1999.

[9] W. Brown, "Synthetic aperture radar," *IEEE Trans. Aerospace and Electronic Systems*, vol. 3, pp. 217–229, 1967.

[10] W. Brown and L. Porcello, "Introduction to synthetic aperture radar," *IEEE Spectrum*, pp. 52–62, 1969.

[11] D. Munson and R.Visentin, "A signal processing view of strip-mapping synthetic aperture radar," *IEEE Trans. Acoustics, Speech, and Signal Processing*, vol. 37, pp. 2131–2147, 1989.

[12] R. Stewart, *Methods of Satellite Oceonography*. Berkeley, CA: University of California Press, 1985.

[13] J. Johnson, P. Lucey, K. Horton, and E. Winter, "Spectral contrast differences between field and laboratory infrared measurements of pristine and disturbed soils," *Remote Sensing of the Environment*, vol. 64, pp. 33–46, 1998.

[14] M. Cherniakov and L. Donskoi, "Frequency band selection of radars for buried object detection," *IEEE Trans. Geoscience and Remote Sensing*, vol. 37, pp. 838–845, 1999.

[15] A. Hibbs and et al, "First year progress and test results," in *Proc. IEE. Detection of Abandoned Landmines*, pp. 138–141, 1998.

[16] D. Daniels, *Surface Penetrating Radar*. London: IEE, 2000.

[17] L. Riggs, J. Mooney, D. Lawrence, J. Broach, and A. Trang, "Identification of metallic mines using low frequency magnetic fields," in *Proc. SPIE Int. Detection and Remediation Technologies for Mines and Minelike Targets III*, (Orlando, FL), pp. 146–157, 1998.

[18] C. Baum, "Singularity expansion method," *Proceedings of the IEEE*, vol. 79, pp. 1481–1492, 1991.

[19] D. Hall and J. Llinas, "An introduction to multisensor data fusion," *Proceedings of the IEEE*, vol. 1, pp. 6–22, 1997.

[20] L. Song, C. Yu, and Q. Liu, "Through-wall imaging (twi) by radar: 2-d tomographic results and analyses," *IEEE Transactions on Geoscience and Remote Sensing*, vol. 12, pp. 2793–2798, 2005.

[21] Q. Liu, Z. Zhang, and et.al., "Active microwave imaging i - 2-d forward and inverse scattering methods," *IEEE Transactions on Microwave Theory and Techniques*, vol. 50, pp. 123–133, 2002.

[22] Z. Zhang and Q. Liu, "Three-dimensional nonlinear image reconstruction for microwave biomedical imaging," *IEEE Transactions on Biomedical Engineering*, vol. 51, pp. 544–548, 2004.

[23] L. Song and Q. Liu, "Fast three-dimensional electromagnetic nonlinear inversion in layered media with a novel scattering approximation," *Inverse Problems*, vol. 20, pp. 171–194, 2004.

[24] C. Yu, L. Song, and Q. Liu, "Inversion of multi-frequency experimental data for imaging complex objects by a dta-csi method," *Inverse Problems*, vol. 21, pp. 165–178, 2004.

[25] S. Rao, D. Wilton, and A. Glisson, "Electromagnetic scattering by surfaces of arbitrary shape," *IEEE Trans. Antenna Propag.*, vol. 30, pp. 409–418, 1992.

[26] P. Corona, A. D. Bonitatibus, G. Ferrara, and C. Gennarelli, "A very accurate model for backscattering by right angled dihedral corners," in *Proceedings of the IEEE Antennas and Propagation Society International Symposium*, pp. 1734–1737, 1990.

[27] J. Marble, D. Wilcox, and R. Mersereau, "Landmine signatures in ground penetrating radar," in *Proc. SPIE Int. Detection and Remediation Technologies for Mines and Minelike Targets VI*, (Orlando, FL), pp. 720–729, 2001.

[28] X. Xiaoyin and E. Miller, "A statistical method to localize buried landmines from gpr array measurements," in *Proc. SPIE Int. Detection and Remediation Technologies for Mines and Minelike Targets VI*, (Orlando, FL), pp. 742–753, 2001.

[29] J. Marble and A. Yagle, "Measuring landmine size and burial depth using ground penetrating radar," in *Proc. SPIE Int. Detection and Remediation Technologies for Mines and Minelike Targets IX*, (Orlando, FL), pp. 409–420, 2004.

[30] H. Anton, *Calculus with Analytic Geometry*. New York: John Wiley & Sons, 1984.

[31] Y. Nievergelt, "Fitting conics of specific types to data," *Linear Algebra and Its Applications*, vol. 378, pp. 1–30, 2004.

[32] J. Marble, D. Wilcox, and R. Mersereau, "Mine/uxo sensor phenomenology," in *Proceedings 3rd Annual Federated Laboratory Symposium*, (College Park, MD), pp. 317–322, 2000.

[33] A. Banos, *Dipole radiation in the Presence of a Conducting Half-Space*. London: Pergamon Press, 1966.

[34] T. Moon and W. Stirling, *Mathematical Methods and Algorithms for Signal Processing*. Upper Saddle River, NJ: Prentice Hall, 2000.

[35] H. V. Trees, *Detection, Estimation, and Modulation Theory*. New York, NY: John Wiley & Sons, 2001.

[36] C. Balanis, *Advanced Engineering Electromagnetics*. Hoboken, NJ: John Wiley & Sons, 1989.

[37] J. Marble, A. Yagle, and A. Hero, "Sensor management for landmine detection," in *Proceedings of SPIE Detection and Remediation Technologies for Mines and Minelike Targets X*, (Orlando, FL), pp. 1217–1228, 2005.

[38] T. Hastie, R. Tibshirani, and J. Friedman, *The Elements of Statistical Learning*. New York, NY: Springer-Verlag, 2001.

[39] W. Scott, K. Kim, G. Larson, and J. McClellan, "Combined seismic, radar, and induction sensor for landmine detection," *IEEE Trans. Geoscience and Remote Sensing Society*, vol. 3, pp. 1613–1616, 2004.

[40] P. Gao, L. Collins, L. Garber, N. Geng, and L. Carin, "Classification of landmine-like metal targets using wideband electromagnetic induction," *IEEE Trans. Geoscience and Remote Sensing Society*, vol. 38, pp. 1352–1361, 2000.

[41] P. Gader, M. Mystkowski, and Y. Zhao, "Landmine detection with ground penetrating radar using hidden markov models," *IEEE Trans. Geoscience and Remote Sensing Society*, vol. 38, pp. 1231–1244, 2001.

[42] S. Russel and P. Norvig, *Artificial Intelligence A Modern Approach*. Prentice Hall.

[43] W. Schmaedeke and K. Kastella, "Event-averaged maximum likelihood estimation and information-based sensor management," in *Proceedings of SPIE*, pp. 91–96, June 1994.

[44] K. Balaji, A. Hartemink, L. Carin, and M. M. Figueiredo, "A bayesian approach to joint feature selection and classifier design," *IEEE Trans. on Pattern Analysis and Machine Intelligence*, vol. 26, pp. 1105–1111, 2004.

[45] V. Krishnamurthy, "Algorithms for optimal scheduling and management of hidden markov model sensors," *IEEE Trans. on Signal Processing*, vol. 49, pp. 2893–2908, 2001.

[46] C. Kreucher, E. Kastella, and A. Hero, "A bayesian approach to multiple target detection and tracking," *IEEE Trans. on Signal Processing*, vol. 41, pp. 1396–1414, 2005.

[47] A. Banos, *Dipole radiation in the Presence of a Conducting Half-Space*. London: Pergamon Press, 1966.

[48] J. Marble, A. Yagle, and G. Wakefield, "Physics derived basis pursuit in buried object identification using emi sensors," in *Detection and Remediation Technologies for Mines and Minelike Targets X*, (Orlando, FL), pp. 1151–1159, 2005.

[49] C. Wang and L. Collins, "Feature selection for physics model based object discrimination," in *Detection and Remediation Technologies for Mines and Minelike Targets X*, (Orlando, FL), pp. 1200–1208, 2005.

[50] J. Marble, A. Yagle, and A. Hero, "Multimodal, adaptive landmine detection using emi and gpr," in *Proceedings of SPIE Detection and Remediation Technologies for Mines and Minelike Targets X*, (Orlando, FL), pp. 1209–1216, 2005.

[51] L. Carin, N. Geng, M. McClure, Y. Dong, Z. Liu, J. He, J. Sichina, M. Ressler, L. Nguyen, and A. Sullivan, "Wide-area detection of land mines and unexploded ordnance," *Inverse Problems*, vol. 18, pp. 575–609, 2002.

[52] X. Liao and L. Carin, "Application of the theory of optimal experiments to adaptive electromagnetic-induction sensing of buried targets," *IEEE Trans. on Pattern Analysis and Machine Intelligence*, vol. 26, pp. 961–972, 2004.

[53] M. Kolba, P. Torrione, and L. Collins, "Information-based sensor management for landmine detection using multimodal sensors," in *Detection and Remediation Technologies for Mines and Minelike Targets X*, (Orlando, FL), pp. 1098–1107, 2005.

[54] D. Blatt and A. Hero, "From weighted classification to policy search," in *Proc. of the Nineteenth Annual Conference on Neural Information Processing Systems*, (Vancouver, BC), 2005.

[55] W. Scott, K. Kim, G. Larson, A. Gurbuz, and J. McClellan, "Combined seismic, radar, and induction sensor for landmine detection," in *Proceedings of the IEEE International Geoscience and Remote Sensing Symposium*, (Anchorage, AK), pp. 1613–1616, 2004.

[56] K. Kim and W. Scott, "An improved resistively-loaded vee dipole for ground-penetrating radar applications," in *Proceedings of the IEEE Antennas and Propagation Society International Symposium*, (Monterey, CA), pp. 2548–2551, 2004.

[57] K. Kim and W. Scott, "A resistive linear antenna for ground penetrating radar applications," in *Detection and Remediation Technologies for Mines and Minelike Targets IX*, (Orlando, FL), pp. 359–370, 2004.

[58] S. Twomey, *Introduction to the Mathematics of Inversion in Remote Sensing and Indirect Measurements*. Mineola, NY: Dover Publications, 1977.

[59] R. Raich and A. Hero, "Sparse image reconstruction for partially known blur functions," in *IEEE International Conference on Image Processing*, (Atlanta, GA), pp. 637–640, 2006.

[60] J. Marble and A. Hero, "Iterative redeployment of illumination and sensing (iris): Application to stw-sar imaging," in *Proc. of the 25th Army Science Conference*, (Orlando, FL), 2006.

[61] L. Scharf, *Statistical Signal Processing*. Reading, MA: Addison-Wesley, 1991.

[62] C. Cafforio, C. Prati, and F. Rocca, "Sar data focusing using seismic migration techniques," *IEEE Transactions on Aerospace and Electronic Systems*, vol. 27, pp. 194–206, 1991.

[63] W. Carrara, R. Goodman, and R. Majewski, *Spotlight Synthetic Aperture Radar*. Boston: Artech House, 1995.

[64] M. Soumekh, *Synthetic Aperture Radar Signal Processing*. New York: Wiley-Interscience, 1999.

[65] R. Stolt, "Migration by fourier transform," *Geophysics*, vol. 43, pp. 23–48, 1978.

[66] M. Ting, R. Raich, and A. Hero, "Sparse image reconstruction using sparse priors," in *IEEE International Conference on Image Processing*, (Atlanta, GA), pp. 1261–1264, 2006.

[67] M. Figueiredo and R. Nowak, "An em algorithm for wavelet-based image restoration," *IEEE Trans. Image Processing*, vol. 12, pp. 906–916, 2003.

[68] A. Kong, *Electromagnetic Wave Theory*. Cambridge, MA: EMW Publishing, 2000.

[69] C. Balanis, *Advanced Engineering Electromagnetics*. Hoboken, NJ: John Wiley & Sons, 1989.

[70] E. Jordan and K. Balman, *Electromagnetic Waves and Radiating Systems*. Englewood Cliffs, NJ: Prentice-Hall, 1968.

[71] W. Stutzman and G. Thiele, *Antenna Design Theory*. New York: John Wiley & Sons, 1981.

[72] J. Marble and A. Yagle, "Measuring landmine size and burial depth using ground penetrating radar," in *Proc. SPIE Int. Detection and Remediation Technologies for Mines and Minelike Targets IX*, (Orlando, FL), pp. 409–420, 2004.

[73] F. Ulaby, R. Moore, and A. Fung, *Microwave Remote Sensing (Vol.1)*. London: Addison-Wesley, 1981.

[74] H. Jakubowicz and S. Levin, "A simple exact method of 3-d migration," *Geophysical Prospecting*, vol. 31, pp. 34–56, 1983.

[75] Y. Yu, T. Yu, and L. Carin, "3d inverse scattering of a dielectric target embedded in a lossy half-space," *IEEE Transactions on Geoscience and Remote Sensing*, vol. 5, pp. 957–973, 2004.

[76] J. Marble and A. O. Hero, "Phase distortion correction for see-through-the-wall radar imaging," in *Proc. IEEE Int. Conf. on Image Processing*, (Atlanta, GA), pp. 2333–2336, 2006.

[77] H. Haddar, S. Kusiak, and J. Sylvester, "The convex back-scattering support," *Journal of Applied Math*, vol. 66, pp. 591–615, 2006.

[78] L. Potter and R. Moses, "Attributed scattering centers for sar atr," *IEEE Trans. Image Proc.*, vol. 6, pp. 79–91, 1997.

[79] P. Silverstein, O. Sands, and F. Garber, "Radar target classification and interpretation by means of structural descriptions of backscatter signals," *IEEE AES Systems Magazine*, vol. 6, pp. 3–7, 1991.

[80] R. Carriere and R. Moses, "High resolution radar target modeling using a modified prony estimator," *IEEE Trans. Antennas and Propagation*, vol. 40, pp. 13–18, 1992.

[81] J. Marble and J. Gorman, "Performance comparison of phenomenology-based features to generic features for false alarm reduction in uwb sar imagery," in *Proceedings of SPIE Algorithms for Synthetic Aperture Radar Imagery VI*, (Orlando, FL), pp. 235–242, 1999.

[82] K. Kastella, "Discrimination gain to optimize classification," *IEEE Transactions on Systems, Man and Cybernetics-Part A: Systems and Humans*, vol. 27, pp. 112–116, January 1997.

[83] C. Kreucher, K. Kastella, and A. O. Hero, "Multi-target sensor management using alpha-divergence measures," in *3rd Workshop on Information Processing for Sensor Networks*, (Palo Alto, CA), pp. 209–222, 2003.

[84] M. Yuan and Y. Lin, "Efficient empirical bayes variable selection and estimation in linear models," *Journal of the American Statistical Association*, vol. 100, pp. 1215–1225, 2005.

[85] H. Libby, *Introduction to Electromagnetic Nondestructive Test Methods*. Malabar, FL: Robert E. Krieger Publishing Company, 1971.

[86] J. McNeill, *Technical Note TN-7: Applications of Transient electromagnetic Techniques*. Mississuaga, ON: Geonics LTD, 1980.

[87] Y. Guo, *Technical Report ST2-93-074: Electromagnetic Detection of an Object Buried in a Dissipative Medium*. Laurel, MD: Johns Hopkins University / Applied Physics Laboratory, 1993.

[88] D. Hill and J. Wait, "The electromagnetic response of a buried sphere for buried dipole excitation," *Radio Science*, vol. 8, pp. 813–818, 1973.

[89] Y. Guo, *Technical Report ST2-94-020: Imaging Subsurface Objects by Nearfield Electromagnetic Holography*. Laurel, MD: Johns Hopkins University / Applied Physics Laboratory, 1994.

[90] J. Lenz, "A review of magnetic sensors," *Proceedings of the IEEE*, vol. 6, pp. 973–989, 1990.

[91] J. Campbell and A. Jacobs, "Detection of buried land mines by compton backscatter imaging," *Nuclear Science and Engineering*, vol. 119, pp. 417–424, 1992.

[92] E. Dugan, A. Jacobs, Z. Su, L. Houssay, and D. Ekdahl, "Status of the xmis x-ray backscatter radiography landmine detection system," in *Proceedings of the SPIE Detection and Remediation Technologies for Mines and Minelike Targets VIII*, (Orlando, FL), pp. 34–44, 2003.

[93] A. Faust, R. Rothschild, and W. Heindl, "Development of a coded aperture backscatter imager using the uc san diego hexis detector," in *Proceedings of the SPIE Detection and Remediation Technologies for Mines and Minelike Targets VIII*, (Orlando, FL), pp. 95–106, 2003.

[94] J. McFee and A. Faust, "Defence r&d canada research on nuclear methods of landmine detection," in *Proceedings of the SPIE Detection and Remediation Technologies for Mines and Minelike Targets VIII*, (Orlando, FL), pp. 1–12, 2003.

[95] W. Niemann, S. Olesinski, and T. Thiele, “Detection of buried landmines with x-ray backscatter technology,” *Non-destructive Testing*, vol. 7, 2002.

[96] H. Barrett and W. Swindell, *Radiological Imaging*. New York: Academic Press, 1981.